

e-ISSN: 3048-460X

CNS&E

Current Natural
Sciences &
Engineering

Peer reviewed, Open-access Journal



AGNI-V

**Inter-Continental
Ballistic Missile
(ICBM)**



**Multiple Independently
Targetable Re-entry
Vehicle (MIRV)**

Volume 1 Issue 2, March 2024

About CNS&E

Current Natural Science & Engineering (CNS&E) Journal publishes new, innovative and cutting-edge research in Natural sciences including physical, chemical, biological, agricultural and environmental sciences, metrology, and other related interdisciplinary fields. Scientific research results in the form of high-quality manuscripts, review articles, mini-reviews, reports, news and short communications are highly welcome.

CNS&E is an Open Access, bimonthly, multidisciplinary journal published by the Vigyanvardhan Blessed Foundation (VBF), a non-profit organization working to disseminate science for the betterment of society.

Scope: CNS&E journal has a broad multidimensional scope. It publishes research in the areas of:

- Hydrogen & Renewable Energy
- Environmental Sciences & Hydroelectric Cell
- Artificial Intelligence Convergence in S&T
- Net Carbon Zero & Earth Sustainability
- Condensed Matter & Nanomaterials
- Health Science & Technology
- Nuclear Science: Health & Society
- Measurement Science & Industrial Research
- Digital & Sustainable Agriculture
- Smart Engineering Materials & Sensors

Publication Policy: The journal maintains integrity and high ethical values. Submitted manuscripts are peer-reviewed and evaluated for novel scientific content irrespective of its origin. The information about a submitted manuscript will be confidential and will not be disclosed other than Chief Editor, editorial staff, corresponding author, reviewers, and the publisher. The journal ensures that any unpublished work must not be used in Editor's, and reviewer's own research without the explicit written consent of the author(s).

Publication Decisions: The Chief Editor of the journal is responsible for deciding the publication or rejection of the submitted manuscript. The Chief Editor may take suggestion with other editors or reviewers in making decision.

Publisher: VB Foundation

CNS&E Editorial Board

Chief Editor

Prof. (Dr.) R K Kotnala,

Former Chairman NABL, Raja Ramanna Fellow DAE &
Chief Scientist, CSIR-National Physical Laboratory

Senior Editors

Prof. A C Pandey

Director, Inter University Accelerator
Centre, New Delhi, India

Prof. K K Pant

Director IIT Roorkee, Uttarakhand, India

Prof. R K Sinha Vice Chancellor,

Gautam Buddha University, G Noida, India

Prof. Bhanooduth Lalljee,

President, Sustainable Agricultural
Organisation, External Professor at the
Mauritius Institute of Education (MIE) and
JSS Academy, Mauritius.

Editors

Dr. Indra Mani

Vice-Chancellor, Vasantrya Naik
Marathwada Krishi Vidyapeeth,
Maharashtra, India

Prof Ajay Dhar

Associate Director, Academy of Scientific
and Innovative Research, AcSIR,
Ghaziabad-UP, India

Dr A K Srivastava

Director, CSIR-Advanced Materials and
Processes Research Institute, CSIR-
AMPRI, Bhopal

Dr. S K Jha

Outstanding Scientist and Head, Radiation
Protection Section (Nuclear Fuels) Health
Physics Division & Professor, HBNI,
Bhabha Atomic Research Centre, Mumbai.

Dr. Nasimuddin

Principal Scientist, Antenna and Optical
Department, Institute for Infocomm
Research; Agency for Science, Technology,
and Research, Singapore.

Associate Editors

Prof. Kedar Singh

Professor & Dean of School of Physical
Sciences, Jawaharlal Nehru University,
New Delhi, India

Prof Rajesh Punia

Head of Department, Department of
Physics, MDU, Rohtak, India

Dr Jyoti Shah

DST-WoSA, CSIR-National Physical
Laboratory, India

Dr. Rakesh Kr Singh

Academic Head, Aryabhata Center for
Nano Science and Nano Technology,
Aryabhata Knowledge University, Patna,
India

CNS&E Volume 1, Issue 2, March 2024

Table of contents:

S. No.	Title and Author	Page No.
1.	Raman Spectroscopy Analysis for Precise Channel Temperature Estimation in AlGaIn/GaN HEMT Devices Marsha M. Parmar, Robert Laishram, Preeti Garg & D.S. Rawal	109-114
2.	Source apportionment and health risk assessment of PM10 bound carbonaceous and elemental species in the central Himalayas Sakshi Gupta, Preeti Tiwari, Priyanka Srivastava, Manish Naja, Nikki Choudhary, Narayanasamy Vijayan, Manoj Kumar, Sudhir Kumar Sharma	115-126
3.	Physico-chemical and microbiological changes in degradation of agri-residue under pit composting Livleen Shukla, Roaf A. Parray, K Annapurna, Satish D Lande, Indra Mani, Deeba Kamil	127-136
4.	Production of Green energy via Water Splitting mechanism by Mn- doped cobalt ferrites [Co_{1-x}Mn_xFe₂O₄] based hydroelectric cells Prachi Jain, S. Shankar, O. P. Thakur	137-145
5.	Induced Magnetization in Antiferromagnetic GdFeO₃ by Nonmagnetic Titanium Substitution for Magnetic Switching and Storage Application Jyoti shah and R K Kotnala	146-150
6.	Electronic Motion and Path Study in Presence of Varying Electric Field Using SciLab 6.1.1 for Coupled Differential Equations Ravindra Singh, Shiv Shankar Gaur	151-156
7.	Laser Induced Damage Study of Dye Doped Polystyrene Films deposited in Glass Substrate by Dip Coating Technique Amit Pratap Singh, Shiv Shankar Gaur	157-162
8.	Low-cost green Synthesis of Silica Engineering Nanomaterials from rice husk (Agriculture waste) and its physical and luminescent properties measurements Akansha Kumari, Rakesh Kr Singh, Abhay Kr Aman, Nishant Kr, Ajitendra Kr Singh	163-173

Raman Spectroscopy Analysis for Precise Channel Temperature Estimation in AlGa_N/Ga_N HEMT Devices

Marsha M. Parmar*, Robert Laishram, Preeti Garg & D.S. Rawal

Solid State Physical Laboratory, Lucknow Road, Delhi 110054, India.

Volume 1, Issue 2, March 2024

Received: 11 March, 2024; Accepted: 26 March, 2024

DOI: <https://doi.org/10.63015/10s-2421.1.2>

**Corresponding author email: sarikamarsha@gmail.com*

Abstract: In recent years, high-electron-mobility Ga_N HEMTs have demonstrated significant advancements in applications such as power converters and RF amplifiers. Nevertheless, their thermal reliability poses a notable challenge, placing constraints on their power-handling capacities. This study employs micro-Raman spectroscopy to evaluate the localized self-heating-induced channel temperature. The channel temperature, determined using the single phonon modes of Ga_N HEMT (E₂(H) & A₁(LO)), exhibits discrepancies and does not align with device temperature values calculated using the SiC phonon peak near the Ga_N channel. However, by employing both phonon modes of Ga_N to decouple the combined effects of joule heating and the thermoelastic effect, accurate channel temperature values are obtained, matching well with those obtained from the SiC phonon peak. The agreement between calculated temperatures from phonon modes and those obtained by heating the device from the back side enhances the credibility of the proposed method.

Keywords: Ga_N HEMT, micro-Raman Spectroscopy, channel temperature, self-heating

1. Introduction: Gallium Nitride (Ga_N) High Electron Mobility Transistors (HEMTs) have become pivotal components in high-frequency and high-power applications [1], [2], [3]. In Ga_N-based devices, the choice of substrate material, particularly between Ga_N-on-Si and Ga_N-on-SiC, introduces critical considerations for power density and thermal management [4]. The inherent limitations of Ga_N-on-Si, specifically associated with self-heating in the channel, impose constraints on output power density compared to Ga_N-on-SiC. This discrepancy is accentuated by the relatively lower thermal conductivity of single-crystalline Ga_N ($k_{\text{GaN}} \sim 130 \text{ Wm}^{-1}\text{K}^{-1}$), comparable to silicon ($k_{\text{Si}} \sim 148 \text{ Wm}^{-1}\text{K}^{-1}$), but significantly inferior to silicon carbide ($k_{\text{SiC}} \sim 350 \text{ Wm}^{-1}\text{K}^{-1}$). While Ga_N-on-SiC, with its elevated thermal conductivity, partially alleviates thermal concerns, it falls short of fully unleashing the potential of Ga_N HEMTs in terms of both direct current (DC) and radio frequency (RF) powers due to suboptimal heat dissipation. Recent advancements,

exemplified by Ga_N-on-diamond substrates boasting superior thermal conductivity ($k_{\text{diamond}} \sim 1800 \text{ Wm}^{-1}\text{K}^{-1}$), present a promising avenue for mitigating the thermal limitations of Ga_N HEMTs. Ga_N-on-diamond configurations have demonstrated record-breaking DC power densities of up to 56 Wmm⁻¹, surpassing traditional substrates [5]. The heightened power density directly translates into a more expansive safe operating area (SOA) for power transistors. This introduction lays the groundwork for our research, which focuses on the integration of diamond as a chip-level heat spreader for Ga_N HEMTs.

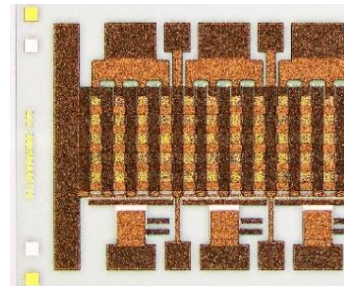
Before exploring various thermal management strategies, accurately determining the channel temperature is crucial. Raman spectroscopy, with a spatial resolution of 1-2 μm, has been extensively researched for determining localized self-heating-induced device temperature as an alternative to IR thermography, which has a spatial resolution of 5 μm [6]. Raman spectroscopy, a non-

destructive technique, enables the estimation of channel temperature with a resolution better than $2\mu\text{m}$. This method relies on the interaction of light with materials at the molecular level. Its widespread use in studying the properties of group III nitrides is attributed to their strong Raman activity. In the Raman scattering process, a photon of wavelength λ_0 from the excitation source, typically a narrow linewidth laser, undergoes inelastic scattering to a different wavelength λ by emitting (Stokes process) or absorbing (anti-Stokes process) an optical phonon in the sample. Each allowed optical phonon mode appears as a peak with a centroid ω and linewidth Γ , related to the phonon frequency and lifetime. The Raman peak position $\omega = \lambda_0^{-1} - \lambda^{-1}$, specified in units of cm^{-1} , is proportional to the phonon frequency, and the linewidth Γ reflects the phonon lifetime. Given that phonon frequencies, lifetimes, and populations vary with temperature, micro-Raman spectroscopy in GaN HEMTs employs Stokes peak positions, Stokes peak linewidths, and/or Stokes/anti-Stokes intensity ratios for temperature measurement [7]. It is noteworthy that although Raman Spectroscopy provides better resolution than IR, the former takes longer time to collect the data. The relationship between Raman peak shifts and temperature/stress is not uniquely defined and can vary depending on factors such as material composition, sample geometry, and measurement conditions.

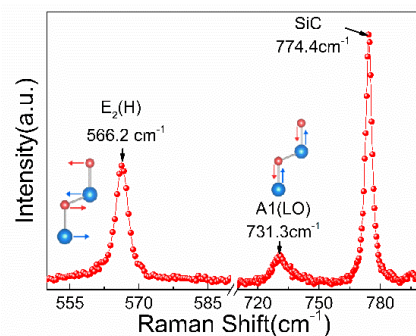
In the subsequent section, we delve into the details of in-situ Raman measurements conducted on in-house fabricated GaN HEMTs to determine channel temperature during external bias application, addressing self-heating effects. For this purpose, we devised an integrated electrical setup capable of delivering DC bias to the GaN HEMTs while concurrently conducting temperature measurements. In our study, we utilized two key GaN phonon modes: E₂(H) and A₁(LO). These phonon modes exhibit combined responses to temperature variations and stress-induced shifts in peak positions. To separate the temperature and stress contributions, we utilized mathematical models that incorporate

both temperature and stress terms into the analysis of Raman peak shifts. By simultaneously analyzing the changes in peak positions and linewidths of both E₂(H) and A₁(LO) phonon modes, we were able to establish relationships between temperature, stress, and Raman peak shifts. This approach allowed us to quantitatively determine the temperature and stress components contributing to the observed Raman peak shifts, thereby enabling a more accurate estimation of the channel temperature in GaN HEMT devices.

2. Experimental Details: For the in-situ measurement of the channel temperature during the application of a DC bias, we designed and fabricated a printed circuit board (PCB) using the toner transfer method. To enhance the PCB's suitability for wire bonding, we applied a $3\mu\text{m}$ thick gold electroplating process to cover the entire board. Subsequently, banana jack connectors were soldered to the PCB to ensure a robust connection. Special attention was given to ensuring that the PCB precisely matched the dimensions of the substrate holder hole in the Raman setup, minimizing any potential movement during in-situ measurements. The devices were bonded to the PCB using a TPT



wire bonder. GaN HEMTs, grown through



metal-organic chemical vapor deposition on a

Figure 1(a) Optical micrograph of final device after fabrication. $L_g = 0.4\mu\text{m}$, $L_{sd} = 4\mu\text{m}$, $L_{gg} = 60\mu\text{m}$, Unit gate width = $300\text{--}400\mu\text{m}$. (b) Raman Spectroscopy of GaN HEMT under ambient condition.

SiC substrate, were investigated. These devices featured a 25nm AlGaN layer on top of HEMT with increasing V_{ds} due to self-heating. The phonon peak positions of GaN, namely $E_2(\text{H})$ and $A_1(\text{LO})$, as well as that of SiC, shift $2\mu\text{m}$ doped GaN buffer layer. Standard Ti/Al/Ni/Au Ohmic contacts and Ni/Au Schottky gates were employed in the design, with a source-drain separation of $4\mu\text{m}$, a gate length of $0.4\mu\text{m}$, and a gate-to-gate distance of $60\mu\text{m}$ in a multifinger configuration, as illustrated in the optical micrograph in Figure 1a. The operation involved applying a DC source-drain bias ranging from 0 to 6 V and a -2.7 V gate voltage. Micro-Raman measurements were conducted using a Horiba spectrometer with a 532 nm frequency-doubled Nd:YAG laser as the excitation source. The sub-bandgap laser illumination was carefully chosen to ensure minimal laser absorption, avoiding interference with device operation during measurements. The experimental setup adopted ZX, $-Z$ Raman backscattering configuration with unpolarized detection, allowing simultaneous measurement of the $A_1(\text{LO})$ (out-of-plane) and $E_2(\text{H})$ (in-plane) phonon modes of GaN. Figure 1b depicts a Raman spectrum obtained from an in-house fabricated GaN HEMT under unbiased conditions, revealing the presence of the two most common modes of GaN, namely $E_2(\text{H})$ (in-plane, 568.5 cm^{-1}) and $A_1(\text{LO})$ (out-of-plane, 736.5 cm^{-1}). The reported wavenumbers correspond to the unstrained GaN layer. However, in the context of HEMT devices where GaN is grown on different materials, such as SiC, mismatches in lattice constants and thermal expansion coefficients occur. Consequently, even under unbiased conditions, shifts from the nominal peak frequencies were observed, as illustrated in Figure 1b. A red shift in the mentioned phonon peak positions signifies an overall tensile strain in the device, while a blue shift indicates compressive strain. We used 532 nm laser light for recording Raman spectra, allowing only

25% of the laser power to fall on the sample to avoid heating. A 50X LWD objective was used for focusing, and the spot size was approximately $2.5\mu\text{m}$. The Raman spectra were recorded at a spot between the drain and source, as shown in the inset of Figure 2a. The spectra were recorded at a gate bias of -2.7 V while the source-to-drain voltage was swept from 0V to 6V. To prevent overheating, since no active cooling was applied, the current compliance was kept at 500mA. The Raman spectroscopy data provides an examination of average temperatures across the $2\mu\text{m}$ thickness of the GaN stack layer in our devices. The depth of focus (DOF) extends beyond the thickness of the GaN layer, enabling the collection of signals from SiC phonon modes in close proximity to the GaN layer. Figure 2a

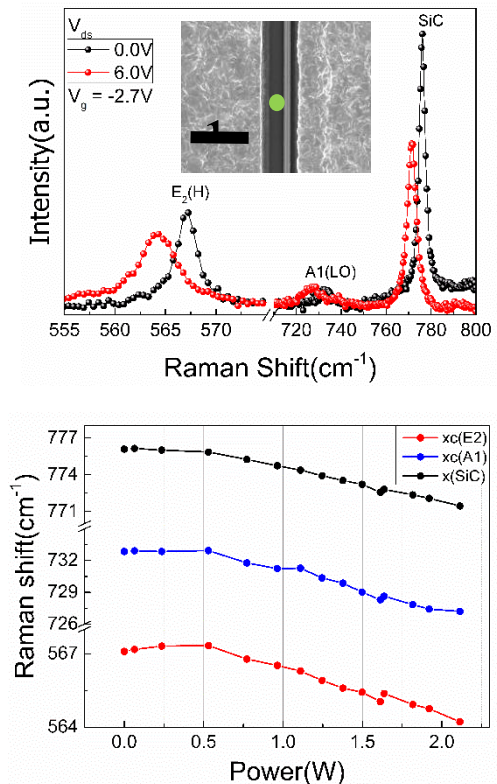


Figure 2(a) Raman Spectra of GaN HEMT. The black curve shows the Raman peaks at 0 V bias condition while the pink one shows the Raman spectra at $V_{ds} = 6.0\text{ V}$. The curves show a clear shift in Raman peaks due to self-heating under biased condition. (b) The observed shift in Raman peaks of optical phonon modes for $E_2(\text{H})$, $A_1(\text{LO})$ and SiC under biased condition due to self-heating.

clearly shows a shift in both in-plane ($E_2(\text{H})$) and out-of-plane ($A_1(\text{LO})$) modes of GaN

towards the lower wavenumber side. Figure 2b illustrates the Raman shift in GaN and SiC spectra as a function of applied power to the device.

3. Results and Discussion: The generation of the Raman scattering spectrum is intricately linked to the lattice vibrations of the sample. When subjected to tensile or compressive residual stress, the atomic bond lengths adjust, altering the lattice vibration energy. The frequency shift in the Raman spectrum is sensitive to the sample's temperature and stress. $\omega(T) = \omega_0 + \frac{A}{e^{Bhc/kT}-1}$ (1)

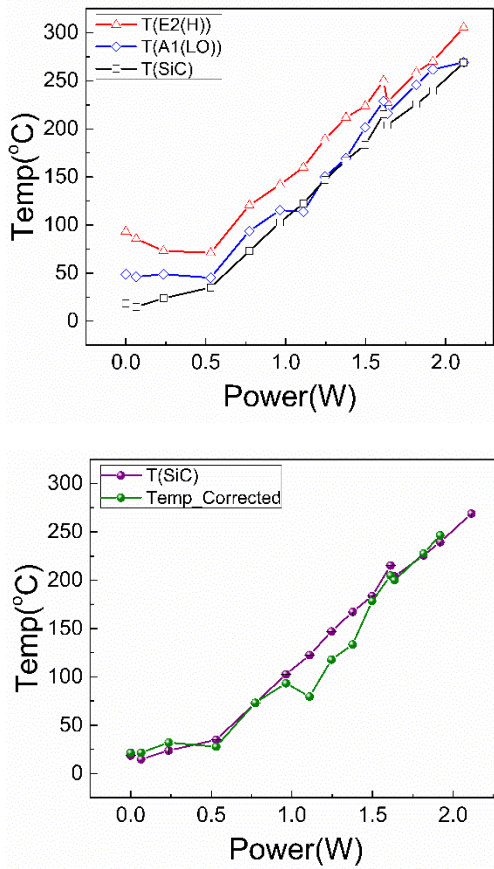


Figure 3(a) Calculated channel temperature versus biased power of GaN HEMT assuming the shift in phonon frequencies is only due to heating (eq 1). **(b)** Calculated in channel temperature taking into account the shift in the phonon frequencies as a combined effect of heating and thermal stress (eq 2).

where, $\omega(T)$ is the Raman peak position at temperature T in kelvin, ω_0 is the Raman peak position at absolute zero, A and B are empirical constants determined by calibration [7]. Using above equation one can calculate the

temperature of the device from just one phonon peak. The estimated temperature from all the three peaks namely E2(H), A1(LO) and SiC are shown in Figure a. It must be noted that the temperature calculated from each of the peak using equation has a difference of $\sim 50^\circ\text{C}$ moreover, the base temperature as calculated by E2(H) peak suggests that the device temperature at 0 bias is $\sim 100^\circ\text{C}$ which is 75°C more than the room temperature. This means the shift in the peaks due to self-heating is not entirely the effect of increase in local temperature but has contribution from another factor. It turns out that stress also affects phonon frequencies and can therefore also be determined using Raman spectroscopy. However, the key challenge is that phonon frequency changes induced by thermal stress are superimposed on the direct temperature induced change, and are typically much smaller. By combining information from both phonon modes, namely E2(H) and A1(LO) we can simultaneously determine temperature and thermal stress from the Raman measurement. Eq (1) can be modified to include thermal stress as [9],

$$\omega(T) = \omega_0 + \frac{A}{e^{Bhc/kT}-1} - 2a'\epsilon_{xx} \quad (2)$$

where, a' is empirical constant and ϵ_{xx} is biaxial strain. If we use equation 2 and calculate the temperature excluding the contribution of stress, it matches well with SiC temperature as shown in Figure (b). The SiC does not have a lattice mismatch during growth so it does not have the effect of thermal stress, hence for SiC, one phonon peak is enough for temperature estimation. Both the E2(H) and A1(LO) phonon modes exhibit responses to temperature variations and thermoelastic effects in the form of shifts in above phonon peak positions. For decoupling the effect of joule heating with that of thermoelastic effects in phonon peaks we used equation 2. Now to calculate the values of these two variables, we formed two equations using the shift in the peak position of E2(H) and A1(LO) phonon modes which change with increase in bias voltage. These two equations when simultaneously solved together, decouple the

combined effect of joule heating and thermoelastic effect. By analyzing the changes in peak positions of both phonon modes simultaneously, we were able to differentiate between the contributions of temperature and stress to the observed shifts in Raman peaks.

Moreover, the unbiased temperature values also drop to also drops to 22°C which was the ambient temperature. The discrepancies between temperatures obtained using single phonon modes of GaN and the SiC peak primarily arise due to the difference in lattice mismatch during the growth of GaN on SiC. The lattice mismatch between SiC and GaN is 3.5% which gives rise to thermoelastic stress under dc biased condition. So the shift in phonon modes of GaN (namely E2(H) & A1(LO)) has combined effect of joule heating and thermoelastic effect. While for SiC, there is no lattice mismatch condition. Hence the shift in the peak is entirely due to joule heating. Also, since the DOF of the Raman microscope for 532 nm laser is 2 μ m, the temperature calculated from SiC peak is almost equal to the channel temperature. The use of equation 2 decouples the combined effect of joule heating and thermoelastic effect for GaN using two phonon modes. Whereas for SiC since the later effect is not present equation 1 is able to provide the correct result. In our study, Raman spectroscopy plays a crucial role in determining the peak operating temperature of GaN HEMT devices, which we identified to be 200°C. This temperature, corresponding to a specific bias condition (e.g., $V_{gs} = -2.7V$ and $V_{ds} = 6V$), represents a critical parameter for assessing device performance and thermal reliability. The determination of this peak operating temperature is facilitated by analyzing the shifts in Raman peaks, particularly those associated with the E2(H) and A1(LO) phonon modes of GaN. These shifts in peak positions, observed under biased conditions, reflect the combined effects of joule heating and thermoelasticity within the device structure. By meticulously analyzing the Raman data collected under varying bias voltages and conditions, we were able to identify the temperature at which the device

operates optimally, corresponding to the peak operating temperature of 200°C. This temperature not only provides crucial insights into the thermal behavior of GaN HEMTs but also serves as a reference point for evaluating device performance and reliability under different operating conditions. Furthermore, the agreement between the peak operating temperature determined from Raman spectroscopy and the observed device temperature during backside heating experiments reinforces the credibility and accuracy of our method. This alignment underscores the effectiveness of Raman spectroscopy in providing precise temperature estimations, thereby enhancing our understanding of thermal management strategies in GaN HEMT devices.

Again, to back check the calculated channel temperature, we heated the device from back side using a thermal chuck and noted the shift in peak position and compared it with the temperature values obtained during self-heating. The results are plotted in Figure . Hence, the true channel temperature can be characterized by assuming the shift in phonon frequencies as a combined effect of heating

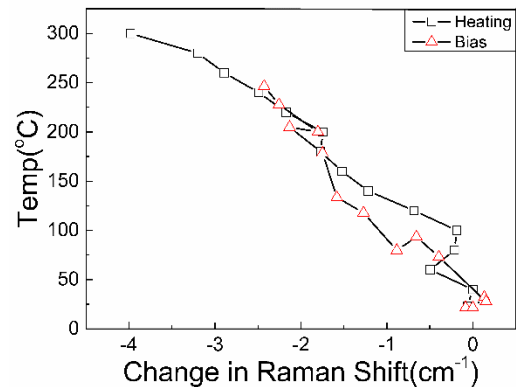


Figure 4 Comparison of the channel temperatures while heating the device from backside with that of self-heating.

and thermal stress which matches well with the channel temperature of the device while heating from back-side.

4. Conclusions: Raman spectroscopy offers insights into the vibrational characteristics of GaN and SiC, revealing sensitivity to factors

such as crystalline quality, temperature, stress, and free carrier density. By employing two phonon modes to separate temperature and stress components, it allows for a more precise determination of channel temperature. The identified peak operating temperature is 200°C at $V_{gs} = -2.7V$ and $V_{ds} = 6V$, aligning closely with the device temperature observed during backside heating. This research sheds light on the critical issue of thermal reliability in GaN HEMTs, offering detailed insights into temperature effects through micro-Raman spectroscopy. The agreement between calculated temperatures and SiC characterization enhances the credibility of the proposed method.

Acknowledgement: We gratefully acknowledge Director SSPL and GaN team at SSPL & GAETEC for fabrication and SSPL characterization division for all the support.

Conflict of Interest: Authors declare No conflicts of interest.

References:

- [1]X. Yang *et al.*, “Dynamic RON Free 1.2-kV Vertical GaN JFET,” *IEEE Transactions on Electron Devices*, vol. 71, no. 1, pp. 720–726.
- [2]Y. Liao, H. Li, K. Qu, and X. Liu, “A Novel Inverse-L Buried GaN Current-Aperture Vertical Electron Transistors,” in *2023 Cross Strait Radio Science and Wireless Technology Conference (CSRSWTC)*.
- [3]D. Wang, D. H. Mudiyansele, and H. Fu, “Design of kV-Class and Low RON E-Mode β -Ga₂O₃ Current Aperture Vertical Transistors With Delta-Doped β -(Al_xGa_{1-x})₂O₃/Ga₂O₃ Heterostructure,” *IEEE Transactions on Electron Devices*, vol. 70, no. 11, pp. 5795–5802.
- [4]J. Kuzmik *et al.*, “Self-Heating in GaN Transistors Designed for High-Power Operation,” *IEEE Transactions on Electron Devices*, vol. 10, no. 61, pp. 3429–3434, 2014,
- [5]M. J. Tadjer *et al.*, “GaN-On-Diamond HEMT Technology With TAVG = 176°C at PDC,max = 56 W/mm Measured by Transient Thermoreflectance Imaging,” *IEEE Electron Device Letters*, vol. 40, no. 6, pp. 881–884,.

[6]“A Review of Raman Thermography for Electronic and Opto-Electronic Device Measurement With Submicron Spatial and Nanosecond Temporal Resolution | IEEE Journals & Magazine | IEEE Xplore.”

[7]A. Sarua *et al.*, “Integrated micro-Raman/infrared thermography probe for monitoring of self-heating in AlGa_N/Ga_N transistor structures,” *IEEE Transactions on Electron Devices*, vol. 53, no. 10, pp. 2438–2447.

[8]M. S. Liu, L. A. Bursill, S. Praver, K. W. Nugent, Y. Z. Tong, and G. Y. Zhang, “Temperature dependence of Raman scattering in single crystal GaN films,” *Applied Physics Letters*, vol. 74, no. 21, pp. 3125–3127.

[9]T. Batten, J. W. Pomeroy, M. J. Uren, T. Martin, and M. Kuball, “Simultaneous measurement of temperature and thermal stress in AlGa_N/Ga_N high electron mobility transistors using Raman scattering spectroscopy,” *Journal of Applied Physics*, vol. 106, no. 9, p. 094509.

Source apportionment and health risk assessment of PM₁₀ bound carbonaceous and elemental species in the central Himalayas

Sakshi Gupta^{1,2}, Preeti Tiwari^{1,2}, Priyanka Srivastava³, Manish Naja³, Nikki Choudhary^{1,2}, Narayanasamy Vijayan^{1,2}, Manoj Kumar^{1,2}, Sudhir Kumar Sharma^{1,2*}

¹ CSIR-National Physical Laboratory, Dr. K. S. Krishnan Road, New Delhi 110012, India.

² Academy of Scientific and Innovative Research (AcSIR), Ghaziabad 201002, India

³ Atmospheric Division, Aryabhata Research Institute of Observational Sciences (ARIES), Nainital 263002, Uttarakhand, India.

Volume 1, Issue 2, March 2024

Received: 6 February, 2024; Accepted: 14 March, 2024

DOI: <https://doi.org/10.63015/2e-2418.1.2>

*Correspondence author email: sudhircsir@gmail.com

Abstract: In this extensive investigation, the sources and health risk assessment of carbonaceous aerosols, as well as the elemental compositions (Ca, Al, Fe, S, K, Mg, Pd, B, Mo, Zn, Ag, Nb, Ga, Cl, Ti, Zr, Na, Cr, Cu, Mn, Cs, P, Y, Sb, Ni, Sn, F, Sr, Br, Pm, U, Pb, Th, Br, Rb, and V) of PM₁₀, were conducted throughout January-December 2021 in Nainital, a central Himalayan region of India. The average annual mass concentration of PM₁₀ was determined to be 64±6 µg m⁻³. Carbonaceous aerosols (CAs), comprising OC, EC, WSOC, and SOC, exhibited annual averages of 9.3±0.8 µg m⁻³, 4.9±0.5 µg m⁻³, 1.5±0.2 µg m⁻³, 2.7±0.2 µg m⁻³, and 2.97±0.45 µg m⁻³, respectively. The elemental composition featured major contributors such as Ca, Al, Fe, S, and K, alongside trace levels of various elements (Mg, Pd, B, Mo, Zn, Ag, Nb, Ga, Cl, Ti, Zr, Na, and Cr). Positive Matrix Factorization (PMF) identified six primary contributors to PM₁₀, each with varying percentage contributions: crustal/soil/road dust, soil re-suspension, combustion, vehicular emissions, industrial emissions, and biomass burning. The health risk assessment revealed elevated Hazard Quotient (HQ) values for Cr and Mn in children, indicating a non-carcinogenic health risk. Adults exposed to high Cr levels may face potential carcinogenic risks, while elements like Al, Pb, Cu, Zn, and Ni pose no health hazards, aligning with USEPA guidelines.

Keywords: PM₁₀, Carbonaceous aerosols, Elemental composition, Source apportionment, Health risk assessment

1. Introduction: Atmospheric aerosols play a crucial role in shaping regional and global climates, affecting air quality, visibility, the Earth's radiation balance, the hydrological cycle, human well-being, crop production, and ecosystems [1]. Carbonaceous aerosols, composed of organic carbon (OC) and elemental carbon (EC) or black carbon (BC), have significant impacts on human health, radiative forcing, and climate change [2, 3]. In urban areas, carbonaceous aerosols contribute to 20–70% of the total aerosol mass, influencing the solar radiation budget [4,5]. Emissions of carbonaceous aerosols from sources like biomass burning, vehicles, and coal-based industries produce hazardous gases such as carbon monoxide (CO), volatile

organic compounds (VOCs), and polycyclic aromatic hydrocarbons (PAHs) [6-11], impacting respiratory and lung health [12]. Carbonaceous aerosols can be emitted directly (primary organic aerosols, POA) or formed indirectly in the atmosphere from VOCs through gas-phase oxidation [11]. The intricate interplay between pollutants, including carbonaceous species and trace elements, has far-reaching implications for environmental quality and public health [3]. The Himalayan ecosystem, including Nainital, faces significant challenges due to various pollutants [13]. Nainital's unique geographical and meteorological characteristics make it an ideal setting for such investigations [14-16]. Understanding the composition and sources of

PM₁₀ in this region is crucial for effective air quality management and protecting the local population's well-being [17].

This study utilizes advanced analytical techniques to explore the elemental composition of PM₁₀, uncovering major and trace elements with diverse sources, both natural and anthropogenic [3, 14-16, 18]. Our goal is to identify and characterize the sources of PM₁₀ in Nainital, unraveling complex atmospheric processes contributing to pollution levels. Additionally, assessing carbonaceous species within PM₁₀ will provide insights into the role of combustion-related emissions, biomass burning, and vehicular activities in shaping the region's air quality [15, 16]. Air masses from the anthropogenically influenced Indo-Gangetic Plain (IGP) region, carrying elevated levels of crop residue

burning by-products and industrial emissions, impact the area throughout the year, extending to oceanic regions [15, 19]. Beyond characterizing pollution sources, the study evaluates potential health impacts associated with PM₁₀ exposure. Understanding health implications is crucial for developing targeted mitigation measures and promoting sustainable development practices in the region. The findings aim to contribute to scientific understanding of air quality dynamics in the Himalayan region and inform policy interventions prioritizing the well-being of local communities [17]. This comprehensive assessment bridges the gap in our knowledge regarding PM₁₀ in the Himalayan region, offering a nuanced understanding of its elemental composition, sources, and health impacts, with Nainital serving as a representative case study.

2. Material & Methods:

2.1. Sampling Site: PM₁₀ samples were collected at the Aryabhata Research Institute of Observational Science (ARIES) in the Manora Hills of Nainital, India (29.35°N, 79.45°E, 1958 m above mean sea level) from January to December 2021, excluding monsoon months (July, August, September) due to precipitation. A total of 40 PM₁₀ samples were collected over 24 h, twice a week using pre-baked (at 550 °C) Pallflex quartz microfiber filters with a Particle Sampler (Model APM460, manufactured by M/s. Envirotech, India). The samples were preserved in a deep freezer at -20°C until chemical analysis. The sampler's average flow rate stood at 1.2 m³ min⁻¹, with a flow accuracy of within ±2% of its full scale. Pre- and post-sampling, filters underwent desiccation, and their initial and final weights were determined using a microbalance with a precision of ±10 µg. PM₁₀ concentration was assessed via gravimetric means. For detailed information on the sampling process, instrumentation used, and methodology, readers can refer to previous publications [3, 14, 15].

2.2. Chemical Analysis: To investigate carbonaceous aerosols, the study focused on estimating the OC (organic carbon), EC (elemental carbon), and WSOC (water-soluble organic carbon) fractions within the PM₁₀ samples. The OC/EC carbon analyzer (DRI 2001A, Atmoslytic Inc., Calabasas, CA, USA) was employed for quantifying OC and EC, utilizing the Interagency Monitoring of Protected Visual Environments (IMPROVE-A) procedure [20]. An area of approximately 0.536 cm² on the filter was carefully excised using the appropriate punch and subsequently subjected to duplicate analysis, providing outputs for OC (OC1, OC2, OC3, OC4) and OP (optical pyrolysis), as well as EC (EC1, EC2, and EC3) [21]. Quartz filters, commonly employed for PM collection and carbon content estimation via thermal-optical analysis, pose challenges such as potential gaseous organic absorption and OC volatilization. Addressing these, the relative impact of such artifacts was assessed using QBQ methods (sample is set up with a secondary quartz filter positioned behind either the primary quartz filter or a Teflon filter, aligned in parallel), with blank filter OC/EC values subtracted from sample results [22]. To

determine WSOC in PM₁₀ samples, a TOC analyser (Model: Shimadzu TOC-L CPH/CPN, Japan) was utilized, with a punch size of 30 mm diameter (7.065 cm²) from PM₁₀ for the analysis [21, 25]. The estimation of primary organic carbon (POC) and secondary organic carbon (SOC) was carried out using the EC tracer method, a common approach [15, 26]. Both OC and EC are products of fuel combustion, with EC serving as the primary tracer for POC. The ratio of OC to EC in fresh aerosols emitted during combustion, denoted as (OC/EC)_{min}, was used, and specific formulas were applied to calculate POC and SOC (Eqn. 1, and 2):

$$POC = [EC] \times (OC/EC)_{min} \quad (1)$$

$$SOC = OC - POC \quad (2)$$

To conduct elemental analysis encompassing a total of 36 elements (including Ca, Al, Fe, S, K, Mg, Pd, B, Mo, Zn, Ag, Nb, Ga, Cl, Ti, Zr, Na, Cr, Cu, Mn, Cs, P, Y, Sb, Ni, Sn, F, Sr, Br, Pm, U, Pb, Th, Br, Rb, and V) in PM₁₀ samples, a Wavelength Dispersive X-ray Fluorescence (WD-XRF) Spectrometer (Rigaku ZSX Primus) was utilized. The spectrometer setup comprised a scintillation counter (SC) for detecting heavy elements and a flow-proportional counter (F-PC) for detecting light elements, alongside a sealed X-ray tube for excitation, an end window, and a Rh-target. Measurements were conducted under vacuum conditions, at a temperature of 36°C, and with a tube rating of 2.4 kW. Various detection methods were employed for different elements: F-PC for Mg, Al, P, S, Cl, K, and Ca; RX25 analyzer crystal for Mg; PET analyzer crystal for Al; Ge analyzer crystal for P, Cl, and S; LiF (200) analyzer crystal for Ca and K; and SC detector along with a LiF (200) analyzer crystal for Ti, Cr, Mn, Fe, and Zn. Blank filters were also subjected to analysis to rectify intensities, ensuring precision with a repeatability error falling within the 5–10% range. Comprehensive details regarding the analytical procedures can be found in Sharma et al [3].

2.3. Source Apportionment and Trajectory Analysis: In this study, the Positive Matrix Factorization (PMF) technique was employed on PM₁₀ chemical constituents (OC, EC, WSOC, Ca, Al, Fe, S, K, Mg, B, Mo, Zn, Ga, Cl, Ti, Zr, Na, Cr, Cu, Mn, Ni, and P) to identify the sources influencing PM₁₀ concentration, using the US-EPA PMF 5.0. The PMF model involves decomposing a speciated data matrix (X) into factor contribution (C) and profile (P) matrices, along with a residual matrix (e) (Eqn. 3).

$$X = C \times P + e \quad (3)$$

The standard equation-based uncertainty (U) is derived through Eqn. 4, incorporating error fraction (ef), concentration (C), and the method detection limit (MDL) of the species [24].

$$U = \sqrt{(ef \times C)^2 + (0.5 \times MDL)^2} \quad (4)$$

$$U = \frac{5}{6} \times MDL, \quad C < MDL$$

Evaluation of model fit is based on Q-robust, excluding values with scaled residuals exceeding 4, compared to Q-true. Species with significant residuals indicate poor fitting, and error estimation employs DISP, BS, and BS-DISP methods [16, 28-30].

Air mass backward trajectory analysis was conducted using ARL datasets and the HYSPLIT model, tracing the pathways of PM₁₀ from the receptor site at 500 m above ground level (AGL). The TrajStat software was employed to generate and analyses 120 h trajectories [15, 25].

2.4. Health Risk Assessment (HRA): The calculation of the HRA followed criteria recommended by the United States Environmental Protection Agency (USEPA). Utilizing data from the Integrated Risk Information System (IRIS) database, the carcinogenic and non-carcinogenic risks associated with inhalation exposure to PM₁₀ elements (Al, Cr, Ni, Pb, Mn, Cu, and Zn) were evaluated. Among all the elements identified only heavy elements assessment was

conducted as per USEPA guidelines. Health risks were quantified through exposure concentration (EC) in terms of lifetime average daily dose, Hazard Quotient (HQ), and Carcinogenic Risk (CR) equations 5-7. The Hazard Quotient (HQ) exceeding 1 indicates potential adverse effects on human health, while CR assesses the additional probability of developing cancer throughout a person's lifetime. Reference values were adopted from USEPA, with acceptable cancer risk levels defined within a recommended range [31-33].

$$EC = \frac{C \times IR \times CF \times EF \times ED}{BW \times AT_n} \quad (5)$$

In the context of the calculation, C represents the concentration of the species ($\mu\text{g m}^{-3}$). Additionally, IR denotes the air inhalation rate, with values set at $10 \text{ m}^3 \text{ day}^{-1}$ for children and $20 \text{ m}^3 \text{ day}^{-1}$ for adults. The correction factor unit (CF) is defined as 0.001, EF stands for relative exposure frequency measured in days per year, ED represents exposure duration set at 24 years, BW corresponds to body weight (15 Kg for children and 70 Kg for adults), and AT_n signifies the average time (calculated as $70 \text{ years} \times 365 \text{ days} \times 24 \text{ h day}^{-1}$).

$$HQ = \frac{EC}{RFD} \quad (6)$$

The reference exposure dose (RFD) for the human population, expressed in mg m^{-3} , was adopted from USEPA 2015.

$$CR = \frac{C \times ET \times EF \times ED \times IUR}{AT} \quad (7)$$

In this context, ET represents exposure time (12 h/day), and IUR stands for the inhalation unit risk ($(\mu\text{g m}^{-3})^{-1}$) derived from elements in the USEPA IRIS (1995) database.

3. Results & Discussions:

3.1. Concentrations of PM_{10} Constituents: The annual average PM_{10} mass concentration ($\pm\text{SE}$) was estimated as $64 \pm 6 \mu\text{g m}^{-3}$ in Nainital, closely resembling the National Ambient Air Quality Standards (NAAQS) of $60 \mu\text{g m}^{-3}$ annually but surpassing the World Health Organization (WHO) limits by fourfold ($15 \mu\text{g m}^{-3}$) (Table 1). Elevated PM_{10} levels have been associated

with adverse health effects, including impaired lung function in children, respiratory issues, asthma exacerbations, and potential risks for adults, such as heart diseases, diabetes, and neurological problems [32, 34]. Previous studies in Nainital indicated an average PM_{10} concentration of $65 \pm 41 \mu\text{g m}^{-3}$ and $67 \pm 26 \mu\text{g m}^{-3}$ respectively that is closely correlated to our study [15, 23]. Hooda et al [24], reported the annual long term PM_{10} concentration at Mukteshwar, situated North-East direction to Nainital ($\sim 50 \text{ km}$) was $40 \pm 30 \mu\text{g m}^{-3}$. Fig. 1 represents the temporal variations of carbonaceous aerosols including OC, EC, WSOC, and SOC.

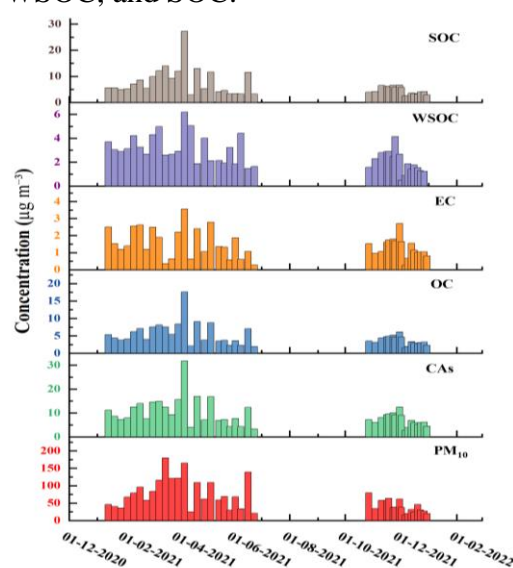


Figure 1. Time series of concentrations ($\mu\text{g m}^{-3}$) of PM_{10} , and carbonaceous aerosols at Nainital

Also, Table 1 shows the annual average concentrations for the same.

Table 1: Annual average concentrations ($\pm\text{SE}$) (in $\mu\text{g m}^{-3}$) of PM_{10} and their chemical constituents at Nainital.

Species	Average ($\mu\text{g m}^{-3}$)	Range ($\mu\text{g m}^{-3}$)
PM_{10}	64 ± 6	16-180
OC	4.90 ± 0.45	1.5-17.6
EC	1.48 ± 0.12	0.3-3.6
WSOC	2.72 ± 0.19	0.5-6.2
CAs	9.32 ± 0.82	2.7-27.4
SOC	2.97 ± 0.45	0.38-3.46
B	0.252 ± 0.024	0.04-0.62
Na	0.106 ± 0.031	0.003-0.944

Mg	0.377±0.081	0.015-2.648
Al	1.498±0.272	0.07-7.99
P	0.042±0.007	0.002-0.170
S	1.303±0.142	0.06-3.91
Cl	0.127±0.033	0.005-1.216
K	1.175±0.152	0.06-4.02
Ca	1.789±0.351	0.089-11.013
Ti	0.110±0.018	0.02-0.50
Cr	0.104±0.010	0.089-0.205
Mn	0.067±0.011	0.03-0.26
Fe	1.479±0.207	0.218-6.020
Ni	0.023±0.003	0.026-0.073
Cu	0.088±0.019	0.029-0.370
Zn	0.231±0.034	0.013-0.835
Ga	0.130±0.032	0.029-0.625
Zr	0.107±0.033	0.013-1.260
Mo	0.238±0.174	0.033-7.174
Br	0.010±0.009	0.03-0.35
Nb	0.165±0.111	0.025-4.031
Ag	0.166±0.076	0.69-2.22
Pb	0.005±0.003	0.089-0.107
Sr	0.013±0.004	0.031-0.106
Y	0.030±0.021	0.04-0.85
F	0.013±0.007	0.137-0.228
Pd	0.254±0.091	0.59-2.34
U	0.006±0.004	0.077-0.106
Sn	0.020±0.018	0.09-0.73
Cs	0.060±0.060	0.068-0.076

The annual average concentrations (\pm SE) of OC, EC, WSOC, and SOC were determined as $4.90\pm 0.45 \mu\text{g m}^{-3}$ (range: 1.5-17.6), $1.48\pm 0.12 \mu\text{g m}^{-3}$ (range: 0.3-3.6), $2.72\pm 0.19 \mu\text{g m}^{-3}$ (range: 0.5-6.2), and $2.97\pm 0.45 \mu\text{g m}^{-3}$ (range: 0.38-3.46), respectively. Total carbon (TC=OC+EC) concentration contributed ~10% to PM₁₀ (with OC at 7.7% and EC at 2.3%), while SOC contributed around 4.6% to PM₁₀. The fraction of carbonaceous aerosols (CAs) in PM₁₀, calculated as the sum of organic matter (OM=1.6×OC) and EC, accounted for ~14.5% of the PM₁₀ load [35]. Elevated levels of OC and EC indicated a notable influence from agricultural waste burning, particularly during rice and wheat harvesting in the north-western region of the

Indo-Gangetic Plain, along with the trans-border movement of pollutants to the receptor sites [21, 36].

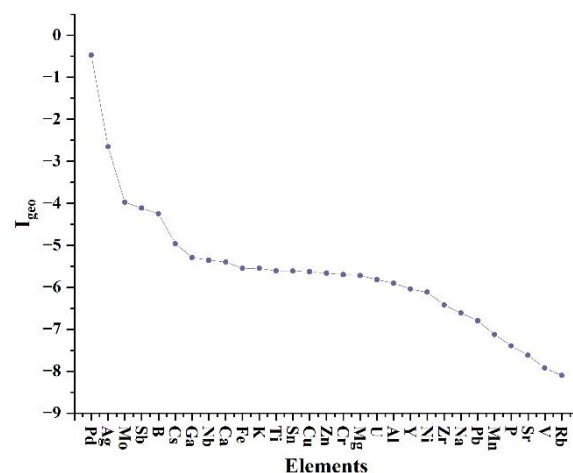


Figure 2: Geo-accumulation index (I_{geo}) of the elements of PM₁₀ over Nainital

The total elemental composition contributed ~16% to the total PM₁₀ mass concentration at the study site. Table 1 illustrates the annual average elemental concentrations, with Ca ($1.789 \pm 0.351 \mu\text{g m}^{-3}$), Al ($1.498 \pm 0.272 \mu\text{g m}^{-3}$), Fe ($1.479 \pm 0.207 \mu\text{g m}^{-3}$), S ($1.303 \pm 0.142 \mu\text{g m}^{-3}$), and K ($1.175 \pm 0.152 \mu\text{g m}^{-3}$) identified as major contributors to PM₁₀ concentrations. Elements such as Mg ($0.377 \pm 0.081 \mu\text{g m}^{-3}$), Pd ($0.254 \pm 0.091 \mu\text{g m}^{-3}$), B ($0.252 \pm 0.024 \mu\text{g m}^{-3}$), Mo ($0.238 \pm 0.174 \mu\text{g m}^{-3}$), Zn ($0.231 \pm 0.034 \mu\text{g m}^{-3}$), Ag ($0.166 \pm 0.076 \mu\text{g m}^{-3}$), Nb ($0.165 \pm 0.111 \mu\text{g m}^{-3}$), Ga ($0.130 \pm 0.032 \mu\text{g m}^{-3}$), Cl ($0.127 \pm 0.033 \mu\text{g m}^{-3}$), Ti ($0.110 \pm 0.018 \mu\text{g m}^{-3}$), Zr ($0.107 \pm 0.033 \mu\text{g m}^{-3}$), Na ($0.106 \pm 0.031 \mu\text{g m}^{-3}$), and Cr ($0.104 \pm 0.010 \mu\text{g m}^{-3}$) were detected at trace levels. Other elements, including Cu, Mn, Cs, P, Y, Sb, Ni, Sn, F, Sr, Br, Pm, U, Pb, Th, Fr, Rb, and V, were quantified in the nanogram range (10 ng m^{-3} to 88 ng m^{-3}). The elemental composition of PM₁₀ particles was also assessed using the geo-accumulation index (I_{geo}) (Fig. 2). The negative values obtained for all elements indicate the presence of elemental contamination within the study site, suggesting minimal pollution. [60].

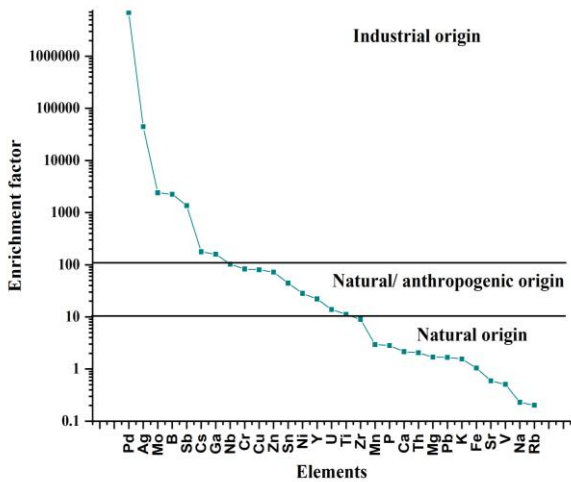


Figure 3. Enrichment Factor (EF) of Metals in PM₁₀

The Enrichment Factor (EF) concept serves as a valuable tool in discerning between natural and human-induced sources of elements. EF values below 5 typically indicate a predominant natural or crustal origin, while values ranging from 5 to 10 suggest a blend of natural and anthropogenic sources. When EF values exceed 10, it points towards primarily anthropogenic origins, often linked to human activities [22, 60]. In this study, the analysis reveals those metals such as Rb, Na, V, Sr, Fe, K, Pb, Mg, Th, Ca, P, and Mn exhibit EF values below 5, indicating their likely derivation from natural crustal sources. Conversely, elements like Zr and Ti display EF values between 5 and 10, implying a combination of natural processes and human activities, such as combustion, construction, or demolition. Finally, elements including U, Y, Ni, Sn, Zn, Cu, Cr, Nb, Ga, Cs, Sb, B, Mo, Ag, and Pd exhibit EF values surpassing 10, strongly indicating their predominantly anthropogenic origin, likely originating from industrial emissions (Fig. 3).

3.2. Source Apportionment and Source Region:

In the extensive 2021 investigation in Nainital, Positive Matrix Factorization (PMF 5.0 version) was applied to analyze PM₁₀. A six-factor solution was deemed the most reliable, involving 22 species (OC, EC, WSOC, B, Na, Mg, Al, P, S, Cl, K, Ca, Ti, Cr, Mn, Fe, Ni, Cu, Zn, Ga, Zr, and Mo) and 40 PM₁₀ samples. To enhance the model's robustness, Mn, Ga, and Mo were considered

weak species, and an extra 10% modelling uncertainty was applied. The PMF analysis results, including source profiles and percentage contributions, are presented in Fig. 4 and Fig. 5 respectively.

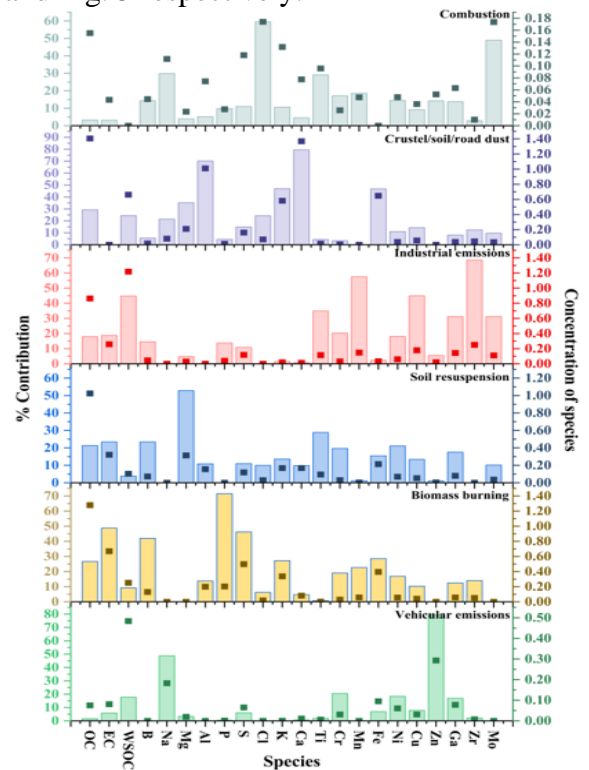


Figure 4: PMF source profile of PM₁₀ at Nainital

The identified factors for PM₁₀ included two dust-related factors (crustal/soil/road dust and soil resuspension), combustion, vehicular emissions, biomass burning, and industrial emissions.

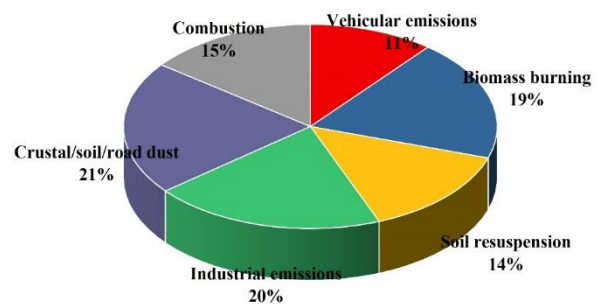


Figure 5: Percentage contribution of the sources extracted by PMF of PM₁₀

Crustal/soil/road dust and soil resuspension factors explained 88% of Mg, indicating a significant influence of soil dust, possibly exacerbated by the tourist-heavy traffic

causing road wear [37-45]. Generally, Ca and Mg are frequently associated with mineral dust and construction activities [25, 46-48]. Given that the sampling site is a tourist hotspot susceptible to the wear and tear of asphalt and concrete roads, primarily due to heavy traffic influence, the increased proportion of crustal elements like Ca and Mg in road dust may result from extensive asphalt and concrete use in road construction [49]. Several other researchers have cited these elements (Ca, Na, Mg, K, and Al) as indicative of a soil dust source in various studies [37-41]. In India, a comprehensive set of marker elements for identifying soil dust includes Al, Si, Ca, Ti, Fe, Pb, Cu, Cr, Ni, Co, and Mn, as discussed in previous studies [42-44]. Combustion, representing 15% of PM₁₀ mass, exhibited high loadings for Cl and Mo, suggesting contributions from coal combustion and industrial activities. Cl is emitted through traffic emissions, predominantly from fuel combustion, and is also a significant contributor to coal combustion [50, 51]. Vehicular emissions, contributing 13%, displayed elevated Na and Zn loadings, indicative of both exhaust and non-exhaust sources such as brake and tire wear [32, 39, 50, 52, 53]. The elements Na, Cu, Zn, and Ca mostly emitted through vehicular exhaustion as these metals are used as additives in motor oil and fuel [37, 51]. Biomass burning contributed 23%, marked by higher loadings for EC, B, P, and S, linked to agricultural residue burning in the nearby Indo-Gangetic plain [18, 54-58]. Also, there were various forest fire events that took place near sampling site, that could also contribute to the biomass burning source. Biomass burning, whether from agricultural residue burning or forest fires, can release phosphorus into the atmosphere. Plant materials contain phosphorus, and when burned, it can be emitted as PM [56-58]. Industrial emissions, characterized by heightened WSOC, Ti, Mn, Cu, Ga, Zr, and Mo, contributed 22% to the PM₁₀ mass [43, 59]. A suite of tracer species, including Ni, Cr, Co, Ga, Cd, Zn, As, Pb, Fe, Cu, Mn, S, and Mo, has been employed in

India to discern specific industrial emissions [28, 37, 43, 59].

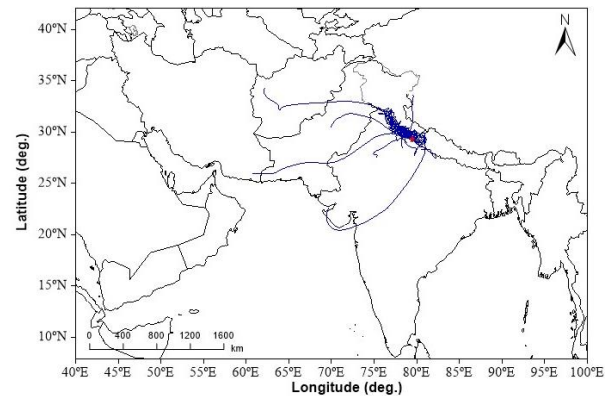


Figure 5: 72 hrs. air mass backward trajectory of PM₁₀ at height 500 m above ground level (AGL) at Nainital

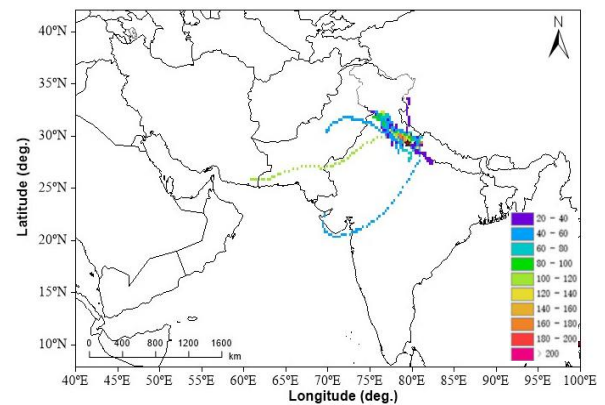


Figure 6. Annual Concentration Weighted Trajectory (CWT) of PM₁₀ over Nainital

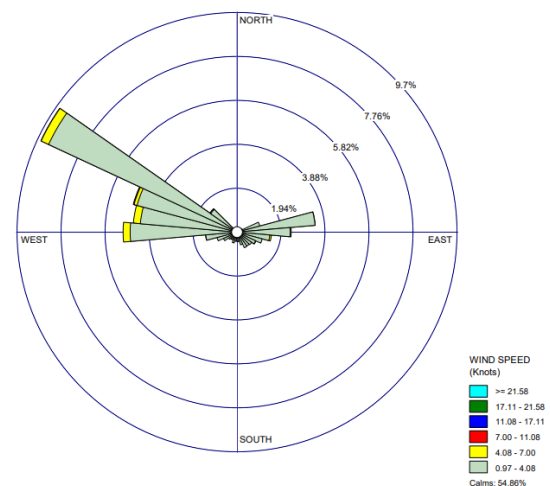


Figure 7: Wind Direction Distribution at Nainital

To comprehend the 72 h. backward trajectories of particulate air masses reaching the sampling site in Nainital, annual trajectories at 500

meters above ground level (AGL) were generated (Fig. 6). Trajectory analysis revealed both local and transboundary origins of PM₁₀, including contributions from northern states, the Thar Desert, and neighboring countries like Pakistan, Afghanistan, Iran, and Nepal [15, 21]. Based on the CWT plot (Fig. 7), it is evident that higher concentrations of PM₁₀ (120-180 $\mu\text{g m}^{-3}$) stem from local emissions. Concentrations ranging between 100-120 $\mu\text{g m}^{-3}$, originating from regional states within the Indo-Gangetic Plain (IGP) and transboundary regions like Pakistan and Iran, are notable. Additionally, concentrations ranging from 60-80 $\mu\text{g m}^{-3}$ are also attributed to local sources. Lower concentrations (20-60 $\mu\text{g m}^{-3}$) are observed from local sources, as well as from regional contributors such as Uttar Pradesh, Madhya Pradesh, Maharashtra, North-western regions, and certain northern regions. Furthermore, contributions from the Arabian Sea and transboundary contributors like Pakistan are discernible in this range. Fig. 8 depicts that the predominant wind contribution originated from the northwest, west, northeast, and east directions locally at the sampling site. Locations such as Nainital bus stop and Mall Road are positioned in the northwest direction from ARIES, suggesting their potential contribution to pollution levels at the study site. This observation underscores the significance of these areas as potential sources of pollutants affecting the study site.

3.3. Health Risk Assessment: Fig. 9 presents the evaluation of EC, HQ, and CR for seven heavy elements (Al, Pb, Cr, Mn, Cu, Zn, and Ni) in both adults and children. Notably, HQ values for Cr and Mn in children, reaching 2.33 and 2.99, respectively, exceeded the acceptable limit of 1, indicating a non-carcinogenic health risk. Similarly, in adults, the HQ value for Mn at 1.28 surpassed the safe limit, suggesting a non-carcinogenic health risk as well. Furthermore, adults exposed to Cr may face a potential carcinogenic risk, as its values exceeded the permissible limit of 10^{-4} . Both Cr and Mn are associated with non-exhaust traffic emissions such as tire or brake wear [25, 27, 53]. Conversely, Al, Pb, Cu, Zn, and Ni exhibited HQ values within the

permissible limits recommended by USEPA, indicating no health hazards associated with these elements. Prakash et al., 2018 explored the carcinogenic risk in Delhi and identified notably increased health risks linked to PM_{1.0}-bound metals, especially for Cr and Ni. The reported risks surpassed safe thresholds for children and approached tolerable limits for adults.

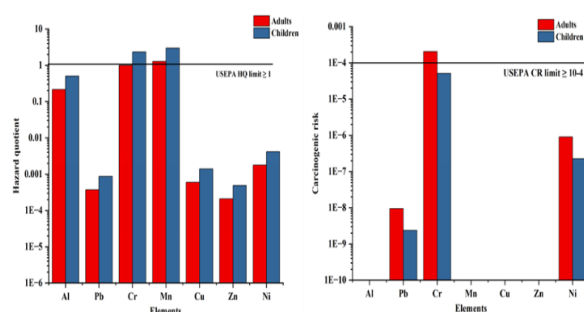


Figure 9: Annual assessment of Hazard Quotient (HQ), and Carcinogenic Risk (CR) of heavy elements on human health

4. Conclusions: In the extensive 2021 study conducted in Nainital, a thorough analysis of PM₁₀, carbonaceous aerosols, and elemental compositions was carried out. The study included assessments of annual concentration averages, Positive Matrix Factorization (PMF)-guided source apportionment, and a health risk evaluation for heavy elements. The average annual PM₁₀ concentration stood at $64 \pm 6 \mu\text{g m}^{-3}$. Carbonaceous aerosols, encompassing OC, EC, WSOC, and SOC, exhibited annual averages of $9.32 \pm 0.82 \mu\text{g m}^{-3}$, with individual components recording concentrations of $4.90 \pm 0.45 \mu\text{g m}^{-3}$, $1.48 \pm 0.12 \mu\text{g m}^{-3}$, $2.72 \pm 0.19 \mu\text{g m}^{-3}$, and $2.97 \pm 0.45 \mu\text{g m}^{-3}$, respectively. The elemental composition, constituting about 16% of the total PM₁₀ mass, highlighted major contributors like Ca, Al, Fe, S, and K, along with trace levels of various elements (Mg, Pd, B, Mo, Zn, Ag, Nb, Ga, Cl, Ti, Zr, Na, and Cr). Source apportionment identified six primary contributors to PM₁₀, including crustal/soil/road dust, soil resuspension, combustion, vehicular emissions, industrial emissions, and biomass burning. Trajectory analysis unveiled transboundary origins of PM₁₀, originating both locally and from northern Indian states,

the Thar Desert, and the Indo-Gangetic Plain. Substantial contributions were also traced back to neighboring countries, such as Pakistan, Afghanistan, Iran, and Nepal. The main wind contribution originates locally from the northwest, west, northeast, and east directions at the sampling site. Nainital bus stop and Mall Road, situated northwest of ARIES, likely contribute to pollution levels at the study site, highlighting their importance as potential pollution sources. The health risk assessment indicated elevated Hazard Quotient (HQ) values for Cr and Mn in children, signaling a non-carcinogenic health risk. Adults exposed to high Cr levels may face potential carcinogenic risks, while elements like Al, Pb, Cu, Zn, and Ni pose no health hazards, aligning with USEPA guidelines. These insights play a pivotal role in shaping public health policies and strategies to mitigate air pollution-related health risks, providing valuable input for policymakers working to enhance ambient air quality and safeguard human health, especially in higher-altitude regions like Nainital.

Acknowledgments: The authors are thankful to the Director, CSIR-NPL, New Delhi and Head, Environmental Sciences & Biomedical Metrology Division, CSIR-NPL, New Delhi for their encouragement and support of this study. Department of Science and Technology, New Delhi is also thankful for financial support.

Conflict of Interest: Authors declare No conflicts of interest.

References:

- [1] S. Fuzzi, U. Baltensperger, K. Carslaw, S. Decesari, H. Denier van der Gon, M. C. Facchini, D. Fowler, I. Koren, B. Langford, U. Lohmann, E. Nemitz, S. Pandis, I. Riipinen, Y. Rudich, M. Schaap, J. G. Slowik, D. V. Spracklen, E. Vignati, M. Wild, M. Williams, and S. Gilardoni, Particulate matter, air quality and climate: lessons learned and future needs, *Atmos. Chem. Phys.*, 15, 2015, 8217–8299.
- [2] T.C. Bond, S.J. Doherty, D.W. Fahey, *et al*, Bounding the role of black carbon in the climate system: a scientific assessment, *J. Geophys. Res. Atmos.*, 118, 2013, 5380–5552.
- [3] S.K. Sharma, N. Choudhary, P. Srivastava, M. Naja, N. Vijayan, G. Kotnala, T.K. Mandal, Variation of carbonaceous species and trace elements in PM₁₀ at a mountain site in the central Himalayan region of India, *J. Atmos. Chem.*, 77, 2020, 1–14.
- [4] A.K. Srivastava, K. Ram, P. Pant, P. Hegde, J. Hema, Black carbon aerosols over Manora Peak in the Indian Himalayan foothills: implications for climate forcing, *Environ. Res. Lett.*, 7(1), 2012, 014002.
- [5] C. Venkataraman, G. Habib, A. Eiguren-Fernandez, A.H. Miguel, S.K. Friedlander, Residential biofuel in South Asia: Carbonaceous aerosol emissions and climate impacts, *Science* 307(5714), 2005, 1454–1456.
- [6] A. Kumar, A.K. Attri, Biomass combustion a dominant source of carbonaceous aerosols in the ambient environment of western Himalayas, *Aerosol Air Qual. Res.*, 16(3), 2016, 519–529.
- [7] Shivani, R. Gadi, R. Kumar, M. Sharma, S.K. Sharma, *et al*, Levels and Sources of organic compounds in Fine Particulate Matter (PM_{2.5}) over Delhi and National Capital Region of India, *Environ. Sci. Pollut. Res.* 25(31), 2018, 31071–31090.
- [8] Shivani, R. Gadi, M. Saxena, S.K. Sharma, T.K. Mandal, Short Term Degradation of Air Quality during Major Firework Events in Delhi, India, *Meteoro. Atmos. Phys.*, 131(4), 2019, 753–764.
- [9] Shivani, R. Gadi, S.K. Sharma, T.K. Mandal, Seasonal variation, source apportionment and source attributed health risk of carbonaceous aerosols in fine particulate matter over National Capital Region, India, *Chemosphere* 237, 2019, 124500.
- [10] R. Gadi, Shivani, S.K. Sharma, T.K. Mandal, Source apportionment and health risk assessment of organic constituents in fine ambient aerosols (PM_{2.5}): a complete year study over National Capital Region of India, *Chemosphere*, 221, 2019, 583–596.
- [11] J.S. Lighty, J.M. Veranth, A.F. Sarofim, Combustion aerosols: factors governing their size and composition implications to human

- health, *J. Air Waste Manag. Assoc.*, 50(9), 2000, 1565–1618.
- [12] C.A. Pope, M. Ezzati, D.W. Dockery, Fine-particulate air pollution and life expectancy in the United States, *New England Journal of Medicine*. 360(4), 2009, 376–386.
- [13] K. Gajananda, J.C. Kuniyal, G.A. Momin, P.S.P. Rao, P.D. Safai, S. Tiwari, K. Ali, Trend of atmospheric aerosols over the north northwestern Himalayan region, India, *Atmos. Environ.* 39, 2005, 4817–4825.
- [14] R. Sheoran, U.C. Dumka, D.G. Kaskaoutis, G. Grivas, *et al*, Chemical composition and source apportionment of total suspended particulate in the central Himalayan region, *Atmosphere*, 12, 2021, 1128.
- [15] N. Choudhary, P. Srivastava, M. Dutta, S. Mukherjee, A. Rai, *et al*, Seasonal Characteristics, Sources and Pollution Pathways of PM₁₀ at High Altitudes Himalayas of India, *Aerosol Air Qual. Res.*, 22(7), 2022.
- [16] N. Choudhary, A. Rai, J.C. Kuniyal, P. Srivastava, R. Lata, *et al*, Chemical Characterization and Source Apportionment of PM₁₀ Using Receptor Models over the Himalayan Region of India, *Atmosphere*, 14(5), 2023, 880.
- [17] R.K. Singh, Assessment of Ambient Air Pollution and Mitigation Strategies towards Achieving Air Quality Index (AQI) in the Indian Himalayan Region, *Int. J. Sci. Res.*, 9(12), 2019.
- [18] K. Ram, M.M. Sarin, Spatio-Temporal Variability in Atmospheric Abundances of EC, OC and WSOC over Northern India, *J. Aerosol Sci.*, 41, 2010, 88–98.
- [19] P. Hegde, K. Kawamura, H. Joshi, M. Naja, Organic and inorganic components of aerosols over the central Himalayas: winter and summer variations in stable carbon and nitrogen isotopic composition, *Environ. Sci. Poll. Res.*, 23, 2016, 6102–6118.
- [20] J. Chow, J. Watson, L.W.A. Chen, W. Arnott, H. Moosmuller, K. Fung, Equivalence of elemental carbon by thermal/optical reflectance and transmittance with different temperature protocols, *Environ. Sci. Technol.*, 38, 2004, 4414–4422.
- [21] S.K. Sharma, S. Mukherjee, N. Choudhary, A. Rai, A. Ghosh, *et al*, Seasonal variation and sources of carbonaceous species and elements in PM_{2.5} and PM₁₀ over the eastern Himalaya, *Environ. Sci. Pollut. Res.*, 28, 2021, 51642–51656.
- [22] S.K. Sharma, T.K. Mandal, M. Saxena, A. Sharma, A. Datta, T. Saud, Variation of OC, EC, WSIC and trace metals of PM₁₀ in Delhi, India. *J Atmos Solar-Terres Phys* 113, 2014, 10–22.
- [23] S. Gupta, S. Shankar, J. C. Kuniyal, *et al.*, Identification of sources of coarse mode aerosol particles (PM₁₀) using ATR-FTIR and SEM-EDX spectroscopy over the Himalayan Region of India. *Environ. Sci. Pollut. Res.* **31**, 2024, 15788–15808.
- [24] R.K. Hooda, N. Kivekäs, M. C. Coen, P. Pietikäinen, V. Vakkari, J. Backman, S.V. Henriksson, E. Asmi, M. Komppula, H. Korhonen, P. Hyvärinen, H. Lihavainen, Driving Factors of Aerosol Properties Over the Foothills of Central Himalayas Based on 8.5 Years Continuous Measurements. *Journal of Geophysical Research: Atmospheres*, 123(23), 2018, 13,421-13,442.
- [25] A. Rai, S. Mukherjee, A. Chatterjee, N. Choudhary, G. Kotnala, T.K. Mandal, S.K. Sharma, Seasonal variation of OC, EC, and WSOC of PM₁₀ and their cwt Analysis over the eastern Himalaya, *Aerosol Sci. Eng.*, 4, 2020, 26–40.
- [26] M. Mishra, U.C. Kulshrestha, Source impact analysis using char-EC/Soot-EC ratios in the central Indo-Gangetic Plain (IGP) of India, *Aerosol Air Qual. Res.*, 21, 2021, 200628.
- [27] M. F. D. Gianini, A. Fischer, R. Gehrig, A. Ulrich, A. Wichser, C. Piot, J.L. Besombes, C. Hueglin, Comparative source apportionment of PM₁₀ in Switzerland for 2008/2009 and 1998/1999 by positive matrix factorisation, *Atmos. Environ.*, 54, 2012, 149–158.
- [28] Y. Li, B. Liu, Z. Xue, Y. Zhang, X. Sun, C. Song, *et al*, Chemical characteristics and source apportionment of PM_{2.5} using PMF modelling coupled with 1-hr resolution online air pollutant dataset for Linfen, China, *Environmental Pollution*, 263(B), 2020, 114532.

- [29] P. Rai, J.G. Slowik, M. Furger, I. El-Haddad, S. Visser, highly time-resolved measurements of element concentrations in PM₁₀ and PM_{2.5}: Comparison of Delhi, Beijing, London, and Karakow, *Atmos. Chem. Phys.*, 21, 2021, 717-730.
- [30] R. Banoo, S. Gupta, R. Gadi, *et al.* Chemical characteristics, morphology and source apportionment of PM₁₀ over National Capital Region (NCR) of India, *Environ. Monit. Assess.*, 196, 2024, 163.
- [31] N. Zheng, J. Liu, Q. Wang, Z. Liang, Science of the total environment health risk assessment of heavy metal exposure to street dust in the zinc smelting district, Northeast of China, 408(4), 2010, 726-733.
- [32] J. Prakash, T. Lohia, A.K. Mandariya, G. Habib, T. Gupta, S.K. Gupta, Chemical characterization and quantitative assessment of source-specific health risk of trace metals in PM_{1.0} at a road site of Delhi, India, *Environ. Sci. Pollut. Res.*, 25, 2018, 8747-8764.
- [33] S. Gupta, S.K. Sharma, T.K. Mandal, Elemental Analysis and Health Risk Assessment of PM_{2.5} at an Urban Site of Delhi, Chapter 16, Recent Advances in Metrology, Sanjay Yadav, Naveen Garg, Shankar G. Aggarwal, Shiv Kumar Jaiswal, Harish Kumar, Venu Gopal Achanta, Springer Science and Business Media, 2023.
- [34] D. Sah, P.K. Verma, K.M. Kumari, A. Lakhani, Characterisation, Sources and Health Risk of Heavy Metals in PM_{2.5} in Agra, India, *Exposure and Health*, 49, 2022, 10147.
- [35] Q. Zhang, D.R. Worsnop, M.R. Canangaratna, J.L. Jimenez, Hydrocarbon-like and oxygenated organic aerosols in Pittsburgh: Insights into sources and processes of organic aerosol, *Atmos. Chem. Phys.*, 5, 2005, 3289-3311.
- [36] A. Chatterjee, S. Mukherjee, M. Dutta, A. Ghosh, S.K. Ghosh, A. Roy, High rise in carbonaceous aerosols under very low anthropogenic emissions over eastern Himalaya, India: Impact of lockdown for COVID-19 outbreak, *Atmos. Environ.*, 244, 2021, 117947.
- [37] B. Gugamsetty, H. Wei, C.N. Liu, A. Awasthi, S.C. Hsu, *et al.* Source Characterization and Apportionment of PM₁₀, PM_{2.5} and PM₁ by Using Positive Matrix Factorization, *Aerosol Air Qual. Res.*, 12, 2012, 476-491.
- [38] A. Waked, O. Favez, L.Y. Alleman, C. Piot, J.E. Petit, *et al.* Source apportionment of PM₁₀ in a north-western Europe regional urban background site (Lens, France) using positive matrix factorization and including primary biogenic emissions, *Atmos. Chem. Phys.*, 14, 2014, 3325-3346.
- [39] M.F. Khan, M.T. Latif, W.H. Saw, N. Amil, M.S.M. Nadzir, M. Sahani, N.M. Tahir, J.X. Chung, Fine particulate matter in the tropical environment: monsoonal effects, source apportionment, and health risk assessment, *Atmos. Chem. Phys.*, 16, 2016, 597-617.
- [40] J.H. Jeong, Z.H. Shon, M. Kang, S.K. Song, Y.K. Kim, J. Park, H. Kim. Comparison of source apportionment of PM_{2.5} using receptor models in the main hub port city of East Asia: Busan, *Atmospheric Environment*, 148, 2017, 115-127.
- [41] M. Manousakas, M. Furger, K.R. Daellenbach, F. Canonaco, G. Chen, A. Tobler, P. Rai, *et al.* Source identification of the elemental fraction of particulate matter using size segregated, highly time-resolved data and an optimized source apportionment approach, *Atmospheric Environment X*, 14, 2022, 100165.
- [42] I. Gupta, A. Salunkhe, R. Kumar, Source Apportionment of PM₁₀ by Positive Matrix Factorization in Urban Area of Mumbai, India, *The Scientific World Journal*, 2012, 585791.
- [43] T. Banerjee, V. Murari, M. Kumar, M.P. Raju, Source apportionment of airborne particulates through receptor modelling: Indian scenario, *Atmos. Res.*, 164, 2015, 167-187.
- [44] S. Jain, S.K. Sharma, N. Choudhary, R. Masiwal, M. Saxena, *et al.* Chemical characteristics and source apportionment of PM_{2.5} using PCA/APCS, UNMIX and PMF at an urban site of Delhi, India, *Environ. Sci. Pollut. Res.* 24, 2017, 14637-14656.
- [45] S.K. Sharma, T.K. Mandal, M.K. Srivastava, *et al.* Spatio-temporal variation in chemical characteristics of PM₁₀ over Indo

- Gangetic Plain of India, *Environ. Sci. Pollut. Res.* 23, 2016, 18809–18822.
- [46] N. Bukowiecki, P. Lienemann, M. Hill, M. Furger, A. Richard, F. Amato, A.S.H. Prevot, U. Baltensperger, B. Buchmann, R. Gehrig, PM₁₀ emission factors for non-exhaust particles generated by road traffic in an urban street canyon and along a freeway in Switzerland, *Atmos. Environ.*, 44, 2010, 2330–2340.
- [47] L.R. Crilley, F. Lucarelli, W.J. Bloss, R.M. Harrison, D.C. Beddows, G. Calzolari, S. Nava, G. Valli, V. Bernardoni, R. Vecchi, Source apportionment of fine and coarse particles at a roadside and urban background site in London during the 2012 summer Clear fLo campaign, *Environ. Pollut.*, 220, 2016, 766–778.
- [48] W. Maenhaut, Source apportionment revisited for long-term measurements of fine aerosol trace elements at two locations in southern Norway, *Nucl. Instrum. Meth. B*, 417, 2017, 133–138.
- [49] D. Fullova, D. Durcanska, J. Hegrova, Particulate matter mass concentrations produced from pavement surface abrasion, *MATEC Web Conf.*, 117, 2017, 00048.
- [50] N. Jiang, Q. Li, F. Su, Q. Wang, X. Yu, P. Kang, R. Zhang, X. Tang. Chemical characteristics and source apportionment of PM_{2.5} between heavily polluted days and other days in Zhengzhou, China, *Journal of Environmental Sciences*, 66, 2018, 188–198.
- [51] Q. Dai, B. Liu, X. Bi, J. Wu, D. Liang, Y. Zhang, Y. Feng, P.K. Hopke, Dispersion normalized PMF provides insights into the significant changes in source contributions to PM_{2.5} after the COVID-19 outbreak, *Environ. Sci. Technol.*, 54 (16), 2020, 9917–9927.
- [52] T. Grigoratos, G. Martini, Brake wear particle emissions: a review, *Environ. Sci. Pollut. Res.*, 22, 2015, 2491–2504.
- [53] A. Roy, M. Mandal, S. Das, M. Kumar, R. Popek, A. Awasthi, *et al*, Non-exhaust particulate pollution in Asian countries: A comprehensive review of sources, composition, and health effects, *Environmental Engineering Research*, 29(3), 2024.
- [54] A. Singhal, G. Habib, R.S. Raman, T. Gupta, Chemical characterization of PM_{1.0} aerosol in Delhi and source apportionment using positive matrix factorization, *Environ. Sci. Pollut. Res.* 24, 2017, 445 – 462.
- [55] S. Jain, S.K. Sharma, M.K. Srivastava, *et al*, Source Apportionment of PM₁₀ Over Three Tropical Urban Atmospheres at Indo-Gangetic Plain of India: An Approach Using Different Receptor Models, *Arch. Environ. Contam. Toxicol.* 76, 2019, 114–128.
- [56] S.K. Akagi, R.J. Yokelson, C. Wiedinmyer, M.J. Alvarado, J.S. Reid, *et al*, Emission factors for open and domestic biomass burning for use in atmospheric models, *Atmos. Chem. Phys.*, 11, 2011, 4039–4072.
- [57] S. Bhuvaneshwari, H. Hettiarachchi, J.N. Meegoda, Crop Residue Burning in India: Policy Challenges and Potential Solutions, *Int. J. Environ. Res. Public Health*, 16, 2019, 832.
- [58] Y. Meng, R. Li, L. Cui, Z. Wang, H. Fu, Phosphorus emission from open burning of major crop residues in China, *Chemosphere*, 288, 2022, 132568.
- [59] S.K. Sharma, T.K. Mandal, M. Saxena, A. Sharma, R. Gautam, Source apportionment of PM₁₀ by using positive matrix factorization at an urban site of Delhi, India, *Urban Climate*, 10, 2014, 656–670.
- [60] M.I.C. Abdullah, A.S.R.M. Sah, H. Haris, Geo-accumulation Index and Enrichment Factor of Arsenic in Surface Sediment of Bukit Merah Reservoir, Malaysia, *Trop. Life Sci. Res.* 31(3), 2020, 109–125.

Physico-chemical and Microbiological Changes in Degradation of Agri-residue under Pit Compositing

Livleen Shukla¹, Roaf A. Parray², K Annapurna¹, Satish D Lande², Indra Mani^{2,4}, Deebea Kamil^{3*}

¹Division of Microbiology, Indian Council of Agricultural Research (ICAR)-Indian Agricultural Research Institute (IARI), New Delhi-110012, India

²Division of Agricultural Engineering, ICAR-IARI, New Delhi-110012, India

³Division of Plant Pathology, ICAR-IARI, New Delhi-110012, India

⁴Vasantrao Naik Marathwada Krishi Vidyapeeth, Parbhani, Maharashtra- 431402, India

Volume 1, Issue 2, March 2024

Received: 10 January, 2024; Accepted: 5 March, 2024

DOI: <https://doi.org/10.63015/9s-2411.1.2>

*Corresponding author email: lshukla65@gmail.com

Abstract: Management of crop residues has remained a major challenge due to lack of easily adaptable and affordable interventions at farmer's field. Cellulolytic bacteria and fungi have been recommended for recycling lignocellulosic-rich organic matter and to convert it into nutrient rich compost. However, these inoculants need to be generated on commercial scale for handling large volume of biomass. Also, the microbial formulation should also be capable of degrading diverse type of agri-residues. Seven fungal strains, namely *Aspergillus awamori* (F-18), *Aspergillus nidulans*, *Trichoderma viride*, *Trichoderma longibrachitum*, *Drechslera halodes*, *Eupenicillium crustaceum* and *Paecilomyces variotii* were characterized based on shelf life, functional activity to make consortium for degradation of various agro and horticultural residues using pit method of composting. An experiment was laid in cemented pits using four different substrates-maize cobs and stalks, paddy straw, kinnow fruit waste and flower waste for rapid degradation. The results revealed a maximum increase in spore count with *Paecilomyces variotii* followed by *Eupenicillium crustaceum* and *Drechslera halodes*. Out of four different additives, glycerol was found to be most suitable additive for incubation of selected fungi. The results on microbial population revealed highest bacterial population in flower waste and highest actinobacterial population in kinnow waste. It was also observed that inoculated organic waste degraded faster than un-inoculated wastes. As the degradation process progressed, total N also increased with time and varied from 1.1 to 1.5 percent. Flower and kinnow waste degradation was completed in 45 days while that of maize and paddy straw in 75 and 90 days, respectively. The pH range was 6.5-8.0 in all the substrates but in inoculated substrates, the range of pH was 7.2-7.6, while electrical conductivity (EC) was 1.4-3.6. The highest humus% was found with paddy straw followed by maize, flower and kinnow. The final product also showed variation in K% and S% which were found to be 0.6% -1.8% and 0.1% -0.20%, respectively.

Keywords: Cellulolytic fungi; inoculant; *In-situ* degradation, agri-residue, consortium

1. Introduction: During post-harvest processing, major crops in India contribute to heavy amount of residues and byproducts. Cereal crops viz., rice, wheat, maize and millets

contribute 70% [1], while rice crop alone contributes 34% to the crop residues. India generates about 620 million tons of the crop residues and rice contributes the highest amount

(154 Mt) residues followed by wheat (131 Mt) [2]. Burning of one tonne of rice straw was estimated for loss of 5.5 kg Nitrogen, 2.3 kg phosphorus, 25 kg potassium and 1.2 kg sulphur besides, organic carbon. Generally, crop residues of different crops contain 80% of nitrogen (N), 25% of phosphorus (P), 50% of sulphur (S) and 20% of potassium (K). If the crop residue is incorporated or retained in the soil itself, it gets enriched, particularly with organic C and N [3]. The states in the North-Western regions of India are facing intense air pollution, particularly during the October–December months, which is the main agricultural harvest season in the country. During these months, the smoke plume emitted from the burning of rice paddy stubble in the open travels across the entire northwest region causing high PM concentrations and dense haze throughout the National Capital Region (NCR) of New Delhi [4]. The on-farm burning of crop residues has intensified in recent years due to unavailability of low cost and easily adaptable technologies for its handling and management and short time window availability between harvesting and sowing of crops. In an era of intensive cropping, the disposal of large quantities of crop residues has become a menace. Inadequate organic waste management leads to a plethora of problems such as environmental pollution, eutrophication, and aesthetic damage to urban landscape, greenhouse gases emission and effects on human health. Unwise and non-scientific disposal of wastes not only poses a grave threat to environmental quality but also results in loss of economic value of wastes. Since organic wastes are an abundant pool of organic matter and valuable plant nutrients, agricultural recycling of these wastes appears to be a promising alternative enabling value addition and their resourceful utilization [5]. *In-situ* and *ex-situ* management of crop residues have remained a major challenge due to lack of easily adaptable and affordable mechanical and microbiological technologies at farmers' field. Cellulose is recognized as the most abundant biopolymer on earth, which is the major

component of agricultural residues [6]. The biopolymer can be degraded into glucose by cellulases such as endoglucanase, cellobiohydrolase and β -glucosidase [7]. Enzymatic degradation of cellulosic biomass is important for sustainable utilization of agricultural residues. Therefore, production of high efficient and economic cellulolytic enzymes, including cellulase, xylanase, and glycosyl hydrolases, has received a great attention. Some important microbes from different niches have been identified to have an extracellular enzyme system to hydrolyze cellulose for metabolism requirement [8]. Chen et al. 2020 reported that *Fictibacillus* sp YS-26 can efficiently degrade different lignocellulosic agricultural residues by producing cellulolytic enzymes viz., α -amylase, pectinase, protease and xylanase [9]. Cellulolytic fungi like *Aspergillus awamori*, *Aspergillus nidulans*, *Trichoderma viride* and *Phanerochaete chrysosporium* are recommended for recycling lignocellulosic-rich organic matter and to convert it into nutrient rich compost. However, these inoculants need to be generated on commercial scale for handling large volume of biomass. There are two major methods of inoculum production—solid state and liquid state fermentation. Both liquid and solid-state fermentations have some disadvantages like odour, slow process, and storage and transport problem especially when larger quantity is required. Viability and shelf life of spores are other issues associated with the current bio-inoculum production techniques. Also, the microbial formulation should also be capable of degrading diverse type of agri-residues. Hence, a complete knowledge of the mass production of microbial inoculants and proper delivery system is a critical impediment to microbial products. It is important to consider that the formulation should have shelf life with retained biological activity for up to a year preferably at ambient temperatures, which is a challenging task as it requires greater effort in terms of funding and research [10]. Therefore, it is essential to develop a high throughput protocol that

employs common and cost-effective growth medium, should be easy to operate and consumes less time for mass production of fungal spores. In view of this, the present work was carried out to produce spores in mass of potential fungal strains which can be used for degradation of various agri-residues like paddy straw, garden waste, fruit waste and convert them to valuable product i.e., compost and to monitor the chemical and biological changes during composting.

2. Materials and Methods

2.1 Selection of Fungal Strains: Seven fungi, selected on the basis of their lignocellulolytic potential, namely *Aspergillus awamori* (F-18), *Aspergillus nidulans*, *Trichoderma viride*, *Trichoderma longibrachitum*, *Drechslera halodes*, *Eupenicillium crustaceum* and *Paecilomyces variotii* were employed in the present study. *Aspergillus awamori* (F-18), *Aspergillus nidulans* and *Trichoderma viride* were obtained from Division of Microbiology, ICAR-Indian Agricultural Research Institute (IARI), New Delhi while other fungi were isolated, characterized under present investigation. All isolates were maintained on Potato dextrose agar medium and later cultivated in modified jaggery medium [11].

2.2 Production of Fungal Spores: The mass production of spores was carried out on sorghum grains using solid state fermentation. In this procedure, 500g of sorghum grains were boiled, air dried and then coated with 4% calcium carbonate and 2% calcium sulphate. The coated grains were sterilized in autoclave bags at 15 lbs pressure and at a temperature of 121°C for 1 hour. The sterilized bags were cooled to room temperature and inoculated with selected fungi individually using their spores.

2.4 Study of Physico-chemical and Microbiological changes during degradation process: During the degradation of different substrates, different hydrolytic enzymes being

The inoculated bags were incubated at 30°C for 10 days. After 10 days, the bags were sieved on a sieve machine having different mesh size from 0.5 mm-2.0 mm and spores were collected in small plastic bottles.

2.3 Study of Characteristic Features of Selected Fungal Strains: The different fungal strains were characterized based on shelf life, functional activity as following:

i) Shelf life: Four different additive agents *viz.* vegetable oil, glycerol, tween-80 and paraffin oil were used for study of shelf life of fungal spores. Mixture of spore powder (1g) was incubated at room temperature for shelf-life evaluation. Samples were taken out periodically and plate count method was used for the viability of spores.

ii) Functional activity: The functional activity of spores was evaluated by inoculating 500 mg spores in 5 liters of modified jaggery medium and incubated for 4 days. Fungal mat was mixed uniformly and used as compost inoculum for rapid degradation of substrates. Fungal mat of all the seven fungi was mixed in equal proportion to make consortium for degradation of various agro and horticultural residues using pit method of composting. An experiment was laid in cemented pits of Division of Microbiology, ICAR-IARI, New Delhi using four different substrates namely maize cobs and stalks, paddy straw, kinnow fruit waste and flower waste for rapid degradation. Two cemented pits (1 x 2 x 8 m), i.e., one for test and other as control, for each substrate were filled with 100 kg of selected substrate followed by spraying and thorough mixing of liquid inoculum with the dose of 5 litres per tonne. Throughout the experiment, moisture was maintained at 80% and turning of the material was done periodically after 15, 30 and 60 days.

the mediators of degradative processes, play an important role in degradation [12] and therefore, the changes in activities of enzymes, *viz.*, cellulose, xylanase and pectinase were studied

as these are responsible for the hydrolysis of cellulose, hemicellulose and pectins. The samples were collected periodically and analysed for physico-chemical and microbiological parameters viz. cellulase and xylanase [13], pectinase [14], organic carbon [9], total N by Kjeldahl method [15]. In addition, humic substances were also determined [16] and standard procedure was used for the enumeration of microorganisms. The total microbial populations of bacteria, fungi and actinobacteria were determined.

3. Results and Discussion

Sporulation Efficiency: Different fungi were observed to have varying sporulation ability (Table 1). It was observed that the fungal spore count after 10 days of inoculation was higher

Another study conducted by [14] showed that *Trichoderma viride* yielded 3×10^{18} spores per ml of suspension on paddy as a substrate at the seventh day of inoculation.

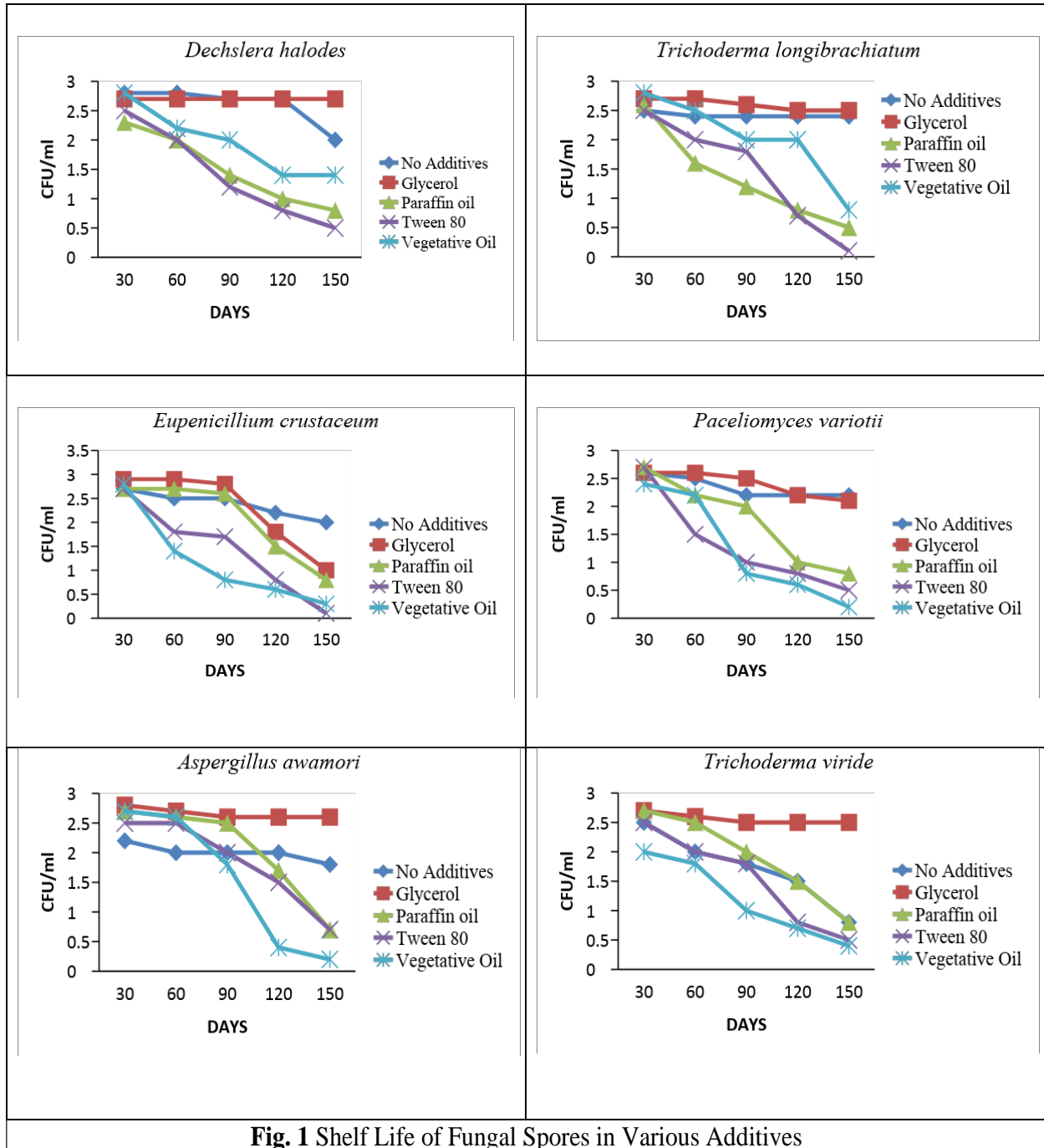
Shelf life of spores: The spores of each fungal isolate were evaluated for shelf-life in four additives with dry powder of spores as control at room temperature for 150 days. The spore count of *Aspergillus awamori*, *Trichoderma viride*, *Trichoderma longibrachiatum*, *Drechslera halodes*, *Eupenicillium crustaceum* and *Paecilomyces variotii* showed that glycerol was found to be the most suitable additive among all the four additives and showed maximum count of spores in 150 days and hence longer shelf-life of spores. The effectiveness of microbial inoculants mainly depends on the type

Table 1: Mass production of spores on sorghum grains

S. no	Fungal strains	Spore count		Fold efficiency
		Initial (10^9)	Final (10^{12})	
1	<i>Aspergillus awamori</i>	3.0	3.3	110
2	<i>Aspergillus nidulans</i>	1.5	2.1	140
3	<i>Trichoderma viride</i>	2.4	2.6	108
4	<i>Trichoderma longibrachiatum</i>	2.0	3.4	170
5	<i>Dechslerahalodes</i>	2.2	2.9	132
6	<i>Eupenicillium crustaceum</i>	1.3	1.8	138
7	<i>Paecilomyces variotii</i>	1.6	3.0	188
	C.D. (@5 %)	0.24	0.30	-

than the initial stage. Fold increase in sporulation varied from 110 to 118 and the maximum increase in spore count was observed with *Paecilomyces variotii* followed by *Eupenicillium crustaceum* and *Drechslera halodes*. In general, it was observed that all the selected fungal strains were able to produce spores in sufficient quantity as required for rapid degradation of various agro-residues. On the fourth day in surface culture inoculation, *Aspergillus awamori* showed a spore formation of $5.70 \pm 0.20 \times 10^8$ per ml of suspension [2].

of formulation and the delivery technology which can increase the shelf lives for few months to year [10]. The spore count for all fungal strains remained stable in glycerol except for *Eupenicillium crustaceum* which showed a marginal decrease in spore count after 150 days of storage (Fig. 1). Similar results were obtained by [16] that showed glycerol as an additive at 3% and 6% can increase the shelf life of *Trichoderma* sp. from 4-5 months to 7 months. Vegetable oil was not found suitable additive as the spore count of all the fungal strains



drastically decreased after 30 days of storage. The spore count in paraffin oil varied with fungal strains and shelf- life ranged from 60-90 days only. The spore powder stored at room temperature for all the fungal strains also showed stable count in 120 days. Hence, the present study was carried out keeping in view

the criteria of low production cost and ease in handling while developing a microbial formulation.

Microbial population dynamics during degradation: The microbial population at various stages of degradation was also determined (Table 2a & 2b). The bacterial and

actinobacterial population were found to increase upto 30 days and then declined, while fungal

compost and the presence or appearance of some microorganisms also reflect the quality of

Table 2(a) Changes in microbial population during composting of various waste

Treatments	Bacteria (X 10 ⁸ cfu g ⁻¹ soil)				Fungi (X 10 ³ cfu g ⁻¹ soil)				Actinobacteria (X 10 ⁴ cfu g ⁻¹ soil)			
	Days				Days				Days			
	0	15	30	45	0	15	30	45	0	15	30	45
MCS	229	235	278	269	10	15	18	07	36	169	190	160
MCS+ MC	231	257	264	271	11	26	32	22	43	174	203	172
FW:DL(1:1)	241	264	309	336	08	11	13	10	30	156	106	221
FW:DL(1:1) + MC	226	284	321	199	10	27	31	22	28	134	184	231
KW:DL (1:1)	201	291	334	241	12	18	22	18	34	148	203	162
KW:DL(1:1)+ MC	225	269	321	195	12	26	30	20	21	114	221	211

population first increased upto 45 days and then it was found to be stable. The highest bacterial and actinobacterial populations were observed in flower waste and kinnow waste, respectively, whereas fungal population was almost same in all the treated wastes. The study carried out by [17] suggested that the number of cellulolytic microorganisms was constantly and significantly higher in the treatment with fungal inoculation, depicting that the initial inoculation significantly enhanced the population density of cellulolytic microorganisms. On the other hand, in the same study, during the thermophilic stage, at the time of start no significant effect on population density of cellulolytic microorganisms, depicting that the added ligno-cellulolytic fungi were partially killed or inactivated during the thermophilic stage. Fungi as reflected by their population were found to be involved in degradation process. The succession of microbes plays a key role in degradation of substrates and converting to

maturing. In the present study dilution plating technique was used which clearly showed variation in microbial population with various substrates. During the degradation of maize, paddy straw, kinnow and flower waste, the cellulose activity increased at 30 days in the fungal consortium applied treatments and it declined after 60 days in maize and paddy straw while in kinnow and flower degradation complete decline was observed by 45 days (Fig. 2 a). However, in a degradation study conducted by [15], *Aspergillus niger* was reported to produce cellulase when incubated with paddy straw maximally at 48 hours and minimum at 24 hours. The initial xylanase activity in all the substrates showed an increase after 15 days and the maximum activity increased upto 60 days in case of inoculated paddy straw and maize waste and declined later on (Fig. 2 b). The xylanase enzyme produced by *Aspergillus* sp. is also found to be efficient in pup bleaching [15]. This observation

Table 2(b) Changes in microbial population during composting of Paddy straw

Treatments	Bacteria (X 10 ⁸ cfu g ⁻¹ soil)					Fungi(X 10 ³ cfu g ⁻¹ soil)					Actinomycetes(X 10 ⁴ cfug ⁻¹ soil)				
	Days					Days					Days				
	0	15	30	45	60	0	15	30	45	60	0	15	30	45	60
PS	216	236	248	250	253	11	16	19	20	22	20	152	189	206	135
PS+ MC	223	251	279	291	223	10	23	29	35	30	24	168	199	221	153

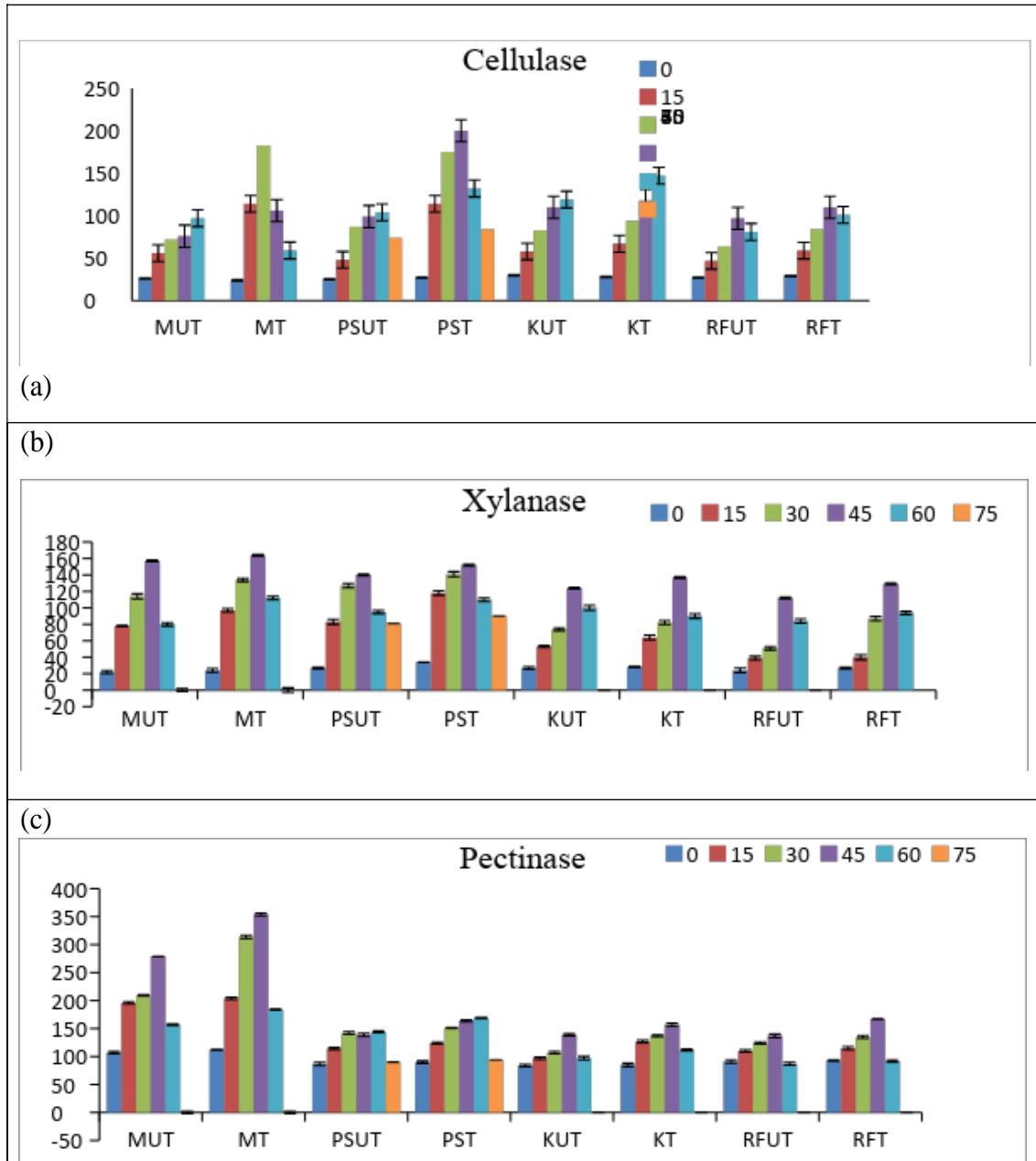


Fig. 2 Enzymatic activity of waste during degradation (mg reducing sugar kg⁻¹dry matter h⁻¹)

MUT: Maize Untreated	MT: Maize treated	PSUT: Paddy Straw Untreated
PST: Paddy Straw Treated	KUT: Kinnow Untreated	KT: Kinnow Treated
RFUT: Flower Untreated	RFT: Flower Treated	

on cellulase and xylanase activity shows that cellulose and hemicellulose content of the substrates are degraded using fungal consortium. During composting of various substrates,

pectinase activity was also found to vary with time (Fig. 2 c). The research work done on cellulase, protease activities in composts prepared using pig slurry, horse manure and straw showed

Table 3: Changes in C:N Ratio during degradation in Pits

	Days						
	0	15	30	45	60	75	90
Maize Untreated	51.00	41.00	39.00	32.00	28.00	-	22.00
Maize Treated	52.00	40.00	38.00	29.00	27.00	-	20.00
Paddy straw Untreated	50.00	40.00	32.00	30.00	28.00	26.00	25.00
Paddy straw Treated	52.00	41.00	30.00	29.00	25.00	22.00	22.00
Flower Untreated	48.00	41.00	38.00	37.00	-	-	-
Flower Treated	49.00	38.00	35.00	25.00	-	-	-
Kinnow Untreated	42.00	39.00	31.00	29.00	-	-	-
Kinnow Treated	41.00	37.00	30.00	25.00	-	-	-

lower enzyme activities than the present work. A study by [18], after assessing 16 compost quality parameters for seven different substrates at five different stages, confirmed that the consortia of fungal inoculants *viz.*, *Trichoderma viride*, *Rhizomucor pussillus*, *Aspergillus awamori* and *Aspergillus flavus* are able to efficiently decompose all the crop residues. The changes in total organic carbon content were also determined during degradation of various substrates. The initial organic carbon of substrates varied from 40.9 % to 49.8%. As the decomposition progressed, the organic carbon content decreased and at the last stage of composting, the lowest organic carbon content was observed with maize waste after 60 days followed by flower waste after 45 days. Similar results were reported by [12] on organic carbon mineralization in paddy straw degradation, where 55% of organic carbon mineralization took place at a temperature of 27°C in 160 days. It was also observed that inoculated organic waste degraded faster than uninoculated wastes. In the present study, at the initial stages, the total N content of different wastes varied from 0.7 % to 1.0%, where the maximum was found in paddy straw followed by maize waste, flower waste and kinnow waste. As the degradation process progressed, the total N also increased with time and varied from 1.1% to 1.5%. Similarly, the initial C:N ratio varied in all the substrates, paddy straw and maize had high C:N ratio as compared to flower waste and Kinnow waste. Flower and kinnow waste degradation was completed in 45 days while in

maize and paddy straw, the same were degraded in 75 days and 90 days, respectively. Thus, to reach the ideal C: N ratio of 20:1, the time of decomposition varied with substrates (Table 3). Although, C:N ratio is one of the parameters of maturity of compost, the stability of compost is also very important factor and the extent of organic matter stabilized is also helpful. The finished product was analyzed for phytotoxicity, humus%, pH, EC, S% and K% (Fig. 3).

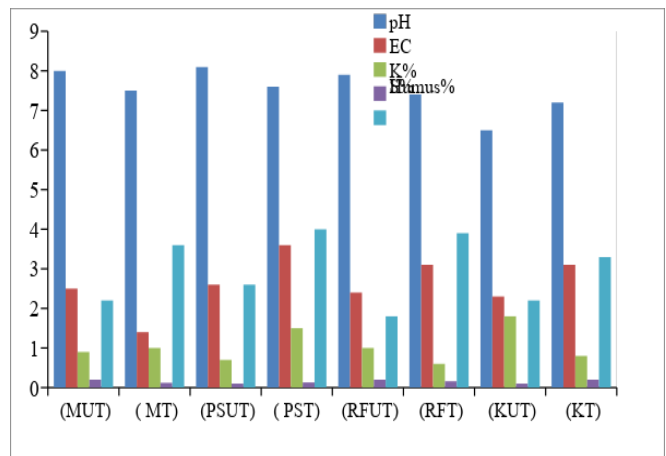


Fig.3 Changes in the physiological properties during the degradation of various waste

MUT: Maize Untreated; MT: Maize treated; PSUT: Paddy Straw Untreated; PST: Paddy Straw Treated; KUT: Kinnow Untreated; KT: Kinnow Treated; RFUT: Flower Untreated; RFT: Flower Treated

The results clearly showed variation in most of the parameters with substrates used for composting. The pH range was 6.5-8.0 in all the

substrates but in inoculated substrates the range of pH was 7.2-7.6 while EC was 1.4-3.6 and the humus content also varied with substrates. The highest humus% was found in paddy straw followed by maize, flower and kinnow. The final product also showed variation in K% and S% which were found to be 0.6% -1.8% and 0.1% - 0.20%, respectively. Seed germination test was performed with water cress seeds (*Lepidium sativum*) and it was observed that all the substrates where fungal inoculation was carried out showed 100% seed germination while the uninoculated substrates showed 50% - 60% seed germination clearly indicating that the compost had not matured.

Overall results on spore count of *Aspergillus awamori*, *Trichoderma viride*, *Trichoderma longibrachiatum*, *Dechslera halodes*, *Eupenicillium crustaceum* and *Paecilomyces variotii* showed that glycerol was the most suitable additive for incubation and longer shelf-life of fungal spores. The fungal strains *Trichoderma viride*, *Trichoderma longibrachitum*, *Dechslera halodes*, *Eupenicillium crustaceum* and *Paecilomyces variotii* were found effective in degradation of ligno-cellulolytic material and hence can be used for degradation of different agro-wastes.

Funding Sources: No funding received for this work.

Acknowledgements: We are thankful to Head, Division of plant pathology, Indian Agriculture Research Institute for their encouragement and support throughout the research and we also gratefully acknowledged the Indian Council of Agricultural Research for providing necessary facilities and financial support.

Compliance with ethical standards: The authors declare that they have no conflict of interest. This article does not contain any studies involving animals or human participants performed by any of the authors.

References:

1. S.K. Lohan, H.S. Jat, A.K. Yadav, H.S. Sidhu, M.L. Jat, M. Choudhary, P.C. Sharma, Burning issues of Paddy residue management in north-west states of India. *Renewable and Sustainable Energy Reviews* (2018) 81:693–706. <https://doi.org/10.1016/j.rser.2017.08.057>
2. A.A. Abd El-Rahman, O.V. Kozlova, S.M.A. El-Shafei, F.K. Alimova, F.G. Kupriyanova-Ashina, Changes in growth patterns and intracellular calcium concentrations in *Aspergillus awamori* treated with amphotericin B. *Microbiology*, 83:344–351, 2014. <https://doi.org/10.1134/S002626171404002X>.
3. Anonymous, National Policy of Crop Residues (NPMCR), Ministry of Agriculture, Department of Agriculture & Cooperation (Natural Resource Management Division), Krishi Bhawan, New Delhi:GOI 2014.
4. Greenpeace, Energy (r) Evolution- A Sustainable EU 27 Energy Outlook. <https://www.greenpeace.org/archive-eu-nit/en/Publications/2012/ER-2012>, 2019.
5. B. Sharma, B. Vaish, U.K. Singh, P. Singh, R.P. Singh Recycling of organic wastes in agriculture. *International Journal of Environmental Research* ,13, 2019, 409–429. <https://doi.org/10.1007/s41742-019-00175-y>
6. J. Pang, Z.Y. Liu, M. Hao, Y.F. Zhang, Q.S. Qi, An isolated cellulolytic *Escherichia coli* from bovine rumen produces ethanol and hydrogen from corn straw. *Biotechnology for Biofuels* 10, 2017, 165. <https://doi.org/10.1186/s13068-017-0852-7>.
7. Y. Xue, J. Han, Y. Li, J. Liu, L. Gan, M. Long, Promoting cellulase and hemicellulose production from *Trichoderma orientalis* EU7-22 by overexpression of transcription factors Xyl1 and Ace3. *Bioresource Technology*, 296, 2020, 122355. <https://doi.org/10.1016/j.biortech.2019.122355>
8. Y. Wei, D. Wu, D. Wei, Y. Zhao, J. Wu, X. Xie, Z. Wei, Improved lignocellulose-degrading performance during straw composting from diverse sources with

- actinomycetes inoculation by regulating the key enzyme activities. *Bioresource Technology*, 271, 2019, 66-74. <https://doi.org/10.1016/j.biortech.2018.09.081>
9. Y. Chen, W. Wang, D. Zhou, T. Jing, K. Li, Y. Zhao, Y. Luo, Biodegradation of lignocellulosic agricultural residues by a newly isolated *Fictibacillus* sp. YS-26 improving carbon metabolic properties and functional diversity of the rhizosphere microbial community. *Bioresource Technology* 310, 2020, 123381. <https://doi.org/10.1016/j.biortech.2020.123381>.
10. S. Gopalakrishnan, A. Sathya, R. Vijayabharathi, V. Srinivas, Formulations of Plant Growth-Promoting Microbes for Field Applications. *Microbial Inoculants in Sustainable Agricultural Productivity*. Springer, New Delhi, 2016, 239–251. https://doi.org/10.1007/978-81-322-2644-4_15
11. L. Shukla, A. Senapati, S.P. Tyagi, A.K. Saxena, Economically viable mass production of lignocellulolytic fungal inoculum for rapid degradation of agro waste. *Current Science*, 107, 2014, 1701–1704.
12. O.C. Devêvre, W.R. Horwáth, Decomposition of rice straw and microbial carbon use efficiency under different soil temperatures and moistures. *Soil Biology & Biochemistry*, 32, 2000, 1773–1785. [https://doi.org/10.1016/S0038-0717\(00\)00096-1](https://doi.org/10.1016/S0038-0717(00)00096-1).
13. L.H.S. Guimarães, S.C. Peixoto-Nogueira, M. Michelin, A.C.S. Rizzatti, V.C. Sandrim, F.F. Zanoelo, A.C.M.M. Aquino, A. Barbosa junior, M.D.L. Polizeli, Screening of filamentous fungi with potential of production of enzyme with biotechnological applications. *Brazilian Journal of Microbiology*, 474–480, 2006. <https://doi.org/10.1590/S1517-83822006000400014>.
14. V. Jegathambigai, R.S. Wijeratnam, R.L.C. Wijesundera, (2010) Effect of *Trichoderma* sp. On *Sclerotium rolfsii*, the causative agent of collar rot on *Zamioculcas zamiifolia* and an on-farm method to mass produce *Trichoderma* species. *Plant Pathology J9*: 47–55. DOI: 10.3923/ppj.2010.47.55.
15. S.S. Sakthi, P. Saranraj, M. Rajasekar Optimization for cellulose production by *Aspergillus niger* using paddy straw as substrate. *International Journal of Advanced Science and Technology*, 1, 2011, 68–85.
16. S. Sriram, K.B. Palanna, B. Ramanujam, Effect of chitin on the shelf-life of *Trichoderma harzianum* in talc formulation. *Indian Journal of Agricultural Sciences*, 80, 2010, 930-932.
17. L. Shukla, S.D. Lande, R.A. Parray, A. Suman, K. Annapurna, I. Mani, Vikram, Recycling flower waste to humus rich compost using effective microbial consortium and mechanical intervention. *Indian Journal of Agricultural Sciences*, 89, 2019, 140–146. <https://doi.org/10.56093/ijas.v89i7.91698>.
18. Sahu, M.C. Manna, S. Bhattacharjya, J.K. Thakur, A. Mandal, M.M. Rahman, S.K. Chaudhari, Thermophilic ligno-cellulolytic fungi: The future of efficient and rapid bio-waste management. *Journal of Environmental Management* 244, 2019, 144–153. <https://doi.org/10.1016/j.jenvman.2019.04.015>
19. Shukla L, Senapati A, Tyagi S P and Saxena A. 2014. Economically viable mass production of lignocellulolytic fungal inoculum for rapid degradation of agro waste, *Current Science*, 107, 2014, 1701–1704.

Production of Green energy via Water Splitting mechanism by Mn-doped cobalt ferrites [Co_{1-x}Mn_xFe₂O₄] based hydroelectric cells

Prachi Jain^{a, b}, S. Shankar^a, O. P. Thakur^{a*}

^a Materials Analysis and Research Laboratory, Department of Physics, Netaji Subhas University of Technology, New Delhi 110078, India

^b Functional Materials Research Laboratory, Department of Physics, ARSD College, University of Delhi-110021, India.

Volume 1, Issue 2, March 2024

Received: 11 January, 2024; Accepted: 14 February, 2024

DOI: <https://doi.org/10.63015/2h-2419.1.2>

*Corresponding author email: ophaku@nsut.ac.in

Abstract: In our current study, we have investigated the impact of manganese (Mn) doping on the structural, magnetic properties, and hydroelectric cell properties of cobalt ferrite with chemical formula [Co_{1-x}Mn_xFe₂O₄, x=0.00, 0.125]. The solid-state approach has been utilized to synthesize the material. XRD measurements revealed the formation of an inverse spinel cubic structure with the space group Fd-3m. FTIR spectra hold a shift in the octahedral and tetrahedral bands with the increase in Mn content in cobalt ferrites. The subsequent rise in ferroelectric behavior has been observed with the net maximum saturation polarization of 1.08 μC/cm². The variation in the permittivity values has been also studied with the increase in Mn content for dry as well as wet hydroelectric cells. The impedance measurements helped us understand the contribution of grains/grain boundaries in the prepared ferrites. The enhanced value of magnetization has been noticed from 48.258 emu/g to 73.089 emu/g upon doping of Mn ions in cobalt ferrite spinel structure lattice. The Mn doped CFO exhibited enhanced performance in hydroelectric cells which demonstrates the great ionic diffusion mechanism with the incorporation of Mn ions. The obtained output makes Mn doped CFO a suitable material for studying microelectronic and hydroelectric cell applications. The purpose of this study is to enhance both ferroelectric as well as ferromagnetic behavior along with the improved value of current in hydroelectric cells.

Keywords: Ferroelectrics, Multiferroics, Hydroelectric cells, Ferromagnetism, Dielectrics.

1. Introduction: Energy storage has now become a big concern in the society because the consumption of energy is increasing day by day. The evolution of toxic gases by the energy released from fossil fuels is degrading the environment. So, there is a high urge to develop those devices that can generate clean and green energy. The generation of green energy by the hydroelectric cells using a few water droplets has been proven to be a cheap, clean, and eco-friendly technique [1]. Water dissociation has been obtained at room temperature by oxygen-deficient materials without the usage of any electrolytes/ acids/ alkalis, etc [2]. Hydroelectric cells have been already tailored using various metal oxides like TiO₂, SnO₂, MgO, ZnO-CuO, Fe₂O₃, and Al₂O₃ [3-8]. It has been rigorously studied that doping of

external elements in ferrite or oxides generates oxygen vacancies in the lattice. Doping of Mg in Al₂O₃ has decreased the internal resistance of oxide and produced the maximum power density of 3.37 mW/cm² [9]. A big amount of industrial waste called red mud has been fabricated into a clean and green source of energy (hydroelectric cells) [10].

CoFe₂O₄ is an interesting magnetoelectric multiferroic material having a transition temperature (T_C) of ~580K. Its transition temperature can be tuned below or above the room temperature by changing the Fe content in Fe_{2-x}Mn_xO₄ (at x =0.125 T_C was 900K) and processing conditions [11]. In contemporary understanding, magnetic materials are classified into various categories, including paramagnetic, diamagnetic, ferromagnetic,

ferrimagnetic, antiferromagnetic, superparamagnetic, and spin glass. Cobalt ferrite nanoparticles have an inverse spinel structure. Co^{2+} and Fe^{3+} occupy either tetrahedral or octahedral interstitial spaces in this O^{2-} form FCC tight packing. Half of the Fe^{3+} ion and Co^{2+} ions are found in the octahedral sites of this inverse spinel cobalt ferrite structure, while the remaining Fe^{3+} ions are found in the tetrahedral sites. Cobalt ferrite features closed-packed spinel arrangements with 32 oxygen ions from unit cells and a secondary phase cubic spinel crystal structure with space group symmetry Fd-3m . The unit cell of the CFO contains a total of 56 atoms. There are 64 tetrahedral sites and 32 octahedral sites in the unit cell containing 32 oxygen ions [12].

It has been observed that Mn doped CFO has decreased the resistance of pure CFO, thereby initiating the fast movement of ions contributing towards improved current [13]. Many findings have been already reported on the storage efficiency of Mn doped CFO. Singh et al. reported the manganese doped ferrite and PANI composite for energy storage electrode material for supercapacitor applications [14]. Milan et al. found increased transport and magnetic properties of CFO upon doping with manganese ion [15]. Fiaz et al. showed the anticancer, antibacterial, and antidiabetic applications of Mn doped CFO [16].

Amongst all available ferrites, the research on manganese (Mn) doped cobalt ferrites (CFO) based hydroelectric cells (HEC) has not been reported yet. Here, we will report the maximum current and voltage produced in Mn doped CFO based HEC.

2. Methodology: The solid-state synthesis route has been followed to prepare the highly porous Mn doped CFO with the chemical composition $[\text{CoFe}_2\text{O}_4, \text{CoMn}_{0.125}\text{Fe}_{1.875}\text{O}_4]$ has been shown in Fig 1. The stoichiometric amount of $(\text{Co}_3\text{O}_4, \text{Loba Chemie})$ and $(\text{Fe}_2\text{O}_3, \text{Fisher Scientific})$ were taken and grounded together in an agar pestle mortar in the acetic medium for 3-4 h constantly. Then, the obtained powder was calcined at 900°C for

3 h. Obtained calcined powder was further sintered at 50°C above the calcined temperature for 4 h. Then, the powder was again grounded for 1 h to obtain fine particles.



hydroelectric cells.

Preparation of Hydroelectric cells (HEC):

The obtained sample powder was mixed with PVA binder and then transformed into square pellets of dimensions $2\text{ cm} \times 2\text{ cm}$ and thickness of 2mm using a hydraulic presser machine as shown in Fig 2. The square pellets were then hardened by sintering at 250°C for 2 h to evaporate the PVA binder and to obtain homogeneity in the samples. Silver paint lines were drawn in a comb pattern on one face of all the pellets. A zinc sheet was pasted on the other side of each of the pellets. Finally, electrical contacts were applied to all the pellets to develop them in the form of fully functional HECs.

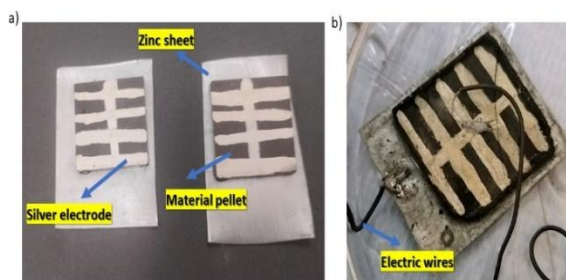


Fig 2. Representation of (a) CFO and (b) Mn-CFO based hydroelectric cells.

3. Characterization Techniques: The XRD measurements of Mn doped CFO were carried out using Bruker D8 Advance X-Ray diffractometer with $\text{Cu-K}\alpha$ radiations ($\lambda = 1.5406\text{\AA}$) in 2θ range extending from 10° to

90° with a scanning speed of 1°/min. The FTIR spectra were obtained using Perkin Elmer for measurements in the range of 4100-400 cm⁻¹ for solid samples. The surface morphology of the samples was done using the FESEM-EDX Zeiss instrument. Dielectric, Conductivity, and Impedance measurements of all samples were carried out by using a Nova Control Technology Impedance analyzer. The magnetic studies (M-H loop) were recorded using an ADE-EV9 VSM (vibrating sample magnetometer) instrument under a magnetic field of 1 Tesla obtained at room temperature. The V-I measurements of the HEC have been performed using a Keithley 2450 source meter.

4. Results and Discussion

4.1. Morphological analysis: Fig 3. represents the XRD pattern of pure cobalt ferrite (CFO) and manganese doped cobalt

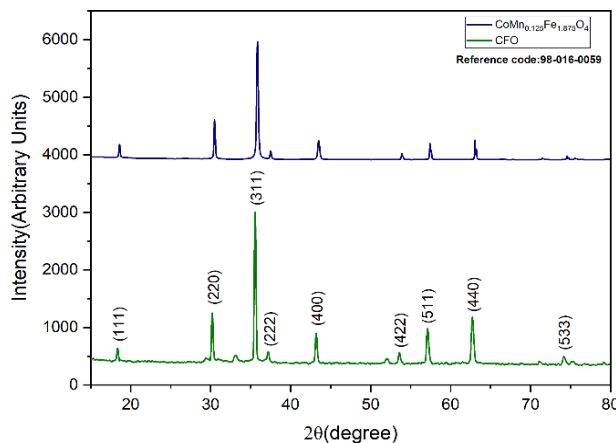


Fig 3. X-ray diffraction data of CFO and CoMn_{0.125}Fe_{1.875}O₄ recorded within the 2θ region of 10°-80°; fitted with Fd-3m space group cubic crystal structure.

ferrites (Mn CFO) recorded using a Panalytical X' Pert Pro MRD diffractometer using Cu K_α radiation (λ= 1.5406Å) obtained at room temperature. The major peaks have been listed as (111), (220), (311), (220), (400), (422), (511), (440), and (533) which are

characteristics of a cubic spinel structure with Fd-3m space group. The obtained diffraction peaks are well matched with the standard JCPDS card number: **98-016-0059** for CoMn_xFe_{2-x}O₄. [17].

Table 1 lists the structural parameters that were determined from the XRD pattern, including crystallite size, lattice parameter, interplanar spacing, X-ray density, bulk density, and porosity (%). The formulae for the calculation of these parameters are

$$\text{Lattice parameter} = d\sqrt{h^2 + k^2 + l^2} \quad (1)$$

$$\text{X-ray density (D}_x\text{)} = \frac{8M}{Na^3} \quad (2)$$

$$\text{Bulk density (D}_b\text{)} = \text{Mass of pellet/ Volume of pellet} = m/\Pi r^2 L \quad (3)$$

$$\text{Porosity (\%)} = 1 - D_b/D_x \quad (4)$$

Using the W-H plot equation, the average crystallite size (D) and induced microstrain have been calculated as given by equation (5)

$$\beta \text{Cos}\theta = (4 \text{Sin}\theta)\epsilon + \frac{K\lambda}{D}, \quad (5)$$

where β represents full width at half maximum (FWHM), θ is the angle of strongest intensity peak, ε is the micro-strain, and λ is the wavelength of Cu-Kα (1.54Å) radiation used respectively. The average crystallite size for the prepared MnCFO nanoparticles has been found around 55.69 nm.

It has been observed from Table 1, that the porosity % has increased from 56.75 % to 61.8% with the incorporation of Mn ions in CFO. The doping of foreign dopant atom (Mn) in the pure CFO leads to the formation of defects resulting in a large value of microstrain [18]. The substitution of dopant ions also creates dislocation in the lattice thereby contributing towards the defects. These defects consist of oxygen vacancies which are

Table 1. Useful Parameters calculated from the XRD plots of Manganese doped cobalt ferrites (MnCFO)

Sample	Crystallite size (nm)	Strain (× 10 ⁻³)	Lattice parameter (Å)	Volume (Å ³)	Interplanar spacing (Å)	Bulk density (g/cm ³)	X-ray density (g/cm ³)	Porosity (%)
CoFe ₂ O ₄	51.16	2.13	8.383	589.112	2.527	2.99	4.506	33.644
CoFe _{2-x} Mn _x O ₄	55.69	0.76	8.385	589.534	2.528	2.91	4.458	34.724

mainly responsible for the interaction of water molecules with the lattice.

4.2. FTIR spectroscopy:

Fourier transform infrared (FTIR) spectroscopy was used to examine the structure and cation distribution between the tetrahedral and octahedral lattice sites in the inverse spinel ferrite, All spinel structures

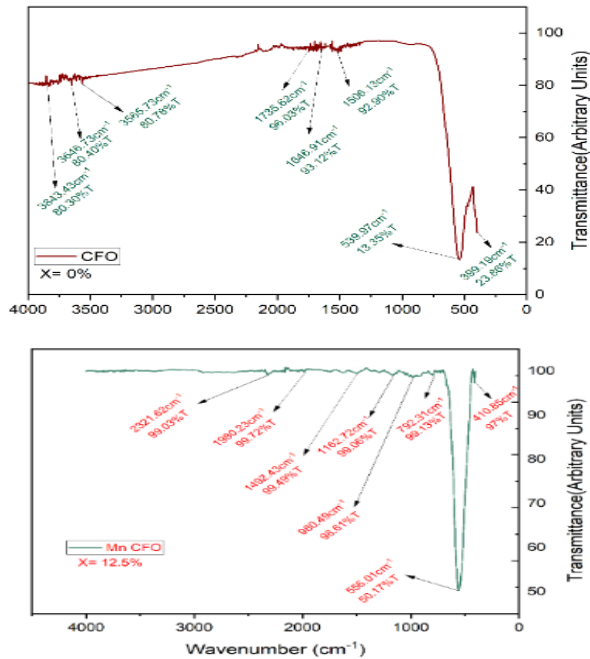


Fig 4. FTIR spectra of (a) CFO (b) Mn-CFO based ferrites.

contain two primary metal-oxygen bands that can be seen in the IR spectrum. Fig 4. shows the FTIR spectrum of pure as well as Mn-doped cobalt ferrite. The band ν_1 for pure and Mn-doped at (539.97 cm^{-1} & 556.01 cm^{-1}) arises in the range of $500\text{-}600\text{ cm}^{-1}$ due to tetrahedral complexes and ν_2 at 399 cm^{-1} & 410.85 cm^{-1} is due to octahedral complexes [19]. In cobalt ferrite and cobalt ferrite doped with Mn, the O-H bands may be shown to be

stretched at a distance of 1506.13 cm^{-1} and bent at a distance of 3843.43 cm^{-1} , respectively. Small particle sizes can cause line broadening and vibrational mode overlap, making it challenging to observe certain bands. The characteristic band ν_1 of spinel ferrites changes to a higher frequency region as the Mn-substitution grows. This is because manganese has a lighter atomic mass than cobalt. Consequently, the frequency of metal-oxygen stretching will rise [20].

4.3. Morphological Studies:

SEM-EDX micrographs of the sintered pellets

Table 2. Atomic and weight % obtained for manganese doped cobalt ferrites (Mn-CFO).

of CoFe_2O_4 , $\text{CoMn}_{0.125}\text{Fe}_{1.875}\text{O}_4$ have been recorded at room temperature and are shown in Fig 5. The surface morphology is observed

Elements	Weight %	Atomic %
O K	21.97	50.07
Mn K	0.65	0.43
Fe K	47.42	30.96
Co K	29.96	18.53

to be quite uniform in both samples. Energy Dispersive X-ray (EDX) micro-analysis is a technique used to determine the elemental composition of a sample. The average grain size of the Mn doped spinel ferrite nanoparticles has been calculated using ImageJ software and found to be near around 69 nm. It provides qualitative information about the presence of different elements like Mn, Co, O, and Fe in the samples and allows for quantitative analysis by determining the

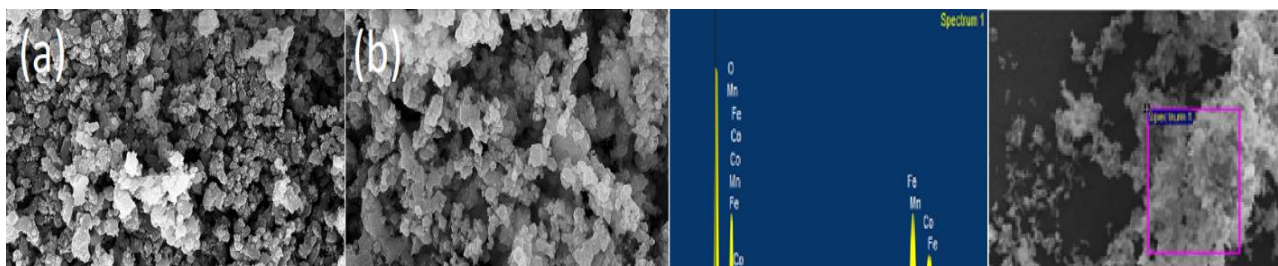


Fig 5. SEM micrograph and compositional study of (a) CoFe_2O_4 (b) $\text{CoMn}_{0.125}\text{Fe}_{1.875}\text{O}_4$, sample at 50 k magnification and 20 kV power.

relative abundance or concentration of elements in the sample [21].

4.4. Comparison of Ferroelectricity: Fig 6. exhibits the variation of polarization against the electric field ($E=10$ KV/cm) for pure as well as Mn doped cobalt ferrites obtained at

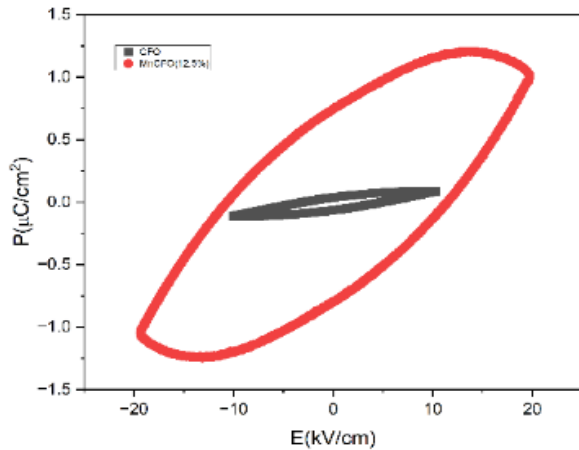


Fig 6. Variation of Polarization (a) CoFe_2O_4 (b) $\text{CoMn}_{0.125}\text{Fe}_{1.875}\text{O}_4$, sample with electric field obtained at RT.

room temperature and the applied frequency at 50 Hz. The material appears to be lossy and polycrystalline based on hysteresis loops [22]. It has been observed that the net saturation polarization has been increased to $1.08\mu\text{C}/\text{cm}^2$ with very small doping of Mn in CFO. The value of net remnant polarization has been also increased upon the addition of Mn in CFO.

4.5. Ferromagnetic Studies: Field-dependent magnetic properties of Mn doped CFO has been shown in Fig 7. as obtained at room temperature. It has been observed that the addition of Mn in CFO caused a vigorous rise in the values of saturation magnetization (M_s) from 48.258 emu/g to 73.089 emu/g. Table 3. exhibits the decrease in coercivity and the subsequent rise in the magnetic properties that occurred for Mn doped CFO. The exclusive rise in the value of M_s is mainly due to the difference in the magnetic moments of the ions present at the A-site and the ions at the B-site. The doping of Mn^{2+} ion caused the replacement of B-site ions and thus altered the magnetic moment of ions present at B-site. Hence, due to the change in the magnetic moment, the net value of (M_s) got intensively

increased [23]. The hysteresis loop has occurred at RT showing that material is ferrimagnetic. The magnetic characteristics of

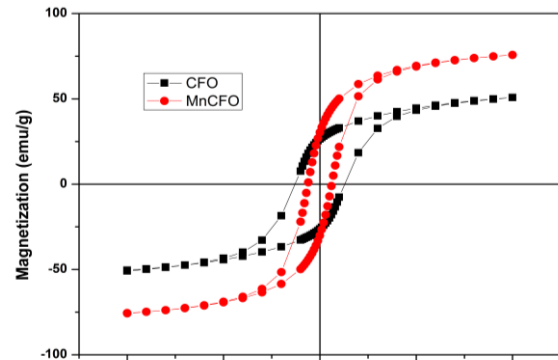


Fig 7. M-H loop of cobalt ferrite & manganese doped (a) CoFe_2O_4 (b) $\text{CoMn}_{0.125}\text{Fe}_{1.875}\text{O}_4$, sample cobalt ferrite nanoparticles.

cobalt ferrite nanoparticles are affected by the particle size, production process, and cation dispersion. These elements produce surface disorder brought on by a canted spin structure and random cation distribution. The high surface disorder generally occurs due to the presence of high surface anisotropy [24]. CFO based compounds have been heavily researched because of its strong coercivity, great chemical stability, superior electrical insulation, significant mechanical hardness, and mild saturation magnetization at ambient temperature, etc [25].

Table 3. Values of M_s , M_r , and H_c for manganese doped cobalt ferrites (Mn-CFO)

Chemical compound	M_s (emu/g)	M_r (emu/g)	H_c (Oe)
CFO	48.258	26.502	1266.45
Mn-CFO	73.089	30.490	644.975

4.6. Variation of dielectric constant (ϵ') for dry and wet hydroelectric cells:The ability of water dissociation by the Mn doped CFO based HEC and the conduction mechanism has been investigated using an impedance analyzer at room temperature. The variation of dielectric constant against frequency in the frequency range 20 Hz- 10^6

Hz is shown in Fig 8. It has been observed that the dielectric constant (ϵ') values has been

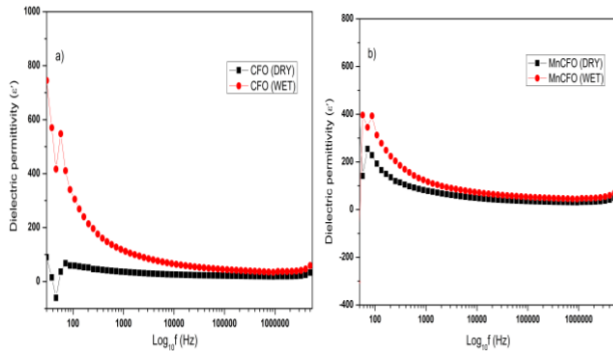


Fig 8. Dielectric constant with frequency for dry and wet hydroelectric cells of (a) CoFe_2O_4 (b) $\text{CoMn}_{0.125}\text{Fe}_{1.875}\text{O}_4$.

increased for wet HEC as compared to dry HEC at low frequency range. The ϵ' values have become almost constant at high frequency range. This behaviour in the variation of ϵ' values is mainly due to rise in ionic and space charge polarization due to dissociated water molecules [26].

4.7. Ionic diffusion Plots: EIS is a highly delicate technique to study the diffusion of ions on the material's surface. The various reactions occurring on the cell surface can be

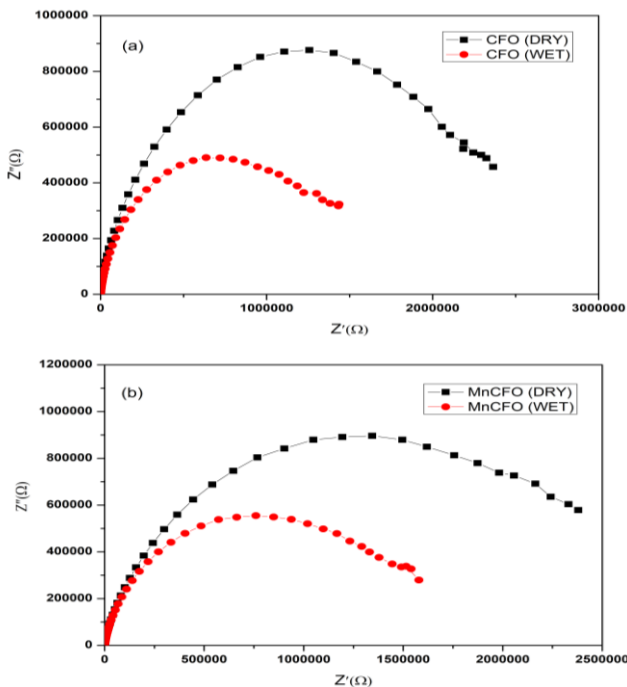


Fig 9. Z'' vs Z' plots for dry and wet hydroelectric cells of (a) CoFe_2O_4 (b) $\text{CoMn}_{0.125}\text{Fe}_{1.875}\text{O}_4$.

studied using EIS spectroscopy. The Nyquist's plots have shown the large impedance of dry

HEC in the order of 107- 108 ohms as compared to wet HEC. Wet HEC exhibit impedance in the range of few kilo ohms. This extreme deduction in the impedance value is due to the dissociation of water molecules into H_3O^+ and OH^- ions. It confirms the water molecules had been adsorbed on the sample surface and got chemidissociated [27].

4.8. Current and voltage studies in Mn doped CFO based hydroelectric cells:

The variation of voltage against current for pure cobalt ferrite as well as Mn doped CFO is

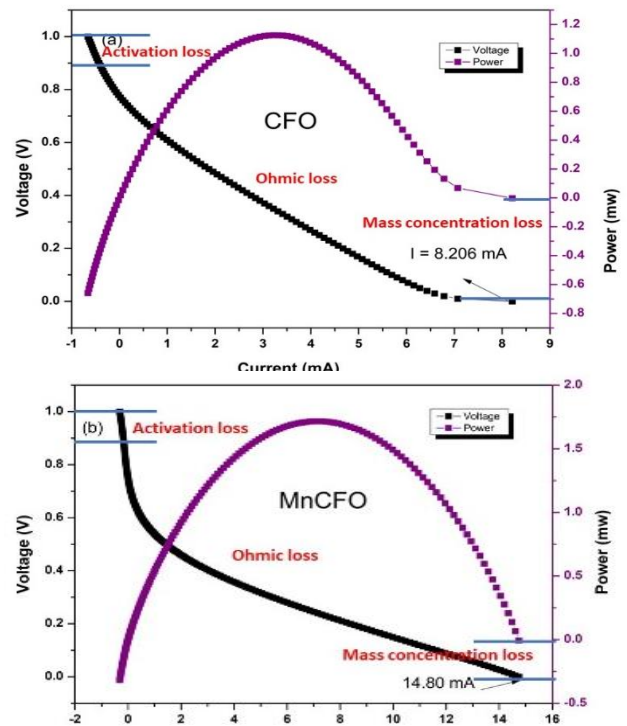


Fig 10. V-I polarization plots for dry and wet HEC of (a) CoFe_2O_4 (b) $\text{CoMn}_{0.125}\text{Fe}_{1.875}\text{O}_4$.

shown in Fig 10. The maximum peak off-load current (I_{sc}) around 14.80 mA has been reported for Mn doped CFO based HEC. The high value of current (~ 14.80 mA) has been accommodated due to the production of more oxygen vacancies in Mn doped CFO. It has been observed that the concentration loss gets reduced for doped cells due to which current remains constant for a longer time and gives high value. The whole V-I polarization curve is divided into mainly three regions:- Activation loss, ohmic loss and mass concentration loss. Activation loss refers to the energy barrier for the charge transfer reaction

at both electrodes. Ohmic region is the region where voltage decreases in almost linear manner with the current. The sharp degradation in the voltage has been occurred due to the aggregation of ions near the electrodes and caused a concentration loss or mass loss [28,29].

5. Conclusions: A comprehensive investigation was conducted to check the impact of Mn substitution on the generation of current by hydroelectric cells of cobalt ferrites. The presence of Mn^{2+} ions in the lattice has led to the generation of strain and oxygen vacancies. X-ray diffraction pattern and Fourier transform spectroscopy has confirmed the formation of cubic phase of $Co_{1-x}Mn_xFe_2O_4$ (where $x = 0.00, 0.125$) ferrites. XRD studies revealed the net increment in the porosity % for the Mn doped CFO. Increased porosity initiated increased chemi-dissociation of water molecules. High values of saturation magnetization obtained at room temperature suggests the ferromagnetic nature of the material. The fitted Nyquist plot of Mn doped CFO based HEC shows a drop in both charge transfer resistance and ohmic resistance. This drop, in turn, enhanced the reaction rate and a corresponding enhancement has been observed in ionic conduction. This enhanced ionic conduction produces an output current of 14.80 mA, accompanied by voltage of 0.98 V, for the substitution of Mn in CFO. This study demonstrates the improved performance of hydroelectric cells based on transition metal doped ferrites.

References:

- Gaur, A., Shah, J., Kotnala, R. K., & Kumar, D. (2022). Development of Mg-doped hematite (α -Fe₂O₃)-based hydroelectric cell to generate green electricity. *New Journal of Chemistry*, 46(44), 21158-21166.
- Manash, A., Singh, R. K., Kumar, V., Shah, J., Das, S. B., Kumar, S. S., ... & Kotnala, R. K. (2023). Studies on structural and magnetic properties of nanoporous Li⁺ substituted MgFe₂O₄ nanomaterials for its application in hydroelectric cell with other areas of science & technology. *Materials Today: Proceedings*, 80, 1002-1013.
- Bhakar, U., Agarwal, A., Sanghi, S., Shah, J., & Kotnala, R. K. (2021). Production of green electricity from strained BaTiO₃ and TiO₂ ceramics based hydroelectric cells. *Materials Chemistry and Physics*, 262, 124277.
- Kumar, P., Vashishth, S., Sharma, I., & Verma, V. (2021). Porous SnO₂ ceramic-based hydroelectric cells for green power generation. *Journal of Materials Science: Materials in Electronics*, 32, 1052-1060.
- Kotnala, R. K., Gupta, R., Shukla, A., Jain, S., Gaur, A., & Shah, J. (2018). Metal oxide based hydroelectric cell for electricity generation by water molecule dissociation without electrolyte/acid. *The Journal of Physical Chemistry C*, 122(33), 18841-18849.
- Maurya, I., Gupta, T., Shankar, S., Gaurav, S., Tuli, V., Shah, J., & Kotnala, R. K. (2022). Dielectric and impedance studies of binary ZnO–CuO nanocomposites for hydroelectric cell application. *Materials Chemistry and Physics*, 291, 126690.
- Jain, S., Shah, J., Dhakate, S. R., Gupta, G., Sharma, C., & Kotnala, R. K. (2018). Environment-friendly mesoporous magnetite nanoparticles-based hydroelectric cell. *The Journal of Physical Chemistry C*, 122(11), 5908-5916.
- Das, R., Shah, J., Sharma, S., Sharma, P. B., & Kotnala, R. K. (2020). Electricity generation by splitting of water from hydroelectric cell: An alternative to solar cell and fuel cell. *International Journal of Energy Research*, 44(14), 11111-11134.
- Gupta, R., Shah, J., Das, R., Saini, S., & Kotnala, R. K. (2021). Defect-mediated ionic hopping and green electricity generation in Al_{2-x}Mg_xO₃-based hydroelectric cell. *Journal of Materials Science*, 56, 1600-1611.
- Kotnala, R. K., Das, R., Shah, J., Sharma, S., Sharma, C., & Sharma, P. B. (2022). Red mud industrial waste translated into green electricity production by innovating an ingenious process based on

- Hydroelectric Cell. *Journal of Environmental Engineering*, 10(2), 107299.
11. Yadav, R. S., Kuřitka, I., Vilcakova, J., Havlica, J., Masilko, J., Kalina, L., ... & Hajdúchová, M. (2017). Impact of grain size and structural changes on magnetic, dielectric, electrical, impedance and modulus spectroscopic characteristics of CoFe₂O₄ nanoparticles synthesized by honey mediated sol-gel combustion method. *Advances in Natural Sciences: Nanoscience and Nanotechnology*, 8(4), 045002.
 12. Thakur, P., Gahlawat, N., Punia, P., Kharbanda, S., Ravelo, B., & Thakur, A. (2022). Cobalt nanoferrites: A review on synthesis, characterization, and applications. *Journal of Superconductivity and Novel Magnetism*, 35(10), 2639-2669.
 13. Kolekar, Y. D., Sanchez, L. J., & Ramana, C. V. (2014). Dielectric relaxations and alternating current conductivity in manganese substituted cobalt ferrite. *Journal of Applied Physics*, 115(14).
 14. Singh, G., & Chandra, S. (2020). Nano-flowered manganese doped ferrite@ PANI composite as energy storage electrode material for supercapacitors. *Journal of Electroanalytical Chemistry*, 874, 114491.
 15. Singh, M., Dubey, B. P., Sahoo, A., Yadav, K. L., & Sharma, Y. (2021). Tailoring the transport and magnetic properties of Mn doped spinel FeCo₂O₄ and their impact on energy storage properties: A new strategy to improve storage performance. *Journal of Energy Storage*, 44, 103361.
 16. Fiaz, S., Ahmed, M. N., ul Haq, I., Shah, S. W. A., & Waseem, M. (2023). Green synthesis of cobalt ferrite and Mn doped cobalt ferrite nanoparticles: Anticancer, antidiabetic and antibacterial studies. *Journal of Trace Elements in Medicine and Biology*, 80, 127292.
 17. Zawrah, M. F., El-Okr, M. M., Ashery, A., & Abou Hammad, A. B. (2016). Characterization of sol-gel fabricated cobalt ferrite CoFe₂O₄ nanoparticles. *Middle East Journal of Applied Sciences*, 6, 362-366.
 18. Jain, P., Shankar, S., & Thakur, O. P. (2023). Unveiling the impact of Ni²⁺/Y³⁺ co-substitution on the structural, dielectric, and impedance properties of multiferroic spinel ferrite for hydroelectric cell application. *Physical Chemistry Chemical Physics*, 25(32), 21280-21296.
 19. Karthickraja, D., Karthi, S., Kumar, G. A., Sardar, D. K., Dannangoda, G. C., Martirosyan, K. S., & Girija, E. K. (2019). Fabrication of core-shell CoFe₂O₄@HAp nanoparticles: a novel magnetic platform for biomedical applications. *New Journal of Chemistry*, 43(34), 13584-13593.
 20. Abdel Maksoud, M. I. A., El-Sayyad, G. S., Abd Elkodous, M., & Awed, A. S. (2020). Controllable synthesis of Co_{1-x}M_xFe₂O₄ nanoparticles (M= Zn, Cu, and Mn; x= 0.0 and 0.5) by cost-effective sol-gel approach: analysis of structure, elastic, thermal, and magnetic properties. *Journal of Materials Science: Materials in Electronics*, 31(12), 9726-9741.
 21. Ashour, A. H., El-Batal, A. I., Maksoud, M. A., El-Sayyad, G. S., Labib, S., Abdeltwab, E., & El-Okr, M. M. (2018). Antimicrobial activity of metal-substituted cobalt ferrite nanoparticles synthesized by sol-gel technique. *Particuology*, 40, 141-151.
 22. Shankar, S., Kumar, M., Ghosh, A. K., Thakur, O. P., & Jayasimhadri, M. (2019). Anomalous ferroelectricity and strong magnetoelectric coupling in CoFe₂O₄-ferroelectric composites. *Journal of Alloys and Compounds*, 779, 918-925.
 23. Yadav, S. P., Shinde, S. S., Kadam, A. A., & Rajpure, K. Y. (2013). Structural, morphological, dielectrical and magnetic properties of Mn substituted cobalt ferrite. *Journal of Semiconductors*, 34(9), 093002.
 24. Swatsitang, E., Phokha, S., Hunpratub, S., Usher, B., Bootchanont, A., Maensiri, S., & Chindaprasirt, P. (2016). Characterization and magnetic properties of cobalt ferrite nanoparticles. *Journal of Alloys and Compounds*, 664, 792-797.

25. Rana, K., Thakur, P., Sharma, P., Tomar, M., Gupta, V., & Thakur, A. (2015). Improved structural and magnetic properties of cobalt nanoferrites: influence of sintering temperature. *Ceramics International*, 41(3), 4492-4497.
26. Jain, P., Shankar, S., & Thakur, O. P. (2022). Dielectric, impedance spectroscopy and hydroelectric phenomena in lanthanum doped bismuth ferrite (Bi_{0.85}La_{0.15}FeO₃). *Materials Today: Proceedings*, 67, 742-747.
27. Badola, S., Shah, J., Gaur, A., Khasa, S., Rawal, D. S., Mandal, T. K., ... & Kotnala, R. K. (2023). Strategic enhancement of oxygen defects in ZnO from ZnS for water splitting to generate green electricity by hydroelectric cell. *Applied Materials Today*, 34, 101904.
28. Gaur, A., Kumar, A., Kumar, P., Agrawal, R., Shah, J., & Kotnala, R. K. (2020). Fabrication of a SnO₂-based hydroelectric cell for green energy production. *ACS omega*, 5(18), 10240-10246.
29. Parray, I. A., Somvanshi, A., & Ali, S. A. (2023). Study of microstructural, ferroelectric and magnetic properties of cerium substituted magnesium ferrite and its potential application as hydroelectric cell. *Ceramics International*, 49(4), 6946-6957.

Induced Magnetization in Antiferromagnetic GdFeO₃ by Nonmagnetic Titanium Substitution for Magnetic Switching and Storage Application

Jyoti shah* and R K Kotnala

CSIR-National Physical Laboratory, Delhi-110012, India

Volume 1, Issue 2, March 2024

Received: 11 January, 2024; Accepted: 14 February, 2024

DOI: <https://doi.org/10.63015/10s-2410.1.2>

*Corresponding author email: shah.jyoti1@gmail.com

Abstract: Room temperature ferromagnetism has been induced in antiferromagnetic GdFeO₃ by substituting titanium at Gd site Gd_{1-x}Ti_xFeO₃ (x=0.00 - 0.25). Perovskite GdFeO₃ has been synthesized at lower temperature by chemical co-precipitation. Titanium substitution in gadolinium orthoferrite has transformed the perovskite phase to garnet phase confirmed by X-ray diffraction analysis. Tolerance factor of perovskite structure has been reduced from 0.81 to 0.78 for x=0.25 Ti substitution. Antiparallel G-type electron spins of GdFeO₃ has been distorted by structural change induced due to titanium substitution. Ferromagnetism has been increased to 0.74 emu/g from 0.5 emu/g by titanium substitution. Retentivity and coercivity has been also increased from 0.005 emu/g to 0.28 emu/g and 27 Oe to 218 Oe respectively. The increase in magnitude of ferromagnetic transition with respect of temperature has been significantly observed by high temperature magnetization measurement. Present process is easy to induce room temperature ferromagnetism in antiferromagnetic GdFeO₃ by distorting the structure at lower temperature by titanium substitution. The retentivity and coercivity produced at x=0.25 titanium substitution is useful for magnetic memory and switching application.

Keywords: Multiferroics, Antiferromagnetic, GdFeO₃, Magnetic Memory

1. Introduction: Rare earth orthoferrites exhibits distorted perovskite structure crystallize in *Pbnm* space group and exhibit weak ferromagnetic properties [1]. However, recently it is reported that some RFeO₃ systems such as EuFeO₃ and GdFeO₃ prepared by a low temperature chemical route exhibit better ferromagnetic properties [2]. The magnetic properties of rare earth orthoferrites are interesting because of the magnetic interactions of the two different types of magnetic ions: Fe³⁺ and R³⁺. The spin-exchange interaction mechanism among Fe–Fe, R–Fe and R–R ions leads to a few interesting phenomena in rare earth ortho-ferrite materials [3,4]. The magnetic properties of RFeO₃ systems at high temperature depend majorly on the Fe–Fe interactions that

lead to an antiferromagnetic type spin ordering with Neel temperatures ranging from 620 to 740 K [5,6]. With decrease in temperature about 100–200 K, the competition of the Fe–Fe and R–Fe interactions leads to a so-called spin-reorientation transition of the ordered Fe³⁺ magnetic moments [7]. Spin reorientation is a more general phenomenon observed in many compounds containing rare earth and iron ions. The crystal structure examined by X-ray photography reported to be twinned on a (110) plane. The displacements of the Gd³⁺ ions from the ideal positions were not very large, but the displacement was considerably larger in the *b* direction than in the *a* direction [8]. Gadolinium compounds are used as contrasting agents for magnetic resonance imaging due to its florescent

properties [9]. Antiferromagnetic gadolinium ortho ferrite has been studied for multiferroic properties by disturbing G-type antiferromagnetic spins by generating strain in the distorted perovskite structure [10-12].

In present work G-type antiferromagnetic ordering of GdFeO_3 has been disturbed by substituting titanium at Gd site synthesis by co-precipitation method. Characterization of pure and substituted nanocrystalline GdFeO_3 powder for the purpose of multiferroic effect has been analyzed. Room temperature magnetism has been obtained in GdFeO_3 perovskite system by titanium substitution. Phase analysis of the composition is done by taking X-ray diffraction pattern. A study of magnetic property of the composition is carried out using Vibrating Sample Magnetometer. Dielectric constant measurement of the compositions at room temperature is done by Impedance analyzer.

2. Experimental: Gadolinium ferrate $\text{Gd}_{1-x}\text{Ti}_x\text{FeO}_3$ ($x=0.0, 0.05, 0.10, 0.15, 0.20, 0.25$) was prepared by chemical co-precipitation method. Analytical grade precursors $\text{Gd}(\text{NO}_3)_3 \cdot 5\text{H}_2\text{O}$, $\text{C}_{12}\text{H}_{28}\text{O}_4\text{Ti}$, $\text{Fe}(\text{NO}_3)_3 \cdot 6\text{H}_2\text{O}$ has been taken in stoichiometric ratio in DI water. Precursor's solution kept at 80°C on magnetic stirring for homogeneous mixing. After one hour stirring solution was precipitated by ammonia solution. The precipitate was washed with DI water until neutral pH is reached. Filtrates were kept in oven for overnight drying at 100°C . The dried samples were presintered at 750°C for 24 h followed by pelletization and sintered at 1000°C for 8 h. Structural, electrical and magnetic measurements were done on sintered pellets.

3. Results and discussion

3.1. X-Ray Diffraction: X-ray diffraction pattern was carried out by Philips X-ray diffractometer (X-pert Pro). X-ray pattern was taken from angle $2\theta = 20$ to 80 with a step 0.02° with $\text{Cu K}\alpha$ source. The operating condition of

X-ray instrument was 40kV , 30mA . Figure 1 shows the diffraction pattern of $\text{Gd}_{1-x}\text{Ti}_x\text{FeO}_3$ ($x=0-0.25$). For $x=0.00$ and $x=0.05$ Ti substitution GdFeO_3 crystallized in perovskite phase [13]. Lattice constants for pure GdFeO_3 were calculated $a=5.30 \text{ \AA}$, $b=5.54 \text{ \AA}$, and $c=7.59 \text{ \AA}$ (orthorhombic) by hkl and d values obtained by X-ray diffraction pattern. For $x=0.10$ some garnet phase $\text{Gd}_3\text{Fe}_5\text{O}_{12}$ peaks start to appear with perovskite phase [14]. Perovskite structure tolerance factor $t = (r_A + r_X) / \sqrt{2}(r_B + r_X)$ has been calculated for Ti substitution at Gd site in table 1. Where A is Gd & Ti, B is Fe and X is Oxygen. According to Goldschmidt rule the tolerance factor t for a perovskite structure is below 0.7 and above 1 beyond which non-perovskite structure is formed. Structure of the minerals is dependent on the chemical composition. The compositions have been synthesized by chemical process so the diffusion of Ti and Fe ions is fast in sintering process. The valency of the Ti ions can be changed by sintering the material and may occupy tetrahedral and octahedral Fe sites. The ionic radii of Ti^{4+} (0.605 \AA) / Ti^{3+} (0.67 \AA) is comparable to Fe^{3+} (0.645 \AA) / Fe^{2+} (0.78 \AA) thus have a possibility to replace octahedral/tetrahedral site of Fe. Titanium substitution somehow relaxed the distorted perovskite into symmetric cubic garnet structure. Gadolinium is located in the center of eight coordinated dodecahedral distorted site.

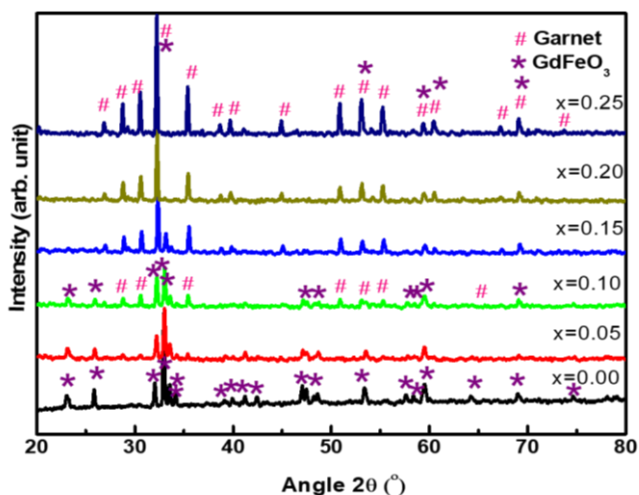


Figure 1. X-ray diffraction pattern of $Gd_{1-x}Ti_xFeO_3$ ($x=0-0.25$).

3.2. Scanning Electron Microscope: Surface microstructure of sintered $GdFeO_3$ and $x=0.25$ Ti substituted $GdFeO_3$ has been shown by SEM image in Figure 2 (a, b). SEM image shows small grains distribution and open pores present throughout the sample. The smaller grains are obtained due to chemical co-precipitation synthesis method. Grains seem to be fused by titanium substitution and collapse of pores visible in Fig 2b.

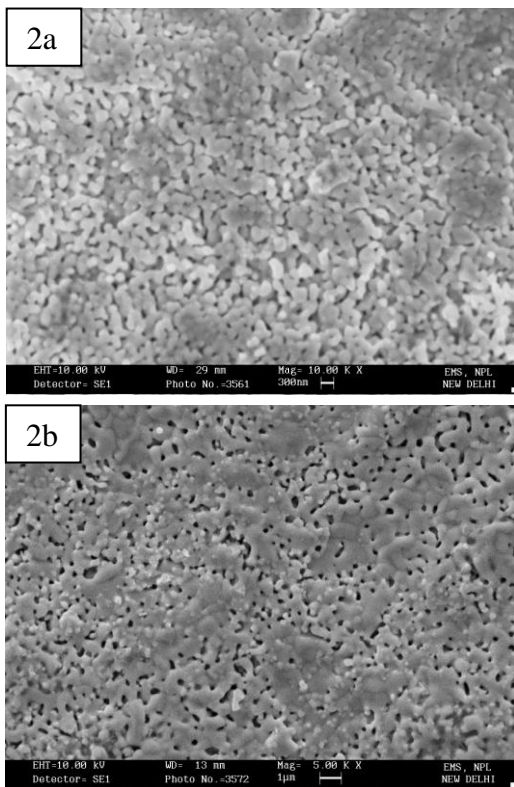


Figure 2. SEM image of $GdFeO_3$ (2a), and $Gd_{0.75}Ti_{0.25}FeO_3$ (2b).

3.3. Magnetization: Room temperature M-H loops were taken by vibrating sample magnetometer as shown in Figure 3. M-H loop shows a typical antiferromagnetic nature of $GdFeO_3$. At 5KOe the magnetic moment was quite low 0.5 emu/g as characteristic of antiparallel arranged spin moments. By increasing Ti substitution, low magnetic field magnetization starts to appear as well as

magnetic moment also increased. For the $x=0.25$ Ti substitution the retentivity of the composition increased to 0.28 emu/g signifies the spin are aligned at low applied magnetic field. This shows the switching behavior of the magnetic moment with reversible applied magnetic field. From XRD pattern it is observed that with Ti substitution perovskite phase converting towards garnet phase. The magnetic moment in garnet appears due to the antiparallel alignment as a result of exchange interaction between Fe^{3+} ions at tetra and octahedral sites with magnetic moment of Gd ions in c site give the net magnetic moment [15]. Thus, replacement of Gd ions by Ti ion is resulted into net magnetic moment observed by M-H loop. It has been clearly observed by X-ray diffraction that the perovskite structure is transforming to cubic garnet structure by titanium substitution in $GdFeO_3$.

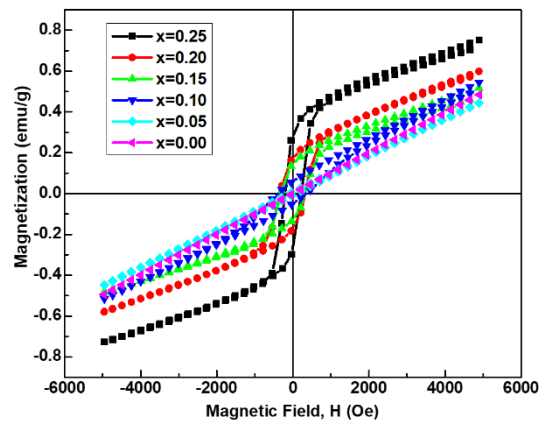


Figure 3. Room temperature magnetization vs. field of $Gd_{1-x}Ti_xFeO_3$ ($x=0.00-0.25$).

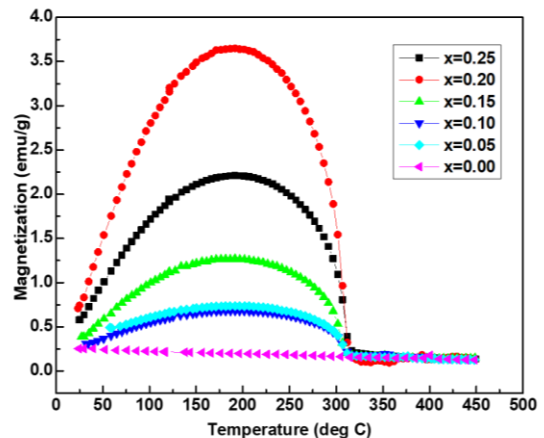


Figure 4. Magnetization vs. temperature plot for Gd_{1-x}Ti_xFeO₃ (x=0.00-0.25) series.

Gd _{1-x} Ti _x FeO ₃	Tolerance Factor	Magnetic Moment (emu/g)	Retentivity (emu/g)	Coercivity (Oe)
X=0	0.810	0.50	0.005	27
X=0.05	0.806	0.45	0.01	86
X=0.1	0.801	0.54	0.06	367
X=0.15	0.796	0.52	0.14	313
X=0.2	0.792	0.61	0.17	321
X=0.25	0.787	0.74	0.28	218

Table 1. Tolerance factor calculated for perovskite structure.

Figure 4 shows the plot between magnetization vs temperature graph of Gd_{1-x}Ti_xFeO₃ (x=0.0-0.25) series. Magnetization vs temperature plot shows typical ferrimagnetic sublattice Curie temperature curve. It is known that Fe³⁺ spins form an antiferromagnetic order along the **a** axis below T_{FeN} = 661 K with a weak ferromagnetic (WFM) component along the **c** axis due to the spin canting in the **ac** plane, which results from the Dzyaloshinskii-Moriya interaction. On the other hand, Gd³⁺ moments order antiferromagnetically along **a** axis below T_{GdN} = 2.5 K. Magnitude of ferrimagnetic spins increased upto x= 0.20, Ti substitution then with further substitution it decreased. This type of Curie temperature T_c (comp) often observed in sublattice-structured compounds. This T_c (comp) at which the net magnetisation is zero because the individual magnetisation of the sublattices have equal magnitudes but opposite signs. It is evident even from this short discussion that the magnetism of garnets, and especially the compensation temperature, is strongly dependent on crystallographic parameters.

4. Conclusions: Antiferromagnetic GdFeO₃ has been transformed to low field ferromagnetic garnet has been obtained by titanium substitution using chemical synthesis process. Perovskite phase has been formed at low temperature 750°C while by solid state reaction it requires prolong

heating above 1300°C for phase formation. By replacing Gd ions with Ti ions shows

ferrimagnetism at room temperature has been observed by inducing structural change. Magnetization vs. temperature plot confirms the

sublattice magnetization of the compound with transformation of phase. Highest retentivity of 0.28 emu/g at low applied magnetic field approximately 150 Oe at x=0.25, titanium substitution is applicable in magnetic switching and storage of magnetic moment at room temperature.

References:

1. S. Geller, Crystal structure of gadolinium orthoferrite GdFeO₃. J. Chem. Phys. 24, 1956, 1236–39.
2. Room temperature magnetoelectric coupling enhancement in Mg-substituted polycrystalline GdFeO₃, Scripta Materialia 67, 2012, 316–19.
3. S. Sahoo, P.K. Mahapatra, R.N.P. Choudhary, M.L. Nandagoswami, A. Kumar, Structural, electrical and magnetic characteristics of improper multiferroic: GdFeO₃. Mat. Res. Express 3, 2016, 065017.
4. C.S. Vandana, B.H. Rudramadevi, Effect of Cu²⁺ substitution on the structural, magnetic and electrical properties of gadolinium orthoferrite. Mat. Res. Express 5, 2018, 046101.
5. Landolt-Börnstein; Numerical Data and Functional Relationships in Science and Technology Group III, Vol 27f3, ed H P J Wijn; 1994
6. R.L. White, Review of Recent Work on the Magnetic and Spectroscopic Properties of the

- Rare Earth Orthoferrites, *Journal of Applied Physics* 40, 1969, 1061.
7. T. Yamaguchi, Theory of spin reorientation in rare-earth orthochromites and orthoferrites, *Journal of Physics and Chemistry of Solids*, 35(4) 1974, 479-500.
 8. J. D. Cashion, A.H. Cooke, D.M. Martin, M.R. Wells, Magnetic interactions in gadolinium orthoferrite. *J. Phys. C* 3, 1970, 1612–20.
 9. D. V. Korolev, G. A. Shulmeyster, M. S. Istomina, N. V. Evreinova, I. V. Aleksandrov, A. S. Krasichkov, V. N. Postnov, M. M. Galagudza, Fluorescently Labeled Gadolinium Ferrate/Trigadolinium Pentairon (III) Oxide Nanoparticles: Synthesis, Characterization, In Vivo Biodistribution, and Application for Visualization of Myocardial Ischemia–Reperfusion Injury, *Materials*, 15 (11), 2022, 3832.
 10. J. Shah, P. Bhatt, D. K. Dayas and R K Kotnala, Significant role of antiferromagnetic GdFeO₃ on multiferroism of bilayer thin films, *Materials Research Express*, 5 (2), 2018.
 11. E E. Ateia, B. Hussein, C. Singh and M. M. Arman, Multiferroic properties of GdFe_{0.9}M_{0.1}O₃ (M = Ag¹⁺, Co²⁺ and Cr³⁺) nanoparticles and evaluation of their antibacterial activity, *The European Physical Journal Plus*, 137(443) 2022.
 12. F. Bzour, A. Gismelseed, I. Z. Al-Yahmadi, et al. Structural, magnetic and mössbauer studies of GdFe_xMn_{1-x}O₃ multiferroic materials. *Hyperfine Interact*, 242(54), 2021.
 13. A. Ruffo, M. C. Mozzati, B. Albini, P. Galinetto and M. Bini, Role of non-magnetic dopants (Ca, Mg) in GdFeO₃ perovskite nanoparticles obtained by different synthetic methods: structural, morphological and magnetic properties, *Journal of Materials Science: Materials in Electronics*, 31, 2020, 18263–77.
 14. Y. Takumi, A. Junji, K. Yusuke, E Shuji, C Susumu, N Shoichi, Ferrimagnetic order in the mixed garnet (Y_{1-x}Gd_x)₃Fe₅O₁₂, *Philosophical magazine*, 85(17), 2005, 1819-33.
 15. M-lan Li, L. Zhang, N. Jiang, S-juan Zhong and L. Zhang, Influences of silicon carbide nanowires' addition on IMC growth behavior of pure Sn solder during solid–liquid diffusion, *Journal of Materials Science: Materials in Electronics*, 32, 2021, 18067–75.

Electronic Motion and Path Study in Presence of Varying Electric Field Using SciLab 6.1.1 for Coupled Differential Equations

Ravindra Singh*, Shiv Shankar Gaur

Department of Physics, Shivaji College (University of Delhi), Raja Garden New Delhi-110027.

Volume 1, Issue 2, March 2024

Received: 9 January, 2024; Accepted: 4 March, 2024

DOI: <https://doi.org/10.63015/5c-2412.1.2>

Corresponding author email: ravindrasingh@shivaji.du.ac.in

Abstract: The study of electronic motion of the electron and its path has been investigated using coupled linear differential equations in presence of electric field. The program executed using Scilab for the electronic motion. 2-D & 3-D trajectories of the electronic path and the variation and the distances in x & y directions with constant Electric field studied. Plotting of trajectories successfully done with Scilab software 6.1.1. Here L.T and with D'operator methods shows same results. 3-D trajectory of the electronic motion is periodic at particular frequencies; along y direction the electrons gain more energy and having more potential with increasing frequency and the investigation of oscillations under given conditions is found to be much higher.

Keywords: Scilab software 6.1.1 and electronic motion.

1. Introduction: The new approaches of the electron path had been studied in the last three decades very fast. Everywhere in this universe there is existence of the electronic motion. The electronic path motion is different in liquid nano plasma and liquid magnetite plasma. The electrons are negatively-charged particles having mass that is approximately $1/1836$ that of the proton and behave dual nature. The electronic world is everywhere in the form of mobile phones, software, electronic music, radio and television broadcasting, the electrical energy grid, air and space travel, engineering communications and a wide range of other areas. The study of electrons path with an experiment done and which interferes in the same manner as water, acoustical or light waves do [1-2]. The e/m , the ratio for e/m is 1.758820×10^{11} C/kg. Two simulation modules also can be used to find the value of e/m ratio for an electron. The electronic path is capable to send the signals from one part of machine to another. Electrical resistivity of metal wires shows that it increases as their width decreases [3-5]. The simulation of electron and particle in cell are very important these days. The mean free path λ of electron and carrier relaxation time τ of the twenty most conductive elemental metals are determined by numerical integration over the Fermi surface obtained from first-principles, using constant λ or τ approximations and wave-vector dependent Fermi velocities $v_f(\mathbf{k})$ [6]. The path of

a particle of mass m carrying a charge e is determined by the author (Herbert Stanley Allen) in combined magnetic and electric fields, when the lines of force are radial and are such as might be due to a single pole of strength μ coincident with an electric charge k [7]. The electrons orbiting around their common barycenter can form bound states and have a triplet spin structure which is independent of the center-of-mass momentum [8]. The resonance in spin can be induced by high-frequency electric fields in materials with a spin-orbit interaction; the oscillation of the electrons creates a momentum-dependent effective magnetic field acting on the electron spin [9-12]. The electron cyclotron drift instability driven by the electron $E \times B$ drift in partially magnetized plasmas that is investigated by Salomon Janhunen et.al. instability is so highly, resolved particle-in-cell simulations [13]. The existence of intense nonstationary processes in helical electron beams (HEB) is done experimentally by [14-15] and the study of helical electron beams (HEB) with disturbed axial symmetry of currents density and HEB with locking electrons in magnetic trap done by A. N. Kuftin et.al.

2. General Discussion: The path of an electron in a magnetic field is shown in figure 1 for which the magnetic force can be find by using the formula $Bev = mv^2/r$ where B is the magnetic field of strength, e is the electronic charge and v is the

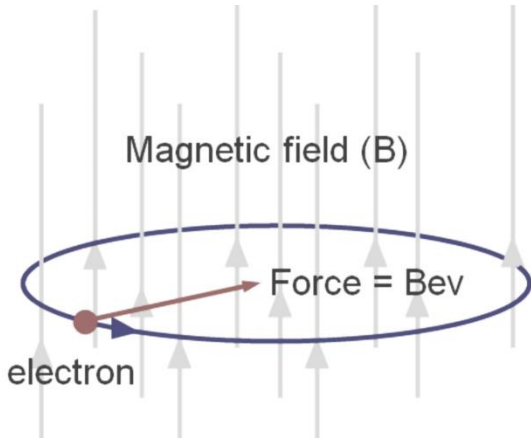


Figure 1: The path of an electron in presence of magnetic field

electron velocity. In a magnetic field the force is always at right angles to the motion of the electron (Fleming's left-hand rule) and so it shows that the path of the electron is circular as shown in Figure 2. Suppose the electron enters the field at an angle to the field direction then the path of the electron will be helical as shown in figure 3.

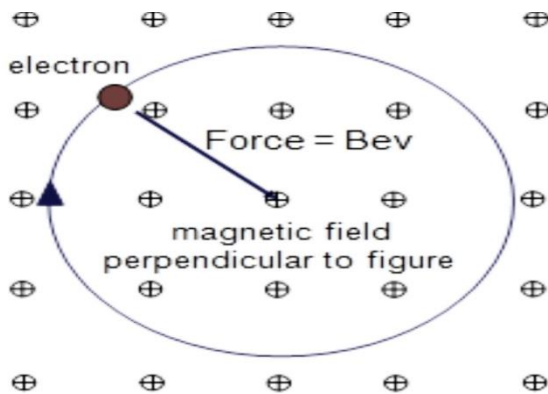


Figure 2: Circular path of the electron

The path of the electron in an electric field is given by the equation, $y = [Ev/2mdv^2] x^2$ where V is the potential difference between the plates which are aligned along the x direction and the electron enters the field at right angles to the field lines and $x = vt$ then the force equation on the electron is given by the equation: $F = eE = eV/d = ma$. Mass and charge of the electron respectively; mass of the electron, $m = 9.1 \times 10^{-31}$ kg and the charge of the electron, $e = 1.6 \times 10^{-19}$ J. So above is the equation of a parabola since for a given electron velocity y is proportional to x^2 . Figure 1 reveals about the motion of a charged particle in a uniform magnetic field having magnitude $F=qvB\sin\theta$ is acted where θ is the angle of velocity \mathbf{v} with the magnetic field \mathbf{B} . It was the general discussion

about the electron path. Now we focused on the equation of motion for the path of electron obtained by the coupled differential solved analytically. Now ignoring the magnetic effect.

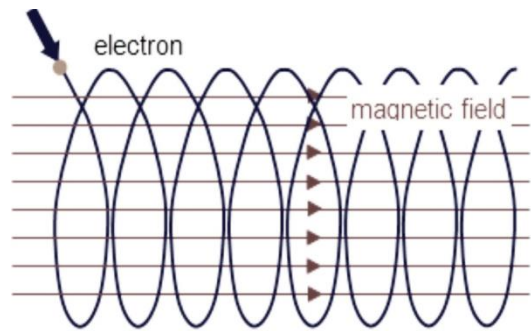


Figure 3: Helical motion of the electron

Here we are taking into account only Electric-field.

3. Electron Dynamics: Here we have to study of the path of electron for a set of coupled differential equations given below

$$m \frac{d^2x}{dt^2} + eh \frac{dy}{dt} = eE \quad \dots\dots(1)$$

$$m \frac{d^2y}{dt^2} + eh \frac{dx}{dt} = B \quad \dots\dots(2)$$

with conditions $x = \frac{dx}{dt} = y = \frac{dy}{dt} = 0$. Where m is the mass of the electron, $m = 9.1 \times 10^{-31}$ kg and the electronic charge, $e = 1.6 \times 10^{-19}$ C; x & y are the position coordinates.

Solution of the Equations: Solving equations (1) and (2); multiplying (2) by ξ (when magnetic field is zero) and adding to (1), we get

$$m \frac{d^2x}{dt^2} + m\xi \frac{d^2y}{dt^2} + eh \frac{dy}{dt} - eh\xi \frac{dx}{dt} = eE$$

$$m \frac{d^2}{dt^2} (x + \xi y) - eh\xi \frac{d}{dt} \left(-\frac{y}{\xi} + x \right) = eE \dots\dots(3)$$

Let us choose a parameter such that $x + \xi y = x - \frac{y}{\xi}$ on solving we get $\xi = \pm i$. Once we put $x + \xi y = \psi$

in (3), we have

$$m \frac{d^2\psi}{dt^2} - eh\xi \frac{d\psi}{dt} = eE$$

$$\frac{d^2\psi}{dt^2} - \omega\xi \frac{d\psi}{dt} = \frac{eE}{m} \quad \dots\dots(4)$$

The complete solution is given by

$\psi = c_1 + c_2 e^{\omega \xi t} - \frac{Et}{h\xi}$ as $x + \xi y = \psi$ then we can write

$$x + \xi y = c_1 + c_2 e^{\omega \xi t} - \frac{Et}{h\xi} \quad \dots\dots(5)$$

In equation (5) putting the value of ξ i.e. $i = -i$, we get

$$x + iy = c_1 + c_2 e^{i\omega t} - \frac{Et}{ih} \quad \dots\dots(6)$$

$$x - iy = c_3 + c_4 e^{-i\omega t} + \frac{Et}{ih} \quad \dots\dots(7)$$

The differentiation of above equations (6) and (7) takes form

$$\frac{dx}{dt} + i \frac{dy}{dt} = c_2 i\omega e^{i\omega t} + \frac{iE}{h} \quad \dots\dots(8)$$

$$\frac{dx}{dt} - i \frac{dy}{dt} = -i\omega c_4 e^{-i\omega t} - \frac{iE}{h} \quad \dots\dots(9)$$

Now using initial conditions, $x = y = \frac{dx}{dt} = \frac{dy}{dt} = 0$ when $t = 0$ in (6), (7), (8) and (9), we get

$$x = \frac{E}{h\omega} [1 - \cos(\omega t)] \quad \dots\dots(12)$$

$$y = \frac{E}{h\omega} [\omega t - \sin(\omega t)] \quad \dots\dots(13)$$

Equations (12) and (13) represents the equations of the path for electron for given set of coupled differential equations. Further we solve the equations using Laplace transform. Let the Laplace transform of x be $\mathcal{L}[x] = \bar{x}$ and $\mathcal{L}[y] = \bar{y}$.

$$\mathcal{L}\left[\frac{d^2x}{dt^2}\right] = p^2 \mathcal{L}[x] - p x(0) - x'(0) \text{ and}$$

$$\mathcal{L}\left[\frac{d^2y}{dt^2}\right] = p^2 \mathcal{L}[y] - p y(0) - y'(0)$$

$$\mathcal{L}\left[\frac{dx}{dt}\right] = p\bar{x} - x(0) \text{ and } \mathcal{L}\left[\frac{dy}{dt}\right] = p\bar{y} - y(0)$$

$$p^2\bar{x} - p x(0) - x'(0) + \frac{eh}{m} [p\bar{y} - y(0)] = \frac{eE}{mp} \quad \dots\dots(14)$$

$$p^2\bar{y} - p y(0) - y'(0) - \frac{eh}{m} [p\bar{x} - x(0)] = 0 \quad \dots\dots(15)$$

Now use the given conditions $x(0) = 0$; $x'(0) = 0$ & $y(0) = 0$; $y'(0) = 0$ above equations takes form

Figure 4: Shows the variation of path ‘E’ Vs ‘r²’ (a) $\omega = \pi/2$; (b) $\omega = \pi/3$

$$p^2\bar{x} + \frac{eh}{m} [p\bar{y}] = \frac{eE}{mp} \quad \dots\dots(16)$$

$$\text{and } p^2\bar{y} - \frac{ehp\bar{x}}{m} = 0 \quad \dots\dots(17)$$

Solving above equations for x and y we get

$$\bar{x} = -\left(\frac{eE}{m}\right) \frac{1}{p(p^2 + (\frac{eh}{m})^2)} \text{ and}$$

$$\bar{y} = -\left(\frac{eh}{m}\right)^2 \frac{1}{p^2(p^2 + (\frac{eh}{m})^2)}$$

Now the result given below has been solved by using partial fractions.

$$x = -\left(\frac{eE}{m}\right) \left\{ L^{-1}\left[-\left(\frac{m}{eh}\right)^2 \cdot \frac{1}{p}\right] + L^{-1}\left[\left(\frac{m}{eh}\right)^2 \cdot \frac{p}{p^2 + (\frac{eh}{m})^2}\right] \right\} \quad \dots\dots(18)$$

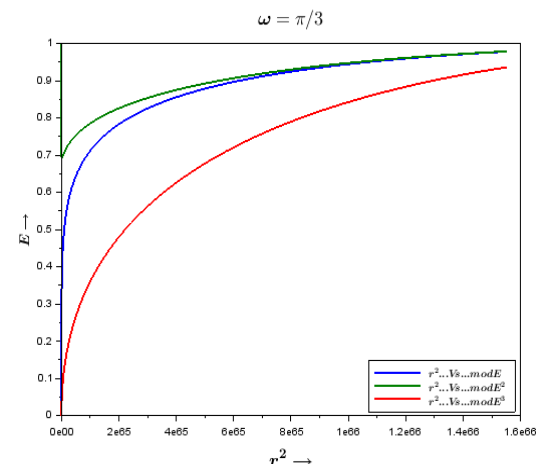
$$y = \frac{E}{h} \left[t - \frac{m}{eh} \sin\left(\frac{eh}{m}t\right) \right] \quad \dots\dots(19)$$

Put $\omega = \frac{eh}{m}$ in above equations we have

$$x = \frac{E}{h\omega} [1 - \cos(\omega t)] \quad \dots\dots(20)$$

$$y = \frac{E}{h\omega} [\omega t - \sin(\omega t)] \quad \dots\dots(21)$$

Equations (20) and (21) represents the equations of the path for electron for given set of coupled differential equations. On comparing four equations (12) & (20); (13) and (21) are found to be same. Next we analyzed the same equations



using Scilab software.

4. Results: Figure 4 is the variation of Electric

field, E and r^2 where $r = \sqrt{x^2 + y^2}$. Here it is observed that E increases with respect to r at some frequencies $\omega = \pi/2$ & $\omega = \pi/3$. Electric field is proportional to distance. When r is very high then a saturation is found for all the curves for limited time. The sharp result comes out when $\omega = \pi/2$ for large 't' the plot line converts into a tedious path like scattering of particles. Green line is the curve between 'r²' Vs 'modulus of E'.

Figure 5(a)-5(d) represents electron trajectory in the $x - y$ plane. The plots of both solutions are against one another at a constant value of field, increasing in equal steps and the frequency is also increasing from 5(a)-5(d). The plots show the variation of x and y for a fixed value of time for

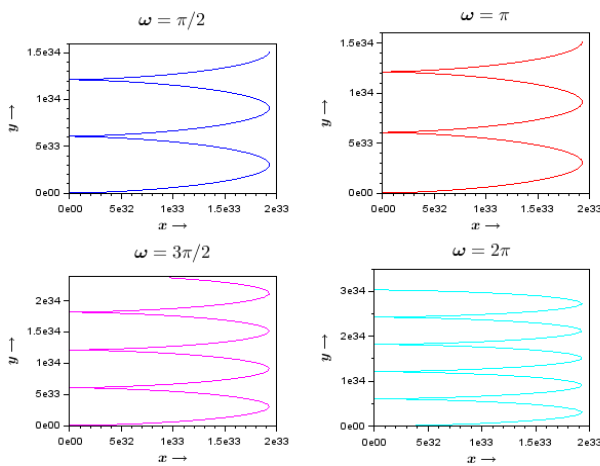


Figure 5: Shows the variation of path y Vs x . For (a) $\omega = \pi/2$; (b) $\omega = \pi$; (c) $\omega = 3\pi/2$; and (d) $\omega = 2\pi$.

each. Mathematically it is noticed from the graph that y is multivalued function, angular frequency doesn't matter in this case here. So it is observed that along y direction the electrons gains more energy or having more potential with increasing frequency and the oscillations under some conditions are found to be much higher. The Hamiltonian as well as the momentum and kinetic energy attains high value in y direction. The classical theoretical aspects are also valid here. If we use variational process, we can restrict the comparison of all paths involving no violation of conservation of energy and momentum also the Hamiltonian, H will be conserved.

Figure 6(a)-6(c) represents 3D electron trajectory. The 3-D trajectory has been studied with the help of latest Scilab software for particular values of angular frequencies $\omega = \pi/2$, $\omega = \pi/3$ and $\omega = \pi/4$. 3-D trajectory depends upon the angular frequency; in the study it has been found that on decreases the angular frequency there is increment in trajectory

loops and the separation between them becomes so close and looks like spiral or human ribs shape.

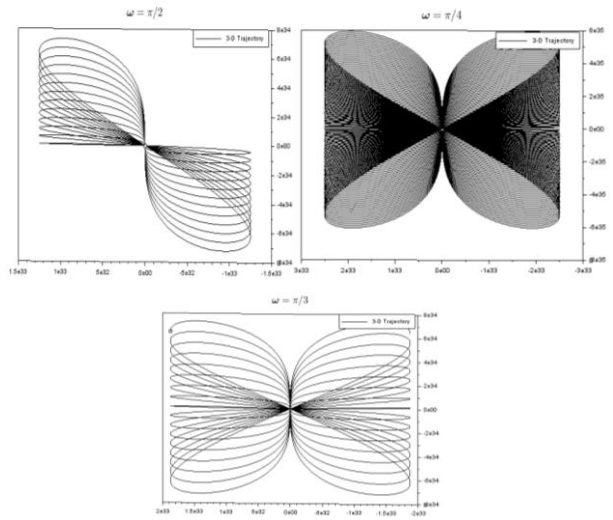


Figure 6: Shows the variation of path y Vs x . For (a) $\omega = \pi/2$; (b) $\omega = \pi$; (c) $\omega = 3\pi/2$.

The figure formed from the trajectory is found to be symmetry with respect to x and y and also about $y=x$ at some particular angular frequencies.

Scilab Coding: Scilab programming/coding done successfully. The coding of Scilab for figure 4 follows as:

```

clc;
funcprot(0);
e=(1.6)*1e-19;
h=(6.6)*1e-34;
m=(9.1)*1e-31;
w=%pi/2;
t=linspace(0,1.3,500);
E=sin(w.*t);
x=(E/(h.*w)).*(1-cos(w.*t));
y=(E/(h.*w)).*(w.*t-sin(w.*t));
r=sqrt(x.^2+y.^2);
plot(r.^2,abs(E),r.^2,abs(E.^E),r.^2,abs(E.^3),'thickness',
2)
xstring(5e34,-.5,['(a)'],0,1)
xlabel('\boldsymbol{r^2\rightarrow}\$', 'fontsize',4)
ylabel('\boldsymbol{E\rightarrow}\$', 'fontsize',3)
legend('\boldsymbol{r^2...Vs...mod E\$', '\boldsymbol{r^2...Vs...mod E^2\$', '\boldsymbol{r^2...Vs...mod E^3}\$',4)

title('\boldsymbol{\text{\omega}=\pi/2}', 'fontsize',4)

```

```

clc;
funcprot(0);
e=(1.6)*1e-19;
h=(6.6)*1e-34;
m=(9.1)*1e-31;
w=%pi/3;
t=linspace(0,1.3,500);
E=sin(w.*t);
x=(E/(h.*w)).*(1-cos(w.*t));

```

```

y=(E/(h.*w)).*(w.*t-sin(w.*t));
r=sqrt(x.^2+y.^2);
plot(r.^2,abs(E).r.^2,abs(E.^E),r.^2,abs(E.^3),'thickness',
2)
xstring(5e34,-.5,["(a)"],0,1)
xlabel('$\boldsymbol{x}\rightarrow$', 'fontsize',4)
ylabel('$\boldsymbol{y}\rightarrow$', 'fontsize',3)
legend('$\boldsymbol{r}^2$ Vs...mod
E$', '$\boldsymbol{r}^2$ Vs...mod
E^2$', '$\boldsymbol{r}^2$ Vs...mod E^3$',4)
title('$\boldsymbol{\text{\omega}}=\pi/3$', 'fontsize',4)

```

Scilab programming/coding done successfully. The coding of Scilab for figure 5 follows as

```

clc;
funcprot(0);
e=(1.6)*1e-19;
h=(6.6)*1e-34;
m=(9.1)*1e-31;
w=%pi/2;
E=1;
t=linspace(0,10,100);
x=(E/(h.*w)).*(1-cos(w.*t));
y=(E/(h.*w)).*(w.*t-sin(w.*t));
subplot(2,2,1)
plot(x,y,'thickness',1)
xstring(1e33,5.9e34,["(a)"],0,1)
xlabel('$\boldsymbol{x}\rightarrow$', 'fontsize',3)
ylabel('$\boldsymbol{y}\rightarrow$', 'fontsize',3)
title('$\boldsymbol{\text{\omega}}=\pi/2$', 'fontsize',4)
w=%pi;
E=2;
t=linspace(0,5,100);
x=(E/(h.*w)).*(1-cos(w.*t));
y=(E/(h.*w)).*(w.*t-sin(w.*t));
subplot(2,2,2)
plot(x,y,'r','thickness',1)
xstring(1e33,1.2e35,["(b)"],0,1)
xlabel('$\boldsymbol{x}\rightarrow$', 'fontsize',3)
ylabel('$\boldsymbol{y}\rightarrow$', 'fontsize',3)
title('$\boldsymbol{\text{\omega}}=\pi$', 'fontsize',4)
w=3*%pi/2;
E=3;
t=linspace(0,5,100);
x=(E/(h.*w)).*(1-cos(w.*t));
y=(E/(h.*w)).*(w.*t-sin(w.*t));
subplot(2,2,3)
plot(x,y,'m','thickness',1)
xstring(1e33,1.7e35,["(c)"],0,1)
xlabel('$\boldsymbol{x}\rightarrow$', 'fontsize',3)
ylabel('$\boldsymbol{y}\rightarrow$', 'fontsize',3)
title('$\boldsymbol{\text{\omega}}=3\pi/2$', 'fontsize',4)
w=2*%pi;
E=4;
t=linspace(0,5,100);
x=(E/(h.*w)).*(1-cos(w.*t));
y=(E/(h.*w)).*(w.*t-sin(w.*t));
subplot(2,2,4)
plot(x,y,'c','thickness',1)
xstring(1e33,2.5e35,["(d)"],0,1)
xlabel('$\boldsymbol{x}\rightarrow$', 'fontsize',3)
ylabel('$\boldsymbol{y}\rightarrow$', 'fontsize',3)
title('$\boldsymbol{\text{\omega}}=2\pi$', 'fontsize',4)

```

Scilab programming/coding done successfully. The coding of Scilab for figure 6 follows as

```

clc;
funcprot(0);
e=(1.6)*1e-19;
h=(6.6)*1e-34;
m=(9.1)*1e-31;
w=%pi/2;
t=linspace(0,50,5000);
E=sin(w.*t);
x=(E/(h.*w)).*(1-cos(w.*t));
y=(E/(h.*w)).*(w.*t-sin(w.*t));
r=sqrt(x.^2+y.^2);
comet3d(t,x,y)
xstring(5e34,-.5,["(a)"],0,1)
legend('3-D Trajectory')
title('$\boldsymbol{\text{\omega}}=\pi/2$', 'fontsize',4)

```

```

clc;
funcprot(0);
e=(1.6)*1e-19;
h=(6.6)*1e-34;
m=(9.1)*1e-31;
w=%pi/3;
t=linspace(-50,50,10000);
E=sin(w.*t);
x=(E/(h.*w)).*(1-cos(w.*t));
y=(E/(h.*w)).*(w.*t-sin(w.*t));
r=sqrt(x.^2+y.^2);
comet3d(t,x,y)
xstring(5e34,-.5,["(a)"],0,1)
legend('3-D Trajectory')
title('$\boldsymbol{\text{\omega}}=\pi/3$', 'fontsize',4)

```

```

clc;
funcprot(0);
e=(1.6)*1e-19;
h=(6.6)*1e-34;
m=(9.1)*1e-31;
w=%pi/4;
t=linspace(-400,400,10000);
E=sin(w.*t);
x=(E/(h.*w)).*(1-cos(w.*t));
y=(E/(h.*w)).*(w.*t-sin(w.*t));
r=sqrt(x.^2+y.^2);
comet3d(t,x,y)
xstring(5e34,-.5,["(a)"],0,1)
legend('3-D Trajectory')
title('$\boldsymbol{\text{\omega}}=\pi/4$', 'fontsize',4)

```

5. Conclusions: The motion of the electron is determined for a set of coupled linear differential equation of second order under certain conditions with an electric field. The opted methods give the same result and verified with the software. The presence if the electric field is considered constant as well as in trigonometric form; the path of the electron is analyzed and the trajectories of the electron and the variation of r with E have been studied. Scilab software 6.1.1 used throughout the plotting and the problem is analysed with it. The

importance of the software is that it gives more accurate study of trajectories, variation with distance and symmetry with angular frequencies. Using Scilab the amplitude/oscillations under given conditions are found to be much higher for path, y . The momentum and kinetic energy found to be high in y direction as compared to x direction. 3-D trajectory depends upon the angular frequency and found to be symmetry with respect to x and y and also about $y=x$.

References:

1. Matija Karalic, Antonio Štrkalj, Michele Masseroni, Wei Chen, Christopher Mittag, Thomas Tschirky, Werner Wegscheider, Thomas Ihn, Klaus Ensslin, Oded Zilberberg, “Electron-Hole Interference in an Inverted-Band Semiconductor Bilayer”, *Physical Review X*, 2020; 10 (3)
2. *Journal of the Institution of Electrical Engineers IET* **2** (14), 112 – 114 (1956).
3. R. L. Graham, G. B. Alers, T. Mountsier, N. Shamma, S. Dhuey, S. Cabrini, R. H. Geiss, D. T. Read, and S. Peddeti, “Resistivity dominated by surface scattering in sub-50nm Cu wires”, *Appl. Phys. Lett.* **96**, 042116 (2010).
4. K. Barmak, A. Darbal, K. J. Ganesh, P. J. Ferreira, J. M. Rickman, T. Sun, B. Yao, A. P. Warren, and K. R. Coffey, “Surface and grain boundary scattering in nanometric Cu thin films: A quantitative analysis including twin boundaries”, *J. Vac. Sci. Technol. A* **32**, 061503 (2014).
5. J. S. Chawla, F. Gstrein, K. P. O'Brien, J. S. Clarke, and D. Gall, “Electron scattering at surfaces and grain boundaries in Cu thin films and wires”, *Phys. Rev. B* **84**, 235423 (2011).
6. Daniel Gall, “Electron mean free path in elemental metals”, *Journal of Applied Physics* **119**, 085101 (2016); <https://doi.org/10.1063/1.4942216>
7. Herbert Stanley Allen, “The path of an electron in combined radial magnetic and electric fields”, *Memoirs of Fellows of the Royal Society* **1**, 5–10 (1911).
8. Yasha Gindikin and Vladimir A. Sablikov, “Spin-orbit-driven electron pairing in two dimensions”, *Phys. Rev. B* **98**, 115137 (2018).
9. Zavoisky, Y. K., “Spin magnetic resonance in para-magnetics”, *J. Phys. USSR* **9**, 245–246 (1945).
10. Dyakonov, M. I. & Perel, V. I., “Spin relaxation of conduction electrons in non-centrosymmetric semiconductors”, *Sov. Phys. Solid State* **13**, 3023–3026 (1972).
11. Rashba, E. I. & Efros, A. L., “Orbital mechanisms of electron-spin manipulation by an electric field”, *Phys. Rev. Lett.* **91**, 126405 (2003).
12. Duckheim, M. & Loss, D., “Electric-dipole-induced spin resonance in disordered semiconductors”, *Nature Phys.* **2**, 195–199 (2006).
13. S. Janhunen et.al., “Evolution of the electron cyclotron drift instability in two-dimensions”, *Physics of Plasmas* **25**, 082308 (2018).
14. B.V. Raisky & S.E. Tsimring, “Numerical simulation of nonstationary processes in intense helical electron beams of gyrotrons”, *IEEE Transactions on Plasma Science* **24**, 3 1996.
15. V. K. Lygin, V. N. Manuilov, B. V. Raisky, E. A. Solujanova & Sh. E. Tsimring, “Theory of helical electron beams in gyrotrons”, *International Journal of Infrared and Milli meter Waves* **14**, 783–816 (1993).

Laser Induced Damage Study of Dye Doped Polystyrene Films deposited in Glass Substrate by Dip Coating Technique

Amit Pratap Singh^{1*}, Shiv Shankar Gaur²

¹Independent Researcher, Indore – 452005 (M.P.), India.

²Shivaji College, University of Delhi, Raja Garden, New Delhi-27

Volume 1, Issue 2, March 2024

Received: 18 January, 2024; Accepted: 1 March, 2024

DOI: <https://doi.org/10.63015/5c-2415.1.2>

Correspondence author email: aps75@rediffmail.com

Abstract: In the present work, the Laser-induced Damage Morphology of Dye-doped Polystyrene films is investigated. The focus is on the Front and Rear side Damage Morphology at two different Pulse Repetition Frequencies, namely 1 pps and 20 pps. For this experiment, films were deposited on both sides of Borosilicate Glass. It was found that at 1 pps, the front side film is damaged without affecting the glass, while the modified beam propagates through the glass to damage the rear side film. Dendrimer-like microstructures are found on both the front and rear sides of the damaged spots, along with pits and craters. At 20 pps frequency, the front side film is damaged, including damage to the glass, resulting in a large crater on the front surface. The morphological features were studied using Fresnel equations. Polymeric films were fabricated using the Dip Coating Technique, and Film thickness was evaluated using the Prism Coupling technique.

Keywords: Laser Induced Damage; Polymeric Films; Dendrimer; Prism Coupling; Dip Coating.

1. Introduction

The microprocessing of Polymers using High power lasers has great importance as it provides good precision and control at micron and nano level. The laser-matter interaction not only depend upon the materials composition but also depend upon the various laser parameters e.g. laser wavelength, pulse repetition frequency and pulse duration (in case of pulsed laser), energy of the laser beam etc. Recently, laser based various methods were reported by different research groups. For example, Rybaltovskii et al has created linear periodic structure in poly-2,20-poxydiphenylene-5,50-bis-benzimidazole (OPBI) by laser drawing process (Rybaltovskii et al.2021). Similarly polymeric surface were modified using Excimer laser based ablation technique for the fabrication of microfluidic systems (Hsieh et al. 2017). Laser ablation studies were performed on poly(dimethyl siloxane) (PDMS),

poly(glycerol sebacate) (PGS) and poly(1,3-diamino-2-hydroxypropane-co-polyol sebacate) (APS) polymers. Laser ablation technique was employed (Tazdidzadeh et al, 2017) to synthesize gold nanoparticle in polyethylene glycol and chitosan solutions. Q switched Nd:YAG pulsed laser were used for the synthesis. Ultrathin Polymeric films on Quartz substrate were ablated using Femtosecond laser by (Jun et al. 2016) to study thin film patterning process. Depending upon the pulse energy it was reported that films can be ablated with or without substrate. The mechanism of ablation was reported to be non-thermal. Photothermal ablation of polymers were analyzed (Kappes et al. 2014) using the temperature measurement setup based on spectral pyrometry. They performed their experiment on Polystyrene, poly (α -methylstyrene), a polyimide and triazene polymer using μ s laser. Surface patterning in doped polymers were also studied

(J.Vapaavuori et al. 2013). Surface Relief Gratings were inscribed in Polymers using laser irradiation. These reported works suggest that Laser-materials processing has great prospect in the area of Polymer synthesis and microprocessing technology. Polymeric materials are cost effective and easy to process. But the unique features offered by Laser beam provides a new dimension in Materials Processing. One such finding of laser microprocessing is reported in the present work in which polymeric films were converted into micron to nano level dendrimers. Absorbing dyes were doped in the polymeric chemistry and used as a catalyst to initiate damage in the polymeric films.

The present work reports the front and rear side damage morphology of Dye doped Polystyrene films fabricated on Borosilicate Glass. Damage morphology is studied using two different pulse repetition frequency-1pps and 20pps. The experiments were performed with Nd:YAG Laser (Wavelength $1.06\mu\text{m}$, pulse duration 20 ns). Polystyrene films are transparent at $1.06\mu\text{m}$, but doping of Methyl red dye makes polymeric film absorbing.

2. Experimental Details: In the present experiment, the damage was performed using Q-switched Nd:YAG laser (wavelength $1.06\mu\text{m}$, pulse duration 20ns). The pulse repetition frequency was used in two modes: 1pps (pulse per second) and 20pps mode. 1 pps was controlled manually while 20 pps was set in automatic mode. The pulse repetition frequency was changed by changing the fringe rate of flash lamp. The output laser beam has Gaussian profile. The beam diameter was determined using slit scan technique. The laser beam in TEM00 mode was focused by a lens of 45cm focal length. The incident energy was adjusted using Neutral Density Filters. He:Ne laser beam (frequency stabilized) was used as a probe beam. It was set to the spot to be damaged and reflected beam was collected by Si photodiode as shown in figure. The He:Ne laser beam size

was kept smaller than the Nd:YAG laser spot size. The reflected intensity from damaged spot is decreased and this decrease is always permanent. The present experiment was performed in air, at room temperature and under normal atmosphere. As shown in Fig.1 laser beam interacts with dye doped polystyrene film deposited on both sides of Borosilicate glass.

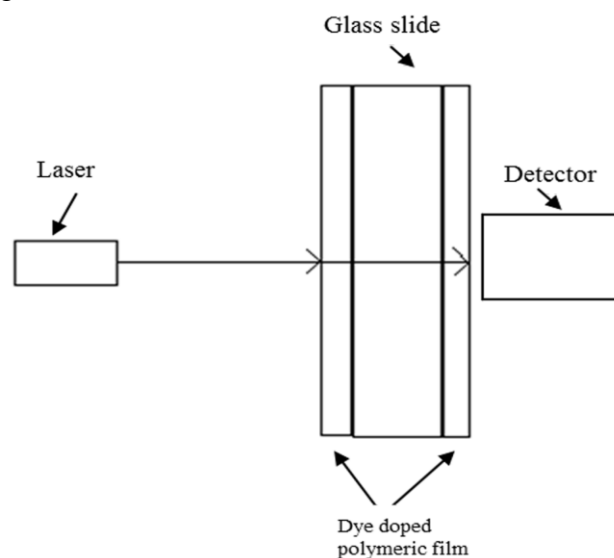


Figure 1. showing the setup of front and rear side Damage experiment

Energy levels in both 1pps and 20pps were fixed to single pulse damage threshold. Single shot damage was first observed using the energy of 0.13 J/cm^2 while the beam diameter was about 1mm. Then damage was also produced using double the energy value of the damage threshold. With reference to fig.1, the film facing to the laser is called herewith front-side film and the film deposited in the other side of the glass slide is called herewith rear-side film.

To define the damage threshold, the film surface was irradiated by laser beam by varying the fluence gradually. For each fluence level data were collected from different places of the film. Damage threshold values were found to be the same at each site. Irradiated spots were studied using SEM to make sure if any modification occurred.

The dye doped films were fabricated on the Borosilicate Glass by Dip Coating technique in clean room environment. The details about the technique can be found in the reference (Kumar et al 2005) Polystyrene was dissolved in Chlorobenzene (10% wt./vol) and Methyl Red dye was mixed in such a manner that its percentage was maintained at 0.3 %. Films were dried in the vacuum oven overnight at room temperature to evaporate the excess solvent in the film. The refractive index and extinction coefficient of polystyrene films at $1.06 \mu\text{m}$ were found to be 1.57 and 9.5×10^{-7} respectively. To correlate the different physical and optical parameters of polymer films same sample was first characterized for refractive index evaluation and then sample was placed into laser damage experimental setup for damage experiments.

Film thickness was evaluated using Prism Coupling technique (Kumar et al 2005). Since these films have waveguiding capabilities, thickness of the film can be found using Prism Coupling technique. The He:Ne Laser beam ($0.6329 \mu\text{m}$) enters into the film with the help of input prism (refractive index 1.756 at laser wavelength). The m-line spectroscopy was performed and waveguiding modes were observed using output prism (refractive index 1.756 at laser wavelength).

3. Results and Discussion

3.1 Damage Morphology in 20 pps regime:

Fig.2(a) shows the damaged spot using 20pps pulse at the energy of 1mJ. The depth of the spot is around $100 \mu\text{m}$. The film thickness was evaluated by Prism Coupling Technique and is found to be $20 \mu\text{m}$. That means Damage involved Glass as well. Comparatively larger values of Damage threshold of Borosilicate Glass in the similar conditions were reported by other groups (Kimmel et al. 2011). In this work the lesser value of Damage may be due to absorbing film (the presence of absorbing dyes

in transparent polymer chemistry) fabricated on glass.

In the damaged spot a big crater is formed. Surface removal, Striations (Fig.2b), crack (Fig.2c) are some of the noticeable feature that defines damage morphology in 20pps regime. In the back side of the system no damage in the film is formed that was concluded by SEM studies. This may be due to damage in Bulk Glass that results in no further propagation of laser pulse in the system. The periphery of the damaged spot in Fig.2a shows that mixed type of damage morphology which involves melting, crack, burning etc.

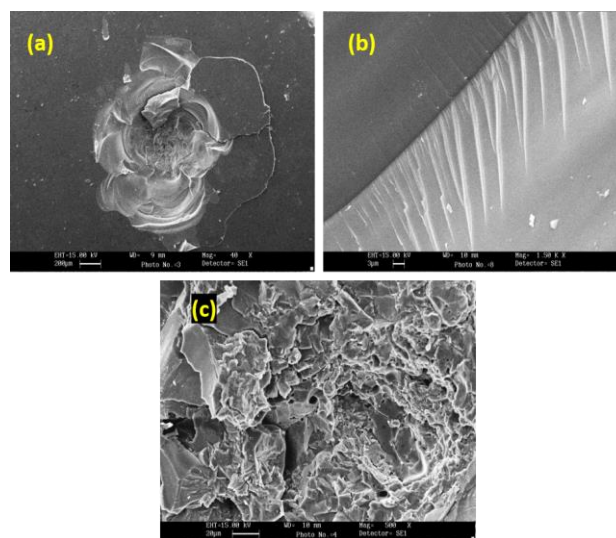


Figure 2. (a) showing the damaged spot with 20pps laser pulse, (b) showing the formation of striations in the damaged spot shown in fig.2a, (c) showing the central portion of damaged spot. Ablation and cracks are clear in the figure.

3.2 Damage Morphology in 1 pps regime

Fig.3a shows the damaged spot at the front end of the film. In this regime the complete film removal can be observed that not involves the glass. The periphery of the damaged spot shows the clear boundaries that are absent in the 20 pps regime. The enlarged view of the periphery (Fig.3b) shows the layered structure that suggests the surface removal through melting.

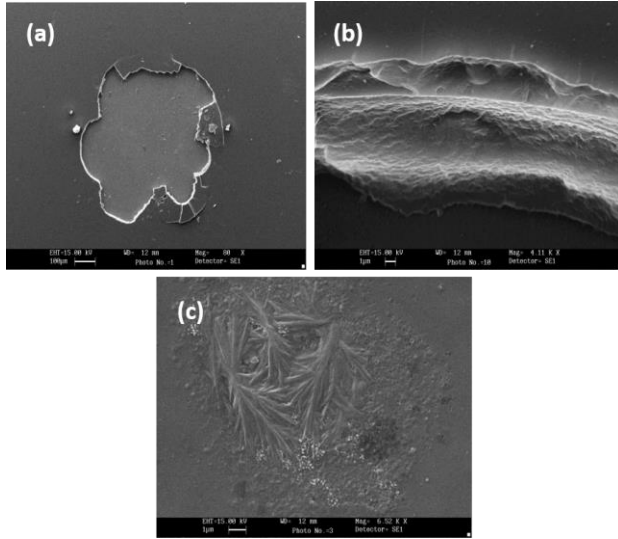


Figure 3. (a) showing the damaged spot using the 1pps pulse at threshold fluence, (b) showing the periphery of the damaged spot shown in fig.3a, (c) showing the dendrimer structure deposited in the glass in the damaged regionig.3

In the damaged spot, the glass surface is filled with some micro-particles (Fig.3c) whose enlarged view suggests the formation of dendrimer like structure (Folgado et al 2016). When the energy is increased to two times, the similar kind of morphology was found in the form of film removal in both sides of the glass without any damage to Glass (Fig.4a). But in the periphery (Fig.4b), layered structure is absent suggesting that film removal does not involve melting.

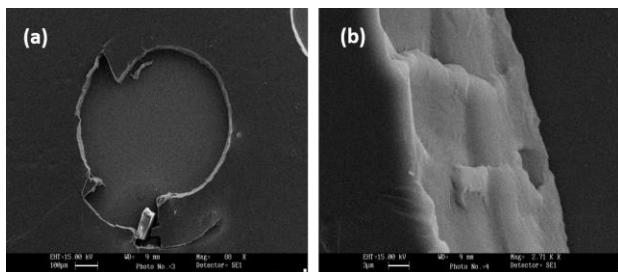


Figure 4. (a) showing the damaged spot using two times energy of damage threshold, (b) showing the periphery of the damaged spot.

Fig.5a shows the rear side damage morphology at the damage threshold value. The complete damaged spot is made of pits and cracks.

Dendrimers exists also in the rear side of damage morphology (Fig.5b). Complete film removal in rear side is absent that may be due to modification in the beam profile after crossing the front side damaged spot. When the energy is increased the similar trend can be seen in rear side film in the form of pits and cracks. But at higher energy level, more area is covered by this morphology, in the form of pits and cracks (Fig.5c and 5d).

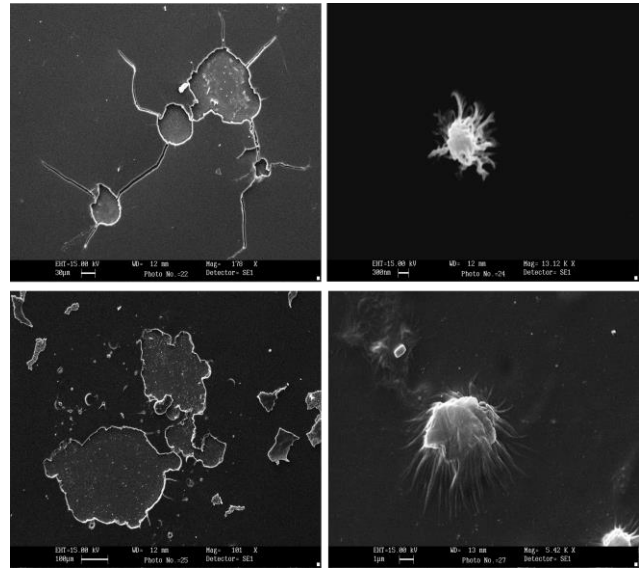


Figure 5. (a) showing the rear side damage at damage threshold value, (b) dendrimer structure in rear side damage shown in fig.5a, (c) rear side damaged spot at two times the damage threshold value, (d) showing the dendrimer in the damaged spot shown in fig 5c.

The difference in the damage morphology of entrance and exit face can be understood as follows:

In fig.1, when light enters into the films (side I), it suffers 180^0 phase shift (Crisp et al 1972). Therefore, due to partial destructive interference, the electric field strength at the film surface (side I), E_{ent}^{fl} can be related to the electric field of incident light E_i , by the following relation

$$E_{ent}^{fl} = E_{R1} + E_i = \frac{2}{n_1 + n_2} \dots\dots\dots(1)$$

Here E_{R1} is the electric field of reflected light from the film (side I), n_I is the refractive index

of film, n_2 is the refractive index of cover (in the present experiment the cover is air therefore the value of n_2 is 1). Now the light with reduced electric field will transmit through the film and incident into the glass surface. At the film-glass interface there will be no phase shift (Boling et al. 1972). Therefore, due to constructive interference at film-glass interface, the electric field becomes

$$\begin{aligned}
 E_{fl}^g &= E_{R2} + E_{ent}^{fl} = \frac{n_2 - n_3}{n_2 + n_3} E_{ent}^{fl} + E_{ent}^{fl} \\
 &= \left(\frac{2n_2}{n_2 + n_3} \right) \left(\frac{2}{n_2 + 1} \right) E_i \\
 &= \frac{4n_2}{(1 + n_2)(n_2 + n_3)} E_i = E_g \dots\dots\dots(2)
 \end{aligned}$$

Here E_{R2} is the electric field of reflected beam from the glass surface. This transmitted beam through the glass slide will again incident into the film (side II). Again due to 180° phase shift there will be destructive interference at the glass-film interface. The electric field will take the form

$$\begin{aligned}
 E_g^{fl} &= E_{R3} + E_g \\
 &= \left(\frac{n_3 - n_2}{n_3 + n_2} \right) E_g + E_g = \frac{2n_3}{n_3 + n_2} E_g \\
 &= \left(\frac{2n_3}{n_3 + n_2} \right) \left(\frac{4n_2}{(1 + n_2)(n_3 + n_2)} \right) E_i \\
 &= \frac{8n_2n_3}{(1 + n_2)(n_2 + n_3)^2} E_i = E_{fl} \dots\dots\dots(3)
 \end{aligned}$$

here E_{R3} is the electric field of reflected beam from the film (side II). This electric field transmit through the film and exit the surface. Therefore, at the exit face, the electric field due to constructive interference (Boling et al. 1972) will be

$$\begin{aligned}
 E_{fl}^{exit} &= E_{R4} + E_{fl} \\
 &= \left(\frac{n_2 - 1}{n_2 + 1} \right) E_{fl} + E_{fl} = \left(\frac{2n_2}{1 + n_2} \right) E_{fl} \\
 &= \left(\frac{2n_2}{1 + n_2} \right) \left(\frac{8n_2n_3}{(1 + n_2)(n_2 + n_3)^2} \right) E_i \\
 &= \left(\frac{16n_2^2n_3}{(1 + n_2)^2(n_2 + n_3)^2} \right) E_i \dots\dots\dots(4)
 \end{aligned}$$

from the above analysis, it is clear that the ratio of electric field at entrance face to that of exit face $\left(\frac{E_{ent}^{fl}}{E_{fl}^{exit}} \right)$ depends upon the refractive index of both film (n_2) and substrate material (n_3). Using the value of film (n_2) as 1.59 glass (n_3) as 1.52, the ratio of electric field at entrance and exit face found to be 0.95. This difference in the electric field in the entrance and exit face is the reason for morphology asymmetry (Boling et al 1972). The sufficiently strong laser beam can create plasma in the surface of polymer film at the entrance face. As the plasma density increased, a standing wave can be formed through the film-glass interface. The electric field at the antinodes can become twice as large as the electric field in the incident beam. This strong electric field can create the pits in the film at side II. Therefore this pits formation in the exit face is due to internal damage rather than surface damage. In case of entrance surface there is no standing wave formation. The plasma at the entrance surface can be heated by the laser so that thermal shock can be created causing the complete surface removal at the exposed surface.

4. Conclusions:

Laser induced damage morphology study has been performed on dye doped polystyrene films that were deposited in both side of glass substrates. The morphological features has been studied in two different prf regime i.e. 1 pps and 20 pps. The study reveals distinct damage morphologies in different pulse regimes when interacting with transparent polymer films on

glass substrates. In the 20 pps regime, a complex interplay of surface removal, striations, and cracks results in a crater formation, influenced by the presence of absorbing dyes in the film. Conversely, the 1 pps regime shows complete film removal at the front end with minimal damage to the glass, indicating localized melting effects. Rear side damage morphology highlights the influence of beam profile modifications on damage patterns. The observed morphology asymmetry is attributed to differences in the electric field at the entrance and exit faces, leading to internal damage mechanisms such as plasma formation and standing wave effects. The presence of dendrimer-like microstructures in both front and rear side films suggests avenues for further research into their characteristics, potentially yielding insights applicable in biophysics. These findings underscore the importance of considering pulse frequency, energy levels, and internal dynamics in understanding laser-induced damage mechanisms and guiding the development of tailored mitigation strategies and the exploration of novel applications in diverse fields.

Acknowledgements

We are grateful to Dr. S. Pal, Laser Science and Technology Center (LASTEC), Metcalfe House, Delhi-110054, for allowing us to conduct experiments in his lab and for providing the necessary experimental facilities for the present research.

Conflict of Interest

Authors declare there is no conflict of interest.

References

- (1) Boling, N. L., Dube, G., Crisp, M. D., **1972**. Morphological asymmetry in laser damage of transparent dielectric surfaces. *Appl Phys Lett* 21 487.
- (2) Crisp, M. D., Boling, N. L., Dube, G., **1972**. Importance of fresnel reflections in laser surface damage of transparent dielectrics. *Appl Phys Lett* 21 364.
- (3) Folgado, Enrique, Guerre, Marc, Bijani, Christian, Ladmiral, Vincent, Caminade, Anne-Marie, Ameduri, Bruno, Ouali, Armelle, **2016**. *Polymer Chemistry* DOI: 10.1039/c6py01167e
- (4) Hsieh, Yi-Kong, Chen, Shiau-Chen, Huang, Wen-Ling, Hsu, Kai-Ping, Gorday, Kaiser Alejandro Villalobos, Wang, Tsinghai, Wang, Jane, **2017**. Direct Micromachining of Microfluidic Channels on Biodegradable Materials Using Laser Ablation. *Polymers* 9 242 1-16.
- (5) Jun, Indong, Lee, Jee-Wook, Ok, Myoung-Ryul, Kim, Yu-Chan, Jeon, Hojeong, **2016**. Femtosecond Laser Ablation of Polymer Thin Films for Nanometer Precision Surface Patterning. *J.Kor.Inst.Surf.Eng.* 49 1 20-25.
- (6) Kappes, R. S., Schonfeld, F., Chen, L., Golriz, A. A., Nagel, M., Lippert, T., Butt, H.J., Gutmann, J. S., **2014**. A study of photothermal laser ablation of various polymers on microsecond time scales. *Springer Plus* 3 489 1-15.
- (7) Kimmel, M., Do, B. T., Smith, A. V., **2011**. Deterministic single shot and multiple shot bulk laser damage thresholds of borosilicate glass at 1.064 micron. *Proc.SPIE* 8190 81900Z1.
- (8) Kumar, R., Singh, A. P., Kapoor, A., Tripathi, K. N., **2005**. Effect of dye doping in poly (vinyl alcohol) waveguides. *J Modern Optics* 52 1471-1483.
- (9) Rybaltovskii, A; Minaev, N; Tsyypina, S; Minaeva, S; and Yusupov, V, **2021**. "Laser-Induced Microstructuring of Polymers in Gaseous, Liquid and Supercritical Media" *Polymers* 2021, 13, 3525. <https://doi.org/10.3390/polym13203525>.
- (10) Tajdidzadeh, M, Zakaria, A.B., Talib, Z. Abidin, Gene, A.S. and Shirzadi, S. 2017. Optical Nonlinear Properties of Gold Nanoparticles Synthesized by Laser Ablation Polymer Solution. *Journal of Nanomaterials* **2017** Article Id 4803843, 1-9.
- (10) Vapaavuori, J., Priimagi, A., Soininen, A. J., Canilho, N., Kasemi, E., Ruokolainen, J., Kaivola, M., Ikkala, O., **2013**. Photoinduced surface patterning of azobenzene-containing supramolecular dendrones, dendrimers and dendronized polymers. *Optical Material Express* 3(6) 711-722.

Low-cost green Synthesis of Silica Engineering Nanomaterials from rice husk (Agriculture waste) and its physical and luminescent properties measurements

Akansha Kumari, Rakesh Kr Singh*, Abhay Kr Aman, Nishant Kr, Ajitendra Kr Singh

Aryabhata Center for Nanoscience and Technology, Aryabhata Knowledge University, Patna, India

Volume 1, Issue 2, March 2024

Received: 8 January, 2024; Accepted: 13 February, 2024

DOI: <https://doi.org/10.63015/5n-2406.1.2>

**Corresponding author email: rakeshsinghpu@gmail.com*

Abstract: The electrical, electronics, and drug industries are heavily reliant on the use of Silica materials for several applications. Green source of production of silica materials is very important to meet the growing demand for industrial purposes. The present work discusses the recent nanosilica production using low-cost methods, from rice husk-agricultural waste, and their structural, microstructural, and optical properties measurement for its applications. The crystallite size of silica particles was measured using XRD is 26 nm and 55 nm, which are prepared from rice husk synthesized by both coprecipitation and leaching processes, respectively.. The SEM images of both the samples showed structural order of the pores within the mesoporous structure. The leached sample showed a purity of around 80%. The infrared spectral data also supports the presence of hydrogen-bonded silanol groups and the siloxane groups in the silica. These nanosilica particles showed Photoluminescence in UV, Visible, and NIR regions. The nanoscale silica formation is also confirmed by TEM and DLS measurements. Zeta Potential studies found -22.12 mV reveals the stability of prepared nano silica for a longer duration.

Key words-Low cost, Rice husk, Crystalline structure, Functional Nano silica, Agriculture waste

1. Introduction: Nationwide concerns of energy-related climate change linked with the spiralling cost of fossil fuels have increased interest in renewable energy sources as an alternative source. During the last about 25 years, human activities such as the production and consumption of fossil fuels as well as agricultural and industrial activities have caused an increase in the atmospheric concentration of greenhouse gases [1]. The rice husk is not suitable for human consumption. The disposal of the ashes and partially bored husk creates environmental hazards. One interesting application of rice husk is the production of silica nanoparticles at low cost and high efficiency [2]. Silica has been used for gene delivery to obtain more efficient DNA delivery

vectors for both basic research and clinical trials in medical sciences [3]. It generally contains about 75% of the organic matter that evaporates while burning of husk and the rest obtained is rice husk ash and contains 85-90% amorphous silica, is highly porous and lightweight with very high external surface area. Its absorbent and insulating properties are useful for acting as a strengthening agent in building materials, Drug delivery, etc. [4-5]. Silica naturally exists in the form of nanoparticles in rice Husk. It accumulates around cellulose micro-compartments. When as a living thing (plant state) rice absorbs silica in the form of silicic acid from the soil and the silica accumulates around cellulose micro-compartments. When burnt rice husk (RH) gives rice husk ash (RHA)

which is a potential source of reactive amorphous silica. Silicon is the second most abundant element on the earth's crust. Moreover, it is considered an essential nutrient for plants and beneficial for crops like rice, wheat, etc. Rice plant absorbs silicon through the soil. That accumulates in the micro cellulose compartments of the grain cover. Silicon is not very reactive although more reactive than carbon. It readily reacts with oxygen. Materials with porous features on the nanoscale have important applications in optics, catalysis, drug delivery systems, hydroelectric cell, coatings, cosmetics, bio-separation, diagnostics, gas separation, and nanotechnology [6-10]. Nanoporous materials consist of an amorphous or crystalline framework with void spaces, which may be cylindrical or cage-like. Porous silica in nanophase possesses a high density of surface silanol (Si-OH) groups after calcination. The reactions of these silanols with various silanes produce different functional groups on the silica framework, which helps in the conjugation of molecules. The objective of the present research is to prepare a technological-grade nanomaterial from agricultural waste. Further, the material prepared should be porous which may be used in varied applications.

2. Materials and Methods:

Synthesis of nano silica from agriculture waste-rice husk: In the present work, the main objective was to obtain crystalline nanosilica of high purity as functional nanomaterial. Two different synthesis techniques were used to prepare two different samples and their properties were compared. The samples were prepared using Rice Husk Ash (RHA). In the first process, the Rice Husks were burnt in the open air and then the ash was further burnt in the high-temperature furnace at 800°C for 3 hours at a ramp rate of 6°C/min. Then the base treatment was done using 2.5 N NaOH. Then it was treated with conc. H₂SO₄ to maintain pH 2, adding liquid ammonia drop by drop to shift the solution to pH value 9. The produced Silica is then treated

with 6N HCl. The procedure was then followed by base treatment (2N NaOH). Then pH was adjusted to 8.5 by adding sulphuric acid. With the pH shift the solution starts to participate. This indicates the formation of nanosilica. In the second process, the Rice Husk was burnt in the high-temperature furnace at a temperature 800°C for 3 hours (6°C/min). The ash obtained was leached in HCl acid for 2 hours. The filtered and dried RHA was again heated in a high-temperature furnace at a temperature of 700°C for 3 hours (6°C/min). The flow chart for the preparation of Nano silica from rice husk as a schematic diagram is shown in figure-1. The RHA was then treated with base NaOH. The solution was kept in a hot air oven for an hour. The precipitate was obtained which was oven-dried for half an hour. Then it was treated with acid (HCl). The solution was kept in the ice bath for an hour. The filtered solution was oven-dried for 24 hours. The nano silica by both processes obtained was then characterized using characterization tools XRD, TGA & DTA, SEM, FTIR, Zeta potential, and PL.

3. Results and discussion

3.1. TGA-DTA measurement: Both Biological and inorganic components make up rice husk. At high temperatures, each of these chemicals exhibits a distinct behaviour. Thermogravimetric analysis (TGA), which is regarded as a crucial instrument for the identification and characterization of materials, can be used to observe this behaviour. The TGA curve in figure-2 demonstrated the weight changes that happened when the rice burned. The matching derivative profile of the DTA, which indicates the rate at which mass loss changes with temperature, is displayed in the insert of this figure-2. The TGA curve demonstrated the weight changes that happened when the rice burned. The matching derivative profile of the thermal analysis, which indicates the rate at which mass loss changes with temperature, is displayed. Based on the peaks related to the mass changes, the thermal analysis

was divided into three stages: stage 1, which was found to be between room temperature and 140°C; stage 2, which was found to be between 150 and 350°C; and stage 3, which was found to be between 350 and 500°C. The breakdown of

3.2. Structural analysis using XRD

Measurement: Two Nano silica samples as a SiO₂ from rice husk were prepared by two different methods, sample 1 (raw RHA) and

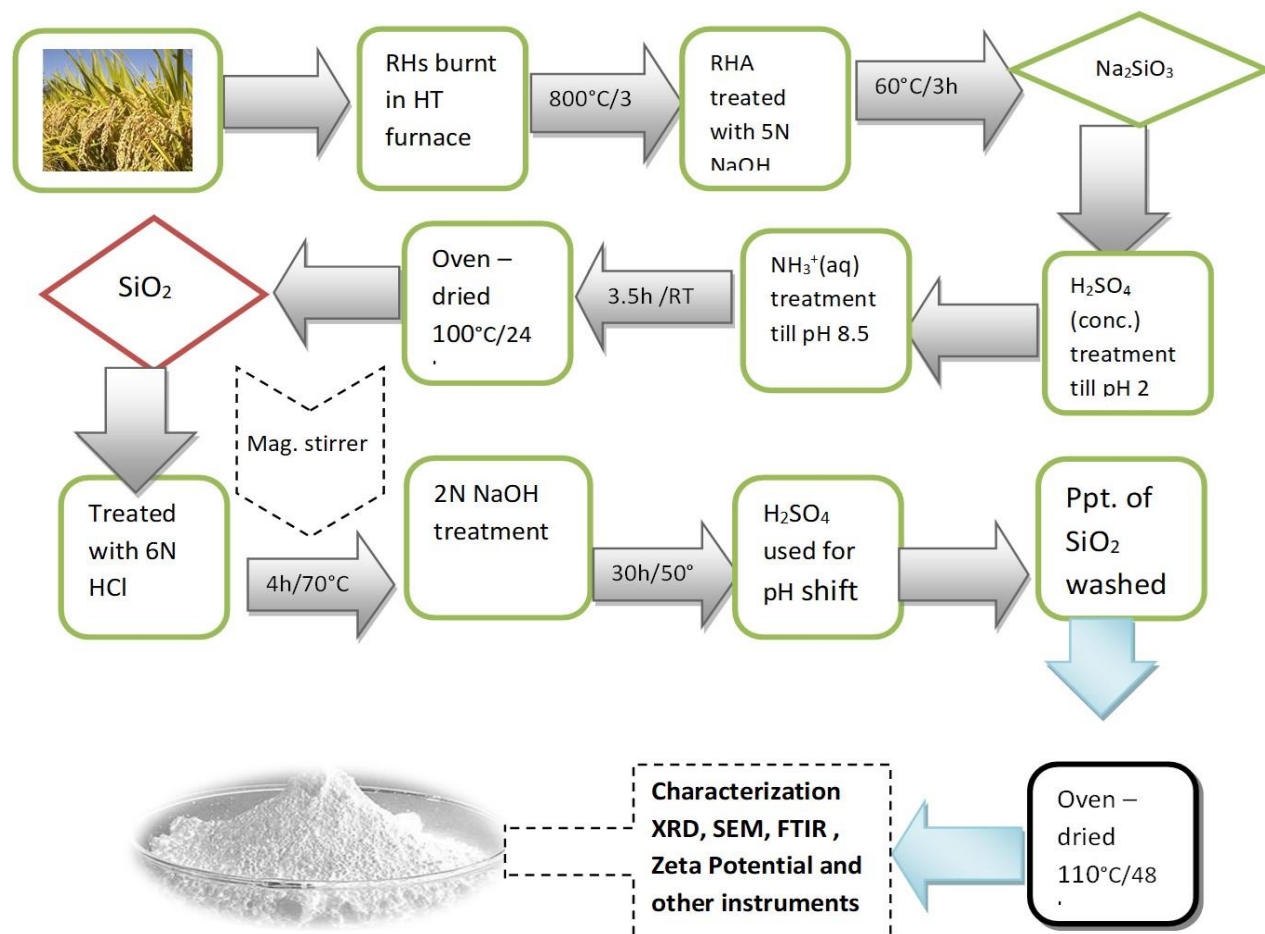


Figure 1. Flow chart for preparation of nanosilica from rice husk and agricultural waste

lignin and the removal of volatiles that were left over from the earlier stages (below 400°C) during stage 3 are responsible for the weight loss (20.14%); this process is analogous to passive pyrolysis [11, 12]. At last, the mass stabilized at a temperature of 550°C, and the remaining ash accounted for 25.57% of the measured total weight. This residue is primarily composed of silica SiO₂ and other metallic compounds, as confirmed also by a subsequent XRD measurement.

sample 2 (leached RHA) are shown in figure-3. The XRD pattern, shown in figure 3, shows the nanosilica, having an average particle size of 26 nm, using Scherrer's formula,

$$t = \frac{0.9\lambda}{\beta \cos \theta}$$

where symbol has usual meaning.

The sharp peaks show the nanomaterial prepared is in a pure very good crystalline phase and the crystal structure obtained was tetragonal [ICDD-98015-3886]. The combustion temperature of this sample was 800°C. This confirms that when

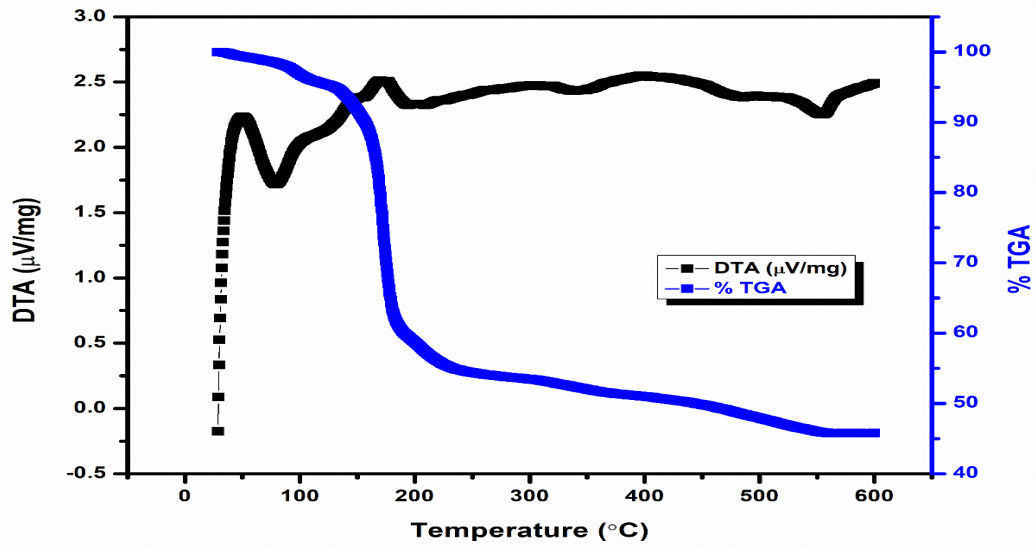


Figure 2. TGA and DTA curves for Nano-silica from rice husk

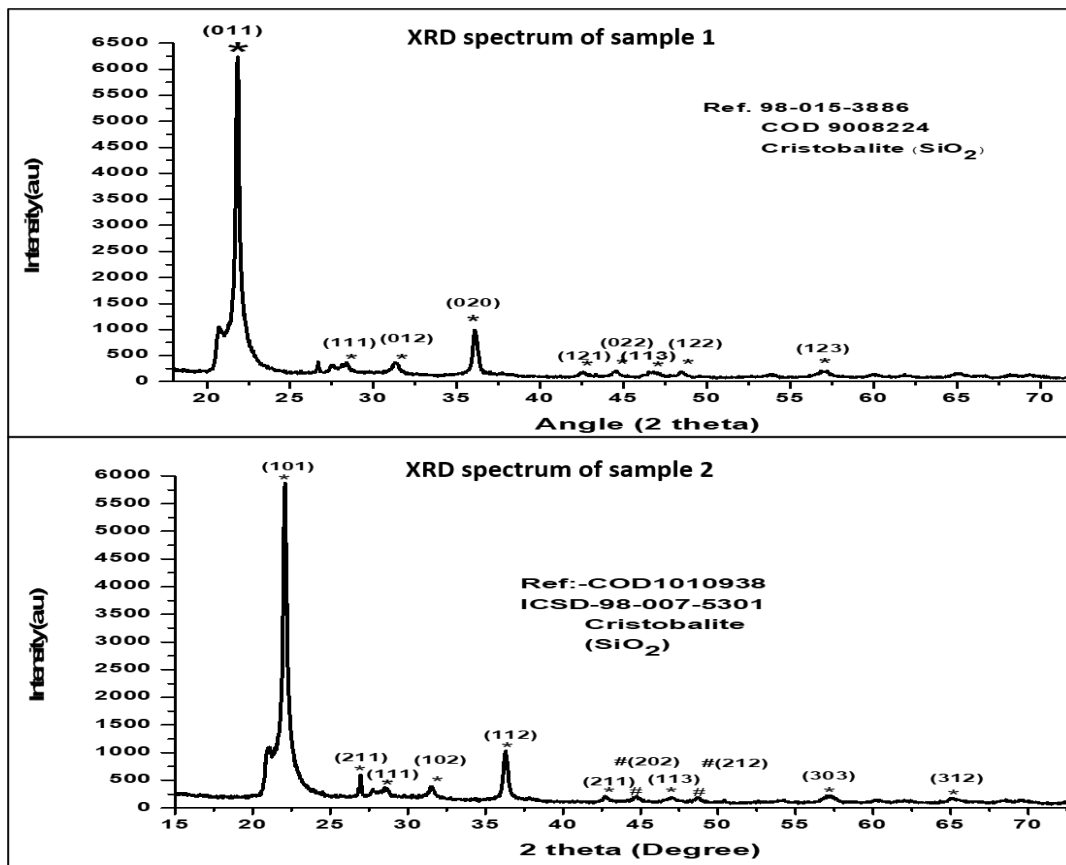


Figure 3. XRD spectra of sample 1 and sample 2

combustion temperature exceeds 700°C then the nano-silica obtained is in crystalline form. This

shows that the temperature range of 500-700°C should be strictly maintained for amorphous

phase nanosilica production which is concluded from our earlier reported work. Amorphous phase silica has several importance [13-14]. Generally higher temperature results in crystalline structure [14]. The purity of nanosilica obtained is 60% as confirmed by XRD peak intensity curves. The XRD pattern in Figure 3 shows the crystalline form of nanosilica, having a size of 55 nm, prepared by the coprecipitation method. Here the crystal structure of the nanosilica obtained is tetragonal [15]. The broadened bases are proof of nano-phase formed. The purity of nano silica obtained is 81% as confirmed by the XRD peak intensity curve.

This sample shows more purity than the first sample-1 (raw RHA), mentioned above. Moreover, the processes involved are less time-consuming. A comparison of both the XRD pattern of rice husk prepared by the coprecipitation method and the leached method is shown in Figure 3. Both nanosilica samples are crystalline in form but vary in crystalline size. The first sample is 26 nm while the second one is 55 nm. They have different purity percentages; the second sample yielded 81% pure silica while the first sample has 60% purity. According to this research, it can be considered that the second method of synthesis is more

suitable than the first where purity is concerned. While the crystalline size of the first sample is 26 nm in range, it will show enhanced properties of nano-phase and can be considered for mixing and binding substance where purity is the least consideration and the utmost concern is the nano-crystalline size and properties associated with it [16-17]. The peaks found in the XRD study demonstrate that the nanomaterials made by RHA are crystalline and that the crystals are tetragonal in form. The noticeable peak, which is seen at roughly 22 degrees, verifies the creation of nanosilica material and is precisely matched to the JCPDS file number [COD 98015-3866]. Figure 3 displays the XRD pattern, with the features hkl value also indicated in the figure, in agreement with previously published studies. This finding reveals that crystalline size and purity of percentage depend on methods of synthesis. Some research groups also reported similar results [18].

3.3. Surface morphology analysis using SEM

The SEM images of both the samples i.e., sample 1 (raw RHA) and sample 2 (leached

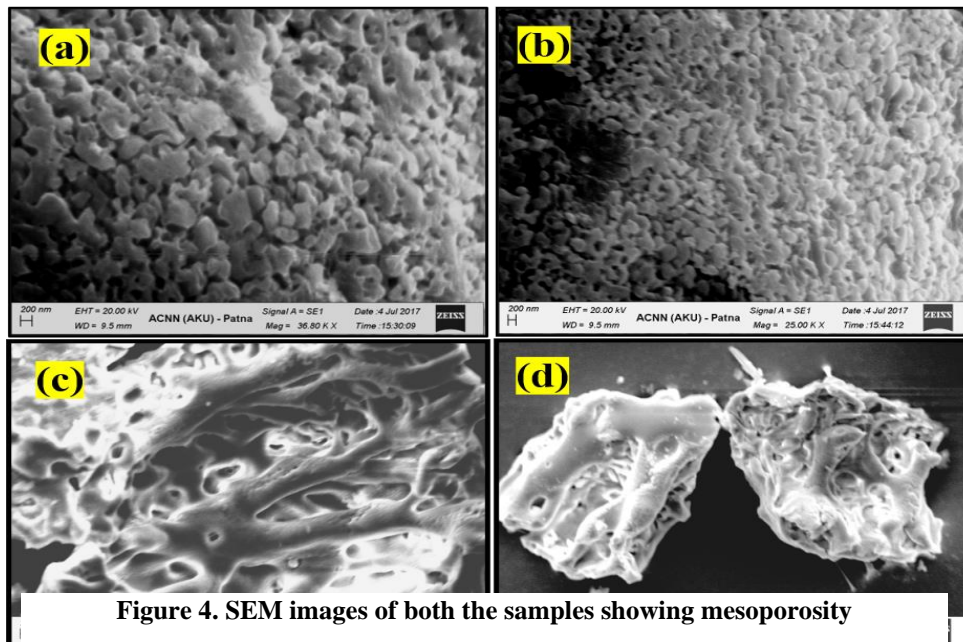


Figure 4. SEM images of both the samples showing mesoporosity

RHA) are shown in figure 4 (a,b) and (c,d) respectively and both the samples show coalescence and even distribution of the nanoparticles. The nanoparticles formed are agglomerated slightly distorted spherical and cylindrical. In addition, the SEM analyses of both samples showed porosity. The nanosilica obtained are mesoporous (2 nm - 50 nm). Nanosilica is one of the versatile classes of mesoporous materials. It has well-defined pore sizes that come with biocompatibility which can be used in a wide range of applications [19]. The surface morphology shown in the figure shows longitudinally aligned as a matrix consisting of lignin and hemicelluloses-like porous structure.

3.4. TEM Analysis: TEM have been used to further examine the silica NPs' size, shape, homogeneity, and uniformity. The nanoparticles that correspond to the sample are shown in Fig. 5 (a). The size distribution histogram was produced using the Image J program, as shown in Fig. 5 (b). In the histogram, an approximate Log-normal curve is combined. Silica nanoparticles (NPs) have a diameter of 40-50 nm and are roughly spherical. A size of 45 nm was measured for the predominant population. Agglomerates are also evident; this unavoidable phenomenon is linked to the interaction of tiny particles as a result of van der Waals forces or electrostatic attraction. The produced silica nanoparticles' modest size suggests that they can be effectively used in the right application.

3.5. FTIR measurements: The FTIR spectrum and data of the sample of both the samples, prepared by us are shown in Figure 6 and Table 1 and Table 2 respectively. FTIR results show that the peak numbers are almost at the same position, hence confirming that the same material (i.e. nanosilica) is synthesized by the two different methods. The peak numbers near $3400-3500\text{ cm}^{-1}$ show the presence of silanol-OH bond. The transmittance peak at 1097 cm^{-1} is due to the presence of siloxane bonds i.e. Si-O-Si bond is also present in both samples. The presence of Si-OH and other silane bond

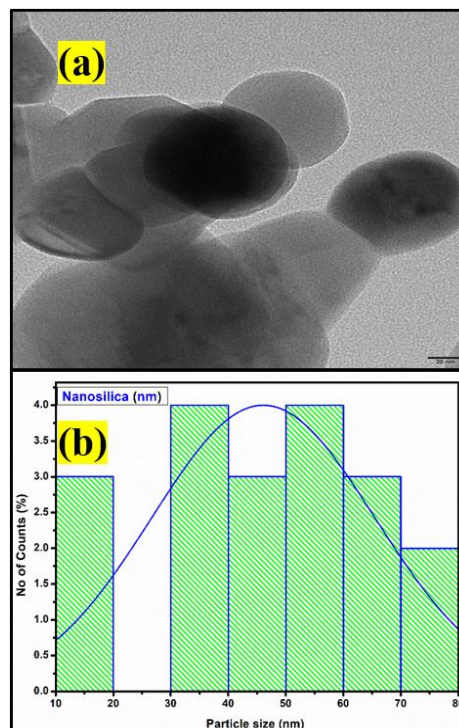


Figure 5 (a-b). TEM and histogram image of SiO_2 from rice husk ash

stretching vibrations are also present. The peaks between $600-800\text{ cm}^{-1}$ are attributed to the stretching vibrations of C-H and C-Cl bonds. The FTIR graph confirms the presence of silica and is like the FTIR of nanosilica obtained in different works [20-21]. Nanosilica has a very high surface/volume ratio and contains many surface hydroxyl groups, which provide electrostatic bond energy for dye molecules on its surface. Therefore, it may be used in several applications [22].

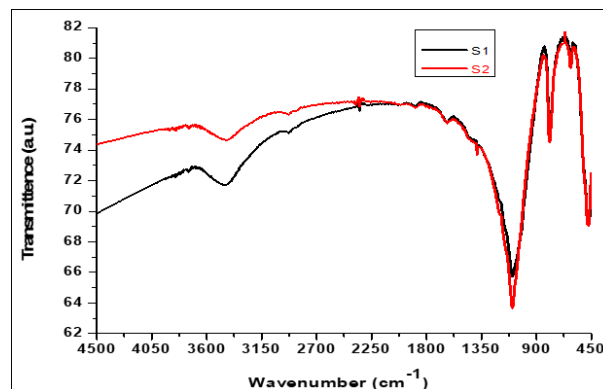


Figure 6. The FTIR graph of sample 1 and sample 2.

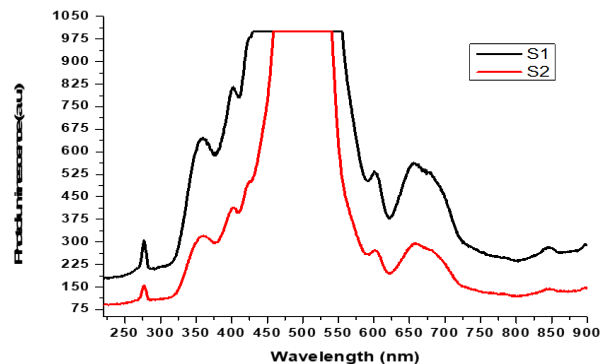
Table 1. For Sample 1 (raw RHA):

Peak Number	X (cm ⁻¹)-wave number	Y (%T)-transmittance
1	3436.26	74.65
2	1096.32	63.64
3	792.02	74.52
4	620.5	79.36
5	475.5	69.04

Table 2 For Sample 2 (leached RHA)

Peak Number	X (cm ⁻¹)-wave number	Y (%T)-transmittance
1	3460.27	71.71
2	1097.03	65.71
3	789.63	74.74
4	618.25	79.74
5	475.95	69.13

3.6. Photoluminescence Measurement: The Photo Luminescence (PL) measurements were carried out using a photoluminescence spectrometer, shown in figure 7. A 200 eV radiation source has been used as an excitation source in figure 7, the total number of peaks emitted in visible, NIR, and UV is almost the same for both Nano silica materials, synthesized by the leaching method and coprecipitate method. However, several peaks in the visible region for both samples are almost the same. This shows the PL intensity and emission were the same for samples synthesized using different methods and having different crystalline sizes. The cause of luminescence is generally due to energy band gap, defects in the crystal, types of elements present, the incident radiation wavelength used, and some other causes [23]. To the best of my knowledge to date, the PL in rice husks nanomaterial is not reported using a 200 eV excitation LASER source, but the PL of silicon (Si) based material was reported by some research groups [24]. The observed PL in this material can be compared with oxides of Silica. The bright luminescence may be due to the presence of silanone (Si=O) and the

**Figure 7. The Photo Luminescence Spectroscopy of sample 1 and sample 2.**

dioxasilirane, SiO₂ as the emitting defects are discussed in detail as prominent peaks lies in range of 455 nm and weak emissions are also seen 600 nm and 650 nm range also which is due to presence of silane bond also reported in other research group [25].

The luminescence behaviour of mesoporous silica nanoparticles shows possible applications in Bio Labelling due to luminescence behaviour. Luminescence and fluorescence imaging in Si nanoparticle imaging techniques are becoming essential in Biomedical applications and Bio nanotechnology fields. Such mesoporous structures may be potential candidates in dye removal and impurities removal from water. Zeolite and carbon nanotubes have mesoporous structures and are being used in water remediation.

3.7. Zeta Potential Measurement: Zeta potential readings were typically important for stability purposes. We discovered in this study that the silica particles have a negative charge in the pH range of 1–13. Zeta-potential measurements, which are needed to generate stable and dispersed suspensions of silica particles in water and validate the experimental conditions for the DLS measurement, are displayed in Fig-8, respectively, for various values. If the Zeta potential of every particle in suspension is high, either positive or negative, agglomeration of the particles will not occur. A common boundary between unstable and stable suspensions is +30 or -30 mV; particles with zeta

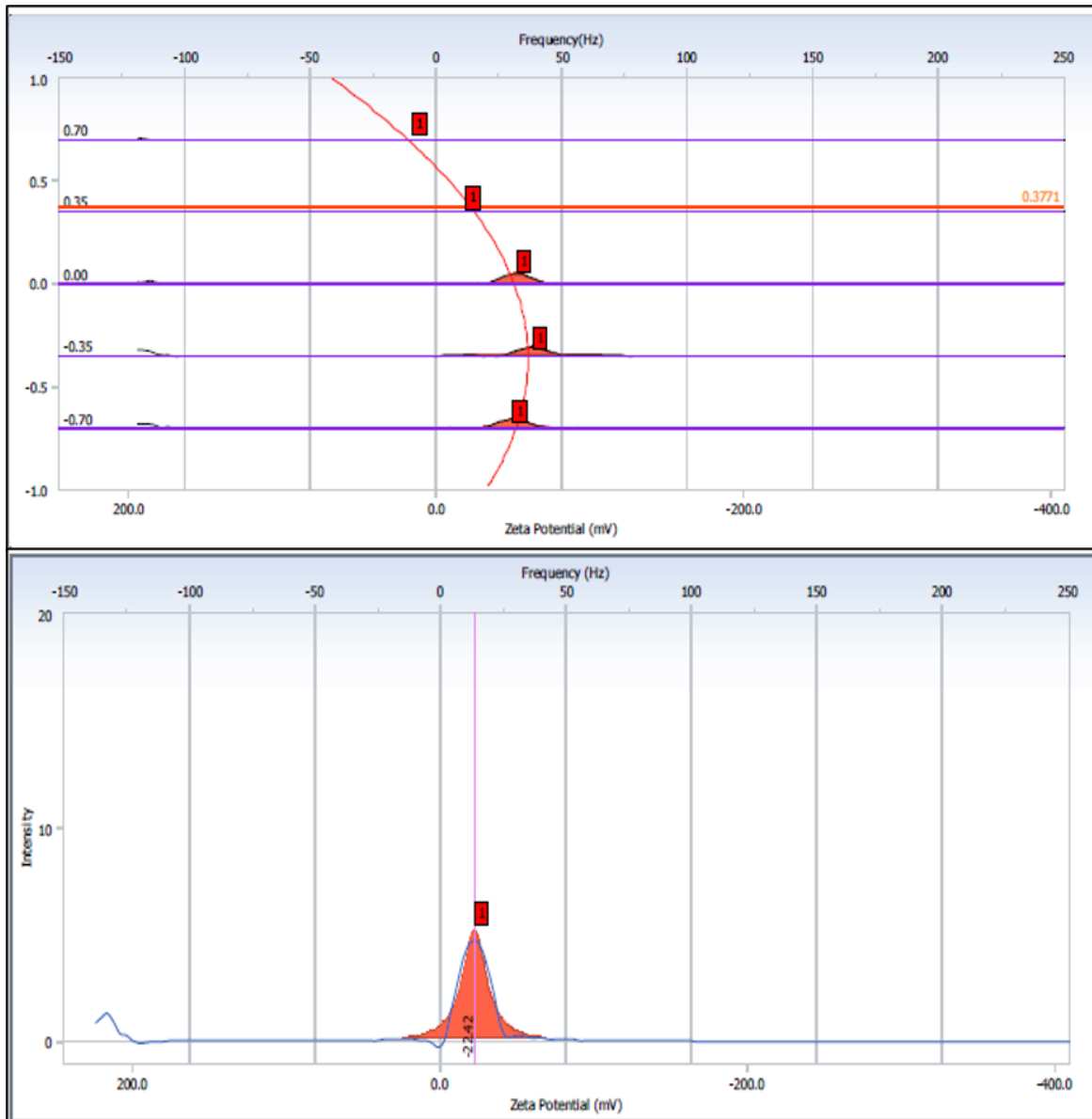


Figure 8: Zeta potential of crystalline Nano silica

potentials higher than this are frequently considered electrostatically stable. A greater zeta potential of around 25 mV is seen in all our samples, suggesting the stability of the post-synthesis suspensions. However, following the triplet experiment, the mean zeta potential displays a similar value of -22.12 mV, as indicated in Fig. 8. This Zeta potential (30.7 mV) is more than what previous writers have reported [25]. Other research groups have also reported on the use of this kind of feature for mesoporous silica drug delivery applications [26].

Conversely, the particles' durability and silica nature were shown by the negative Zeta potential, confirming their utility in drug administration.

3.8. Dynamic Light Scattering (DLS) and Particle size distributions: After the Zeta measurement, we also looked into DLS measurement to assess the particle size, which is typically more than the crystallite size as determined by XRD measurement and TEM analysis as the particle size when distributed in a liquid, as shown in figure-9.

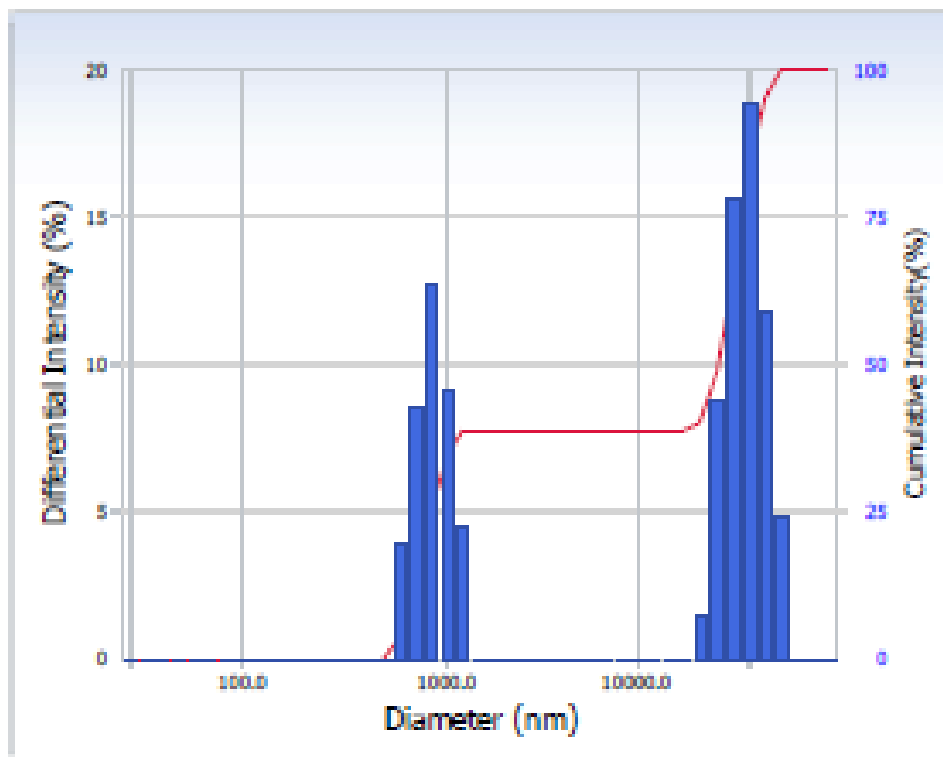


Figure 9. Hydrodynamic diameter and Concentration nanosilica

There is only one peak in width, centered at 1000 nm, and there is very little difference in the mean diameters of volume and number. Fine and coarse fractions in the dispersion are essentially non-existent, despite the size distribution in Figure 10 spanning to 1000 nm. The assertion that well dispersed somewhat spherical synthesizes silica nanoparticles is confirmed by the low value of the polydisperse index. Generally, the size measured by DLS is as hydrodynamic diameter.

4. Conclusions: The crystalline silica particles obtained from rice husk were found 26nm and 55nm, synthesized by both coprecipitation and leaching processes. The SEM images of both samples showed coalescence and even distribution of the nanoparticles with structural order of the pores within mesoporous, which support their use as Functional nanomaterials. The difference in purity was observed, the Leached sample showed a purity of around 80%. The infrared spectral data also supports the presence of hydrogen-bonded silanol group and the siloxane groups in the silica. Due to the

strong Si-O bond, silica-based mesoporous nanoparticles are more stable to external responses such as degradation, purification of water, and mechanical stress as compared to liposomes, liposomes, and dendrimers which inhibit the need for any external stabilization in the synthesis of mesoporous silica nanoparticles. These Nano silica particles showed Photoluminescence in UV, Visible, and NIR regions. The mesoporous nanosilica obtained can be further used in drug delivery as they have low toxicity as well as high drug loading capacity, so they are used in controlled and target drug delivery systems. The Nano scale silica formation is also confirmed by TEM and DLS measurement. Zeta Potential studies reveal the stability of prepared Nano silica for a longer period.

Acknowledgement: The authors would like to express their gratitude to the Department of Education, the Government of Bihar, and the Aryabhata Knowledge University, Patna for having such a facility for the synthesis and characterization of nanostructured materials.

Conflict of Interest: The authors affirm that they have no known financial or interpersonal conflicts that would have appeared to have an impact on the research presented in this study.

References:

- [1] Z.L. Wang, R.P. Gao, J.L. Gole, and J.D. Stout, Silica nanotubes and nanofiber arrays, *J. Adv. Mater.* 12, 2000, 1938–1940.
- [2] Z. Li, J. Zhang, J. Du, B. Han, and J. Wang, Preparation of silica microrods with nano-sized pores in ionic liquid microemulsions, *Colloids Surf. A: Physicochem. Eng. Aspects* 286, 2006, 117–120.
- [3] R. Manivannan and S. Ramanathan, The effect of hydrogen peroxide on polishing removal rate in CMP with various abrasives, *Appl. Surf. Sci.* 255, 2009, 3764–3768.
- [4] J. Zhang, L.-M. Postovit, and D. Wang, In situ loading of basic fibroblast growth factor within porous silica nanoparticles for a prolonged release, *Nanoscale Res. Lett.* 4, 2009, 1297–1302.
- [5] W. Zhang and M. Zhao, Fluidisation behaviour of silica nanoparticles under horizontal vibration, *J. Exp. Nanosci.* 5, 2010, 69–82.
- [6] F. Torney, B.G. Trewyn, V.S.Y. Lin, and K. Wang, Mesoporous silica nanoparticles deliver DNA and chemicals into plants, *Nat. Nanotechnol.* 2, 2007, 295–300.
- [7] M.L. Liu, D.A. Yang, and Y.F. Qu, Effect of different chemical additives and heat-treatment on ambient pressure dried silica aerogels, *J. Exp. Nanosci.* 5, 2010, 83–91.
- [8] M. Tomozawa, D.L. Kim, and V. Lou, Preparation of high purity, low water content fused silica glass, *J. Non-Cryst. Solids* 296, 2001, 102–106.
- [9] P.A. Tanner, B. Yan, and H. Zhang, Preparation and luminescence properties of sol-gel hybrid materials incorporated with europium complexes, *J. Mater. Sci.* 35, 2000, 4325–4328.
- [10] G. Wu, J. Wang, J. Shen, T. Yang, Q. Zhang, B. Zhou, Z. Deng, F. Bin, D. Zhou, and F. Zhang, Properties of sol-gel derived scratch-resistant nano-porous silica films by a mixed atmosphere treatment, *J. Non-Cryst. Solids* 275, 2000, 169–174.
- [11] Pijarn, N.; Jaroenworoluck, A.; Sunsaneeyametha, W.; Stevens, R., “Synthesis and characterization of nanosized-silica gels formed under controlled conditions,” *Powder Technol.*, 203, 2010, 462-467.
- [12] Liou, T. H., “Evolution of chemistry and morphology during the carbonization and combustion of rice husk,” *Carbon N. Y.*, 42, 2004, 78-83
- [13] P. Mishra, A. Chakraverty, and H.D. Banerjee, Production and purification of silicon by calcium reduction of ricehusk white ash, *J. Mater. Sci.* 20, 1985, 4387–4391.
- [14] A. Chakraverty, P. Mishra, and H.D. Banerjee, Investigation of combustion of raw and acid-leached rice husk for production of pure amorphous white silica, *J. Mater. Sci.* 23 1988, 21–24.
- [15] J. James and M. Subba Rao, Silica from rice husk through thermal decomposition, *Thermochim. Acta* 97, 1986, 329–336.
- [16] K. Kamiya, A. Oka, and H. Nasu, Comparative study of structure of silica gels from different sources, *J. Sol-Gel Sci. Technol.* 19, 2000, 495–499.
- [17] K.G. Mansaray and A.E. Ghaly, Determination of kinetic parameters of rice husks in oxygen using thermogravimetric analysis, *Biomass Bioenergy* 17, 1999, 19–31.
- [18] N. Yalcin and V. Sevinc, Studies on silica obtained from rice husk, *Ceram. Int.* 27 2001, 219–224.
- [19] T.H. Liou, Preparation and characterization of nano-structured silica from rice husk, *Mater. Sci. Eng.: A* 364, 2004, 313–323.
- [20] R.R. Zaky, M.M. Hessien, and A.A. El-Midany, Preparation of silica nanoparticles from semi-burned rice straw ash, *Powder Technol.* 185 2008, 31–35.
- [21] C. Real, M.D. Alcalá, and J.M. Criado, Preparation of silica from rice husks, *J. Am. Ceram. Soc.* 79, 1996, 2012–2016.

- [22] R. Conradt, P. Pimkhaokham, and U. Leela-Adison, Nano-structured silica from rice husk, *J. Non-Cryst. Solids* 145, 1992, 75–79
- [23] G.F. Luo, W.H. Chen, Y. Liu, Q. Lei, R.X. Zhuo, X.Z. Zhang, Multifunctional enveloped mesoporous silica nanoparticles for subcellular co-delivery of drug and therapeutic peptide, *Sci. Rep.* 4, 2014 6064-6049.
- [24] Naiara I. Vazquez, Zoilo Gonzalez, Begõna Ferrari, Yolanda Castro Synthesis of mesoporous silica nanoparticles by sol–gel as nanocontainer for future drug delivery applications, *Bol. Soc. Espanola Ceram. Vidr.* 5, 2017, 139–145
- [25] M.S. Dhlaminia, J.J. Terblansa, R.E. Kroona, O.M. Ntwaeaborwaa, J.M. Ngaruiyaa, J.R. Bothab and H.C. Swarta, Photoluminescence properties of SiO₂ surface-passivated PbS Nanoparticles, *South African Journal of Science* 104, 2008, 397-400.
- [25] Samira Jafari , Hossein Derakhshankhah , Loghman Alaei , Ali Fattahi , Behrang Shiri Varnamkhasti , Ali Akbar Saboury, Mesoporous silica nanoparticles for therapeutic/ diagnostic applications, *Biomedicine & Pharmacotherapy*, 109, 2019, 1100-1111
- [26] Naiara I. Vazquez, Zoilo Gonzalez, Begõna Ferrari, Yolanda Castro Synthesis of mesoporous silica nanoparticles by sol–gel as nanocontainer for future drug delivery applications, *Bol. Soc. Espanola Ceram. Vidr.* 5, (2017), 139–145.

CNS&E

Current Natural
Sciences &
Engineering

www.cnsejournals.org

Published by
**Vigyanvardhan
Blessed
Foundation
(VBF)**

**Globally
Visible**

**Peer
Reviewed**

**The
Most
Valuable
& Biggest
Journal on
New Science
from India**

**A Comprehensive
Interdisciplinary
Journal**

**Easy
Submission,
Quick
Publication**

**CNS&E Editorial Board Comprises of Globally
Renowned S & T Luminaries & Advisory Support from
World Top Institutes' Leaders**

Current Natural Sciences & Engineering (CNS&E) Journal publishes new, innovative and cutting-edge research in all areas of Natural sciences including physical, chemical, health, nuclear, agricultural, environmental sciences, energy, metrology, nanomaterials, Hydrogen Energy and Net Carbon Zero

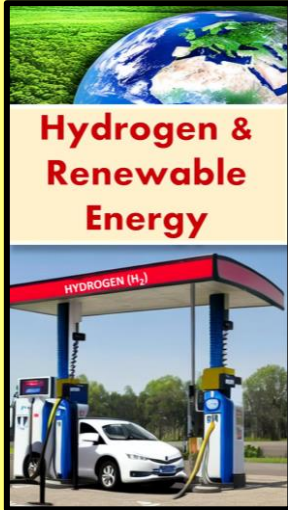
**Free from
Heavy
Publishing
Charges..**

**A Unique Platform to Boost your
Research Impact Globally !**

<https://cnsejournals.org/manuscript-submission/>

CNS&E

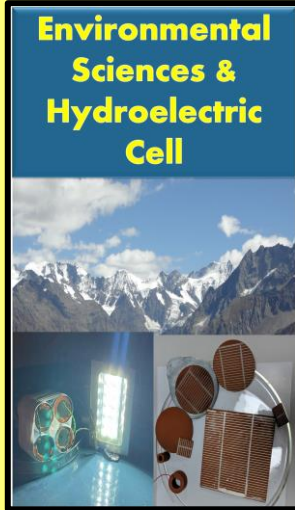
Current Natural
Sciences &
Engineering



Hydrogen & Renewable Energy

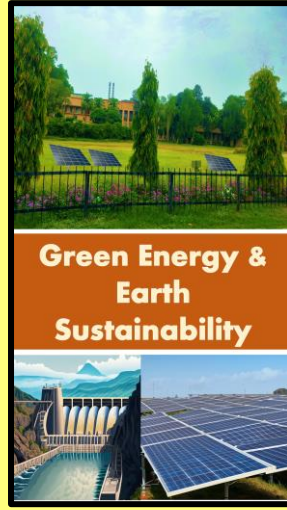
HYDROGEN (H₂)

This panel features a top image of the Earth from space, a middle image of a hydrogen refueling station with a car, and a bottom image of a hydrogen fuel cell.



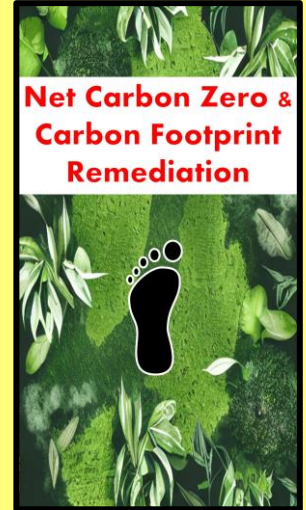
Environmental Sciences & Hydroelectric Cell

This panel shows a top image of a hydroelectric dam, a middle image of a hydroelectric power plant, and a bottom image of a hydroelectric cell.



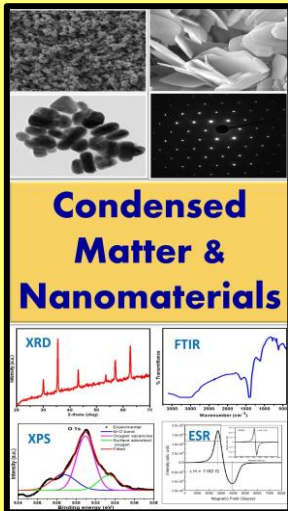
Green Energy & Earth Sustainability

This panel includes a top image of a green landscape with solar panels, a middle image of a hydroelectric dam, and a bottom image of solar panels.



Net Carbon Zero & Carbon Footprint Remediation

This panel shows a top image of green leaves, a middle image of a carbon footprint graphic, and a bottom image of green leaves.



Condensed Matter & Nanomaterials

XRD FTIR XPS ESR

This panel displays a top image of various materials, a middle image of a microscope, and a bottom image of scientific graphs including XRD, FTIR, XPS, and ESR.



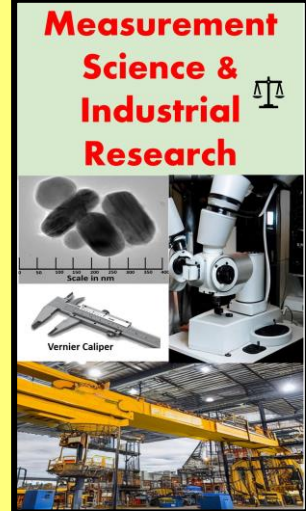
Health Science & Technology

This panel features a top image of a cell, a middle image of a medical device, and a bottom image of a cell.



Nuclear Science: Health & Society

This panel shows a top image of a nuclear atom, a middle image of a nuclear reactor, and a bottom image of a medical scanner.



Measurement Science & Industrial Research

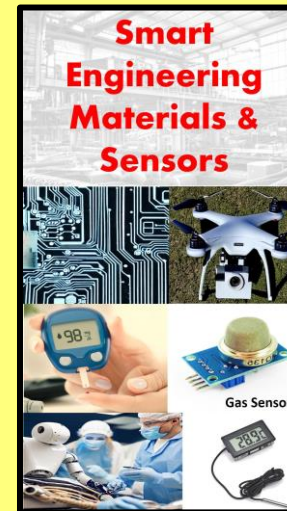
Scale in mm Vernier Caliper

This panel includes a top image of a scale, a middle image of a microscope, and a bottom image of an industrial factory.



Digital & Sustainable Agriculture

This panel shows a top image of a farm with digital icons, a middle image of a tractor, and a bottom image of a field.



Smart Engineering Materials & Sensors

Gas Sensor

This panel features a top image of a circuit board, a middle image of a drone, and a bottom image of a gas sensor.